

**EFFECT OF UNSTEADY WAKE, FREE STREAM
TURBULENCE, TIP GEOMETRY ON
BLADE TIP FLOW AND HEAT TRANSFER**

A Thesis

**Submitted to the Graduate Faculty of the
Louisiana State University and
Agricultural and Mechanical College
in partial fulfillment of the
requirements for the degree of
Master of Science in Mechanical Engineering**

in

The Department of Mechanical Engineering

**by
Vikrant Saxena
B.Tech., Indian Institute of Technology, 2001
May 2003**

Acknowledgements

I am extremely thankful to Dr. Srinath V. Ekkad for providing me with his profound knowledge of Gas turbines. I would also like to thank him for his guidance, advice and encouragement given to me. I will like to appreciate his good humor, patience and approach to any problem. I thank him for providing me financial support while at LSU.

I will also like to thank Dr. Michael Khonsari and Dr. Ramachandra Devireddy for being members of my MS committee. I also like to thank them for their valuable suggestions regarding my thesis.

I would like to thank my lab colleague Hasan Nasir for his valuable suggestions and contributions during experimental study. I would also like to thank Stacey Dupre for helping me during the experiments. Acknowledgements are due also to Mohammad Altorairi, Lujia Gao and Ryan Hebrer for their support and help. I would also like to thank Gautam Pamula for developing the macro and undergraduate students' team for building the experimental rig. I would also thank the sponsors of this project, NSF and NASA La-Space, for funding this project.

Finally, I thank my parents and my love Tej Kour, for their support and encouragement to me during my MS program.

Table of Contents

Acknowledgements.....	ii
List of Figures.....	v
Nomenclature.....	ix
Abstract.....	xi
Chapter 1. Introduction.....	1
1.1 The Description of Leakage Flow with Free Turbulence and Unsteady effects	1
1.2 Literature Survey.....	5
1.3 Objective of the Present Study.....	10
Chapter 2. Experimental Set-Up.....	11
2.1 Inlet Nozzle.....	12
2.2 Turbulence Grid.....	12
2.3 Wake Generator.....	13
2.4 Test Section.....	15
2.4.1 Test Blade.....	17
2.4.2 Guide Board.....	20
2.5 Description of Different Proposed Tip Geometries.....	20
2.5.1 Plane Tip.....	20
2.5.2 Ribs.....	20
2.5.3 Cylindrical Pin Fins.....	22
2.5.4 Squealers.....	22
Chapter 3. Data Acquisition Systems.....	26
3.1 Visual Image Processing System.....	26
3.2 Pressure Data Processing System.....	27
3.3 Hot Wire System.....	27
Chapter 4. Procedure and Data Reduction.....	30
4.1 Heat Transfer Experiments.....	30
4.2 Hot Wire Measurements.....	33
4.3 Pressure Measurements.....	33
4.4 Experimental Uncertainty.....	34
Chapter 5. Results: Flow and Pressure Measurements.....	37
5.1 Flow Measurements.....	37
5.2 Pressure Measurements.....	39

Chapter 6. Results: Heat Transfer Measurements.....	44
6.1 Effects of Flow Condition on the Tip Surface.....	44
6.2 Effects of Tip Geometry on Heat Transfer.....	66
6.3 Effects of Tip Geometry on Heat Transfer Compared to Baseline Case.....	69
Chapter 7. Conclusions.....	77
References.....	79
Vita.....	82

List of Figures

Figure 1.1 Tip Leakage Flow seen from the pressure side.....	1
Figure 1.2 Conceptual view of the Leakage Flow through the Clearance Gap Leakage Flow.....	2
Figure 1.3 Oxidation Heat Damages on the Blade Tip.....	3
Figure 1.4 Conceptual view of the unsteady wake propagation through a rotor blade row	4
Figure 1.5 Suggested history and effects of clearance gap separation bubble.....	6
Figure 1.6 Schematic layout of the full squealer on the blade tip.....	7
Figure 2.1 The overall layout of the facility and cascade test section.....	11
Figure 2.2 The schematic layout of the experimental setup.....	12
Figure 2.3 Turbulence Grid and Wake Generator as assembled in test cabinet.....	13
Figure 2.4 Wake generator drive components.....	14
Figure 2.5 Wake generator hub and rod assembly.....	14
Figure 2.6(a) Schematic layout of the back view of test section.....	16
Figure 2.6(b) Overhead view of test section.....	16
Figure 2.7 The complete description of the heat transfer Test Blade.....	18
Figure 2.8 The location of the pressure taps on the blade surface at different span locations.....	19
Figure 2.9 The location of the pressure taps on the shroud surface above the blade.....	19
Figure 2.10 Plane Blade tip configurations.....	20
Figure 2.11 Blade tip with ribs in different orientations.....	21
Figure 2.12 Blade tip with cylindrical pin fins.....	22
Figure 2.13 Blade tip with different kinds of squealers.....	23

Figure 2.14 Top view of the Blade tip for all the different configurations tested.....	24
Figure 3.1 A schematic layout of the image processing system.....	26
Figure 3.2 A Plunix RGB camera.....	27
Figure 3.3 A schematic layout of the pressure measurement system.....	28
Figure 3.4(a) A single calibrated hot wire probe.....	28
Figure 3.4(b) Hot Wire system.....	29
Figure 4.1 Hue-Temperature calibration curve.....	31
Figure 5.1 Velocity signature for the four flow conditions.....	38
Figure 5.2 Surface pressure distributions on the test blade at different span Locations.....	40
Figure 5.3 Comparison of surface pressure distributions for two different span Locations	41
Figure 5.4 Static pressure distributions $\{(P_t-P_s)/P_t\}$ on the shroud for the plain tip under different flow conditions.....	42
Figure 5.5 Static pressure distributions $\{(P_t-P_s)/P_t\}$ on the shroud for all the ten different tip configurations.....	43
Figure 6.1(a) Detailed heat transfer coefficient distributions on plain tips (Case 1).....	46
Figure 6.1(b) Effect of upstream flow condition on tip camberline heat transfer coefficient for baseline case.....	47
Figure 6.2(a) Detailed heat transfer coefficient distributions on tip with ribs against the flow 3-quarters inch away (Case 2)	48
Figure 6.2(b) Effect of upstream flow condition on tip camberline heat transfer coefficient for case 2.....	49
Figure 6.3(a) Detailed heat transfer coefficient distributions on tip with ribs against the flow one inch away (Case 3)	50
Figure 6.3(b) Effect of upstream flow condition on tip camberline heat transfer coefficient for case 3	51

Figure 6.4(a) Detailed heat transfer coefficient distributions on tip with ribs along the flow one inch away (Case 4).....	52
Figure 6.4(b) Effect of upstream flow condition on tip camberline heat transfer coefficient for case 4.....	53
Figure 6.5(a) Detailed heat transfer coefficient distributions on tip with parallel ribs one inch away (Case 5).....	54
Figure 6.5(b) Effect of upstream flow condition on tip camberline heat transfer coefficient for case 5.....	55
Figure 6.6(a) Detailed heat transfer coefficient distributions on tip with pins one inch away (Case 6).....	56
Figure 6.6(b) Effect of upstream flow condition on tip camberline heat transfer coefficient for case 6.....	57
Figure 6.7(a) Detailed heat transfer coefficient distributions on tip with Suction Side Squealer (Case 7).....	58
Figure 6.7(b) Effect of upstream flow condition on tip heat transfer coefficient towards pressure side for case 7.....	58
Figure 6.7(c) Effect of upstream flow condition on tip heat transfer coefficient towards suction side for case 7.....	59
Figure 6.8(a) Detailed heat transfer coefficient distributions on tip with Pressure side Squealer (Case 8).....	60
Figure 6.8(b) Effect of upstream flow condition on tip heat transfer coefficient towards pressure side for case 8.....	60
Figure 6.8(c) Effect of upstream flow condition on tip heat transfer coefficient towards suction side for case 8.....	61
Figure 6.9(a) Detailed heat transfer coefficient distributions on tip with camberline Squealer (Case 9)	62
Figure 6.9(b) Effect of upstream flow condition on tip heat transfer coefficient towards pressure side for case 9.....	62
Figure 6.9(c) Effect of upstream flow condition on tip heat transfer coefficient towards suction side for case 9.....	63

Figure 6.10(a) Detailed heat transfer coefficient distributions on tip with Full Squealer (Case 7).....	64
Figure 6.10(b) Effect of upstream flow condition on tip heat transfer coefficient towards pressure side for case 10.....	65
Figure 6.10(c) Effect of upstream flow condition on tip heat transfer coefficient towards suction side for case 10.....	65
Figure 6.11 Detailed heat transfer coefficient distributions on tip for all the different tip geometries.....	68
Figure 6.12 Comparison of camberline heat transfer coefficient distributions of Case 1 and Case 2.....	69
Figure 6.13 Comparison of camberline heat transfer coefficient distributions of Case 1 and Case 3.....	70
Figure 6.14 Comparison of camberline heat transfer coefficient distributions of Case 1 and Case 4.....	71
Figure 6.15 Comparison of camberline heat transfer coefficient distributions of Case 1 and Case 5.....	72
Figure 6.16 Comparison of camberline heat transfer coefficient distributions of Case 1 and Case 6.....	73
Figure 6.17 Comparison of camberline heat transfer coefficient distributions of Case 1 and Case 7.....	74
Figure 6.18 Comparison of camberline heat transfer coefficient distributions of Case 1 and Case 8.....	75
Figure 6.19 Comparison of camberline heat transfer coefficient distributions of Case 1 and Case 9.....	76
Figure 6.20 Comparison of camberline heat transfer coefficient distributions of Case 1 and Case 10.....	76

Nomenclature

C	blade axial chord length (12 cm)
d	wake rod diameter (cm)
h	local heat transfer coefficient ($\text{W}/\text{m}^2\text{-K}$)
n	number of rods on wake generator
N	speed of rotating rods (rpm)
P_s	local static pressure
P_t	total pressure at inlet (atmospheric pressure)
S	wake Strouhal number, $2\pi Ndn/(60V_1)$
T_m	mainstream temperature
T_w	local wall temperature
T_u	free-stream mean turbulence intensity at cascade inlet
V_1	cascade inlet velocity (m/s)
V_2	cascade exit velocity (m/s)
X	streamwise distance from leading edge to trailing edge along the midchord.
ν	kinematic viscosity of inlet air
Hue	Hue of the color
Q''	Heat flux on the blade tip
Q''_{loss}	Heat flux loss from the blade tip due to conduction and radiation effects
H	height of test blade
A	Surface area of the blade tip surface
M	Mach number

Re free stream Reynolds number, $\rho VC/\mu$

S blade spacing

T_w Wall temperature

V Voltage Input

I Current Input

Subscripts

∞ mainstream flow

t total

s static

Abstract

A comprehensive investigation of the effect of various tip sealing geometries is presented on the blade tip leakage flow and associated heat transfer. The linear cascade is made of four blades scaled up HPT turbine in a low speed wind tunnel facility with the two corner blades acting as guides. The tip section of a HPT first stage rotor blade is used to fabricate the 2-D blade. The wind tunnel accommodates an 116° turn in the flow through the blade cascade. The mainstream Reynolds number based on the axial chord length at cascade exit is 4.83×10^5 . The center blade has a tip clearance gap of 1.5625% with respect to the blade span. Static pressure measurements are obtained on the blade surface, the tip surface, and the shroud. Several tip sealing techniques are investigated in this study. Crosswise trip strips are used to reduce leakage flow and associated heat transfer by placing the trip strips in different orientation. Cylindrical pin fins are investigated and compared to the trip strip geometries. A full and three partial squealers are investigated. The partial squealers are placed on the suction side, pressure side and midchord of the blade tip. Detailed heat transfer measurements are obtained using a steady state HSI-based liquid crystal technique. The upstream wake effect is simulated with a spoked wheel wake generator placed upstream of the cascade. A turbulence grid placed even farther upstream generates the required free-stream turbulence of 4.8%. The effect of periodic unsteady wake effect is investigated by varying the wake Strouhal number from 0.0 to 0.2, and to 0.4. Results show that the squealers and the trip strips placed against the leakage flow direction produce the lowest heat transfer on the tips compared to all the other cases. Results also show that the full squealer has a strongest effect on the overall reduction of tip heat transfer.

Chapter 1

Introduction

1.1 The Description of Leakage Flow with Free Turbulence and Unsteady Effects

In the axial flow turbines, the blades are fixed on the moving rotor under a stationary casing (i.e. shroud) as shown in Figure 1.1. As the combustor exhaust gas flows through the turbine, these turbine blades help in converting the energy of the hot pressurized gases to mechanical energy. In an aircraft engine the major part of this energy is utilized by the compressor and produce thrust. In case of power turbines, the goal is also to produce additional power to generate electricity.

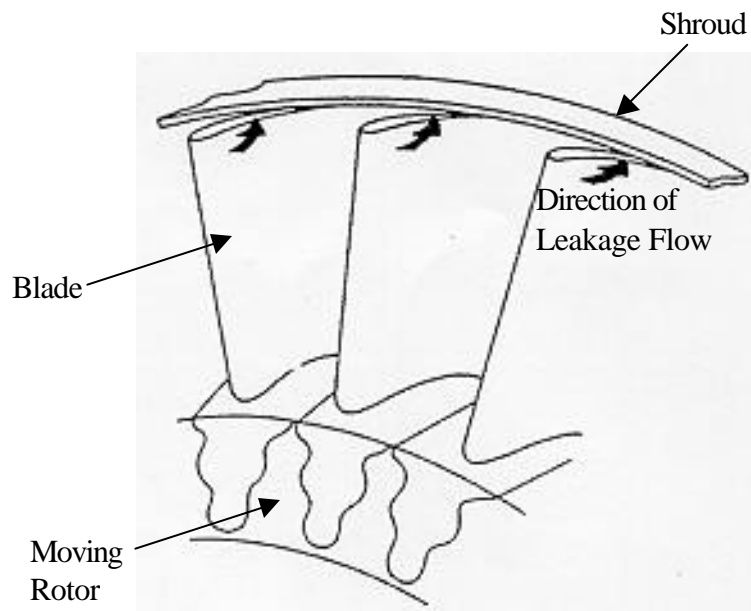


Figure 1.1 Tip Leakage Flow seen from the pressure side (Metzger et.al 1989)

The gap between this stationary casing and the blade tip is called clearance gap. The clearance gap is the region of the lower area of cross-section. The concave side of the blade is called the pressure side and the convex side is called suction side. These leads to high pressure difference across the pressure and suction sides of the blade tip that causes the flow to accelerate in this gap region as shown in Figure 1.1 and Figure 1.2. This flow is accompanied by secondary flows, which have the effect of bringing very hot portion of the mainstream to the vicinity of the clearance gap, especially at the downstream portion of the blade. The portion of the blade tip in contact with this hot air is exposed to high convection heat transfer.

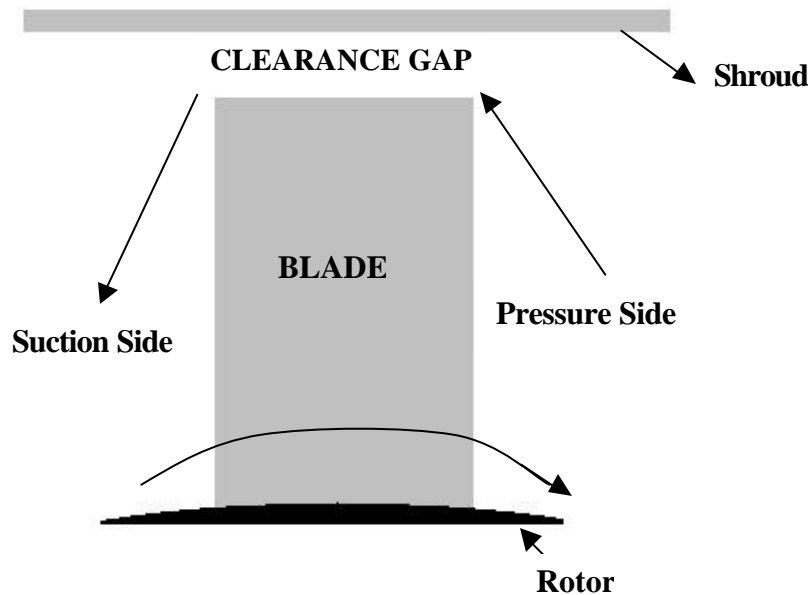


Figure. 1.2 Conceptual view of the Leakage Flow through the Clearance Gap Leakage Flow

The rotor tip leakage flow, although undesirable, cannot be eliminated. The leakage flow causes high heat load to the tip region and leads to oxidation and cracking resulting in blade tip as discussed by Yang and Diller (1995) as shown in Figure 1.3.

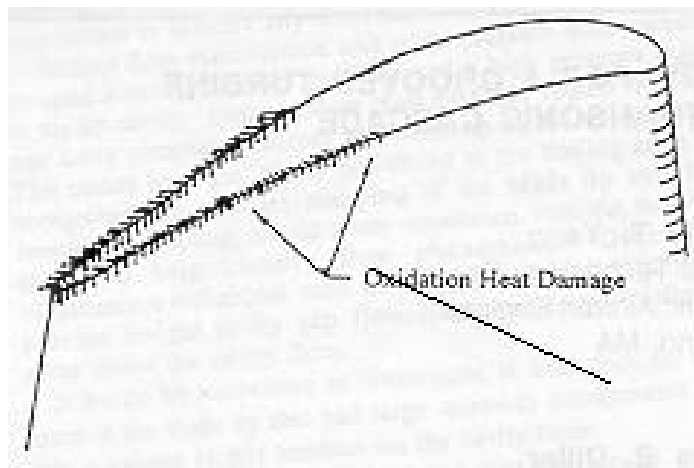


Figure 1.3 Oxidation Heat Damages on the Blade Tip (Yang and Diller, 1995)

This affects both the structural durability and the stage aerodynamic performance of the blade. Since it is impossible to eliminate the tip leakage flow between the blade and the stationary shroud, effort is focused on designing the blade tip region to reduce leakage flow and thus reduce overall heat load and delay failure initiation processes. Most of the research is now focused on designing tip geometries that will reduce the leakage flow and the associated heat transfer of the tip.

The leakage flow is associated with many unsteady effects. Typically unsteady flows that occur naturally in the flow are for one body in the wake of another. Another type are those in which the entire flow field oscillates are for downstream of a pump. The third type of unsteadiness in which we are interested is a forced, periodic, and localized, disturbance of the flow. This occurs when a moving object cuts across the flow path, as in turbine stages. The relative motion of the alternate stationary and rotating annular blade rows, which comprise each stage, causes the unsteadiness in the flow as shown in Figure

1.4. The unsteady flow that occurs in the passage of an axial flow turbomachines strongly affects the blade's fluid dynamic performance, flow loss and heat transfer.

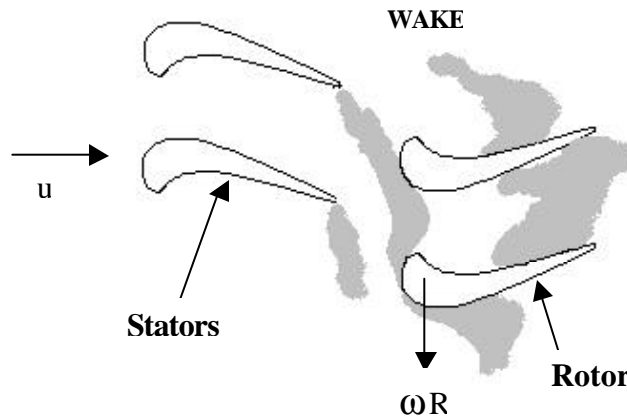


Figure. 1.4 Conceptual view of the unsteady wake propagation through a rotor blade row (Mayle et.al., 1991)

Doorly et al. (1985) describes the principal components of unsteadiness as:

1. **Wake Passing:** At the exit of a given blade row the flow is non-uniform in the circumferential direction. This is due to the presence of wakes that are shed at the trailing edge of each blade. The blades of the downstream row are subjected to a periodically varying inlet velocity and turbulence flow field, since the relative rotation of the rows causes the downstream blades to chop through the wakes.
2. **Shock Wave Passing:** For transonic stages only, shock waves generated by a transonic blade impinge on the blades of downstream row. The blade of the downstream row consequently chops periodically through shock waves, in addition to wakes.
3. **Potential Flow Interaction:** The relative motion between a blade and the blades of the rows immediately upstream and downstream causes the periodic

variations in the potential flow field. If the row spacing is increased, this form of unsteadiness decays rapidly.

4. **Additional High Energy Turbulence:** The flame unsteadiness in the combustion chamber of high –pressure turbine stage may generate high levels of turbulence. This effect persists through the first and second turbine blade rows.

The turbulence generated at the exit of the combustor contributes to significant heat transfer enhancement. The effect of turbulence is not very well understood as yet. The randomly distributed turbulent spots are formed due to the breakdown of the laminar boundary layer by the free stream turbulence disturbances. These spots move further downstream along with the flow and form new spots, eventually forming a fully turbulent boundary layer. This leads to enhancement in the heat transfer.

1.2 Literature Survey

Bindon (1989) and Morphis and Bindon (1988) studied tip clearance loss, using a linear cascade under low-speed conditions, and concluded that the losses varied linearly with gap size. Using static pressure measurements and flow visualization, Bindon observed a separation bubble on the blade pressure edge that mixes with a high-speed leakage jet induced at the midchord as shown in Figure 1.5. The leakage flow was defined as sink-like on the pressure side and source-link on the suction side of the blade. Yaras et al. (1989) also observed the presence of a separation bubble away from the leading edge and concluded that flow towards the leading edge had little effect on overall losses. In Yaras' study, a high-speed test rig was used.

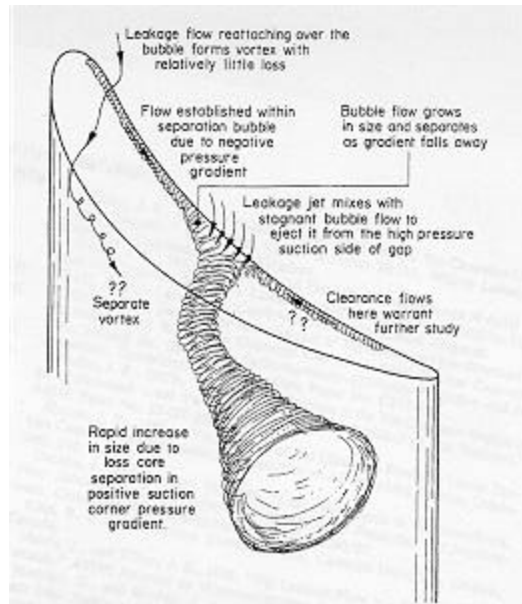


Figure 1.5. Suggested history and effects of clearance gap separation bubble (Bindon).

Yamamoto (1989) also found that leakage vortices were sensitive to incident angle and the blade tip gap height. Mayle and Metzger (1982) investigated heat transfer on a 2-D rectangular tip with rotating and stationary shroud. They established that the effects of relative motion between a blade model and the shroud have negligible effects on heat transfer data. Dring et. al (1982) and Hodson (1984) used low speed rotating turbine to show that the wakes shed by the blades of one row induce an unsteady transition of the boundary layer on the blades comprising the downstream blade row. Doorly (1988) concluded that the effect of wake passing an already turbulent boundary layer is fairly small. Han and Zhang (1993) concluded that unsteady wake causes an increase of turbine blade heat transfer for a given low or medium incoming free-stream turbulence. Funazaki (1994) investigated that the blade tip heat transfers enhanced by the periodic passing wakes from the moving bars and this effect increases as the Strouhal number of moving bars is increased. Steinthorsson (1996) concluded that the tip heat

transfer near the leading edge slightly increases when the rotational speed is varied. The variation in rotational speed causes the change in the incidence angle, which enhances the blade tip transfer.

Metzger et al. (1989) and Chyu et al. (1989) investigated the effects of varying the recess depth on the tip heat transfer of a blade tip model. It was determined that tip heat transfer was reduced under the presence of a cavity. The cavity simulated the squealer tip geometry. Leakage flow was reduced until the depth reached $D/W = 0.2$. Here, D is the depth and W is the width of the squealer on the blade tip as shown below.

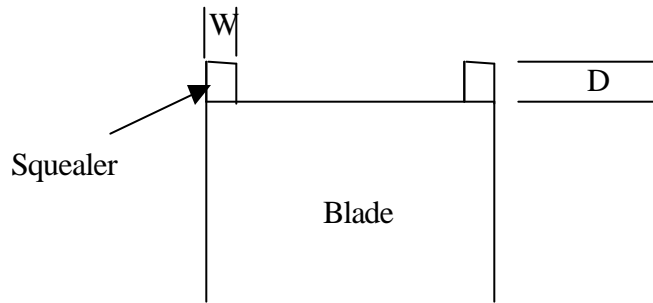


Figure 1.6 The schematic layout of the full squealer on the blade tip.

Martin and Nicolas (2000) investigated the influence of the tip's geometry, the gap size, the main flow Mach and Reynolds number and the coolant infection into the grooved tip section. Kaiser and Bindon (1997) analyzed the effects of tip clearance; tip geometry and multiple stages on turbine stage efficiency in a rotating turbine rig. They investigated the pressure and heat transfer distributions on a stationary flat blade cascade model and compared these experimental results with CFD predictions.

Metzger et al. (1990) performed the numerical simulation of leakage flow and compared the results to the actual turbine and its operating conditions measurements available. The comparison between the model and the measured heat transfer showed

good agreement. Thus, they proved that the model would be helpful for the early design estimates. Yang and Diller (1995) used the Heat Flux Microsensor (HFM) to measure the heat flux in the tip cavity of a blade. These HFM measurements showed that the heat transfer coefficients in the tip gap are both insensitive of tip gap height and mainstream flow velocity. Bunker et al. (1999) published the first study with detailed blade tip heat transfer measurements on actual blade tips. Their measurements were made for a first-stage power generation blade using steady state liquid crystal technique. They varied the curvature of the blade tip edges (rounded and sharp) and demonstrated that the blade with a tip edge radius had a greater leakage flow and a higher heat transfer coefficient. Bunker et al. (1999) also reported that an increase in free stream turbulence intensity increased the heat transfer coefficient. These authors observed that there exists an area of low heat transfer located toward the blade leading edge. This is referred to as the sweet spot. Ameri and Bunker (1999) used CFD simulations to reproduce the results for the same blade geometry shown by Bunker et al. (1999). They concluded that the assumption of periodic flow was invalid for tip heat transfer calculations because the entire passage had to be modeled. Their numerical results for the radius edge showed better agreement with the experimental data than that of the sharp edge.

Azad et al. (2000) performed heat transfer investigations on blade tip in which three different tip clearance gaps ($C/H=1, 1.5, 2.5\%$) were used. They used a GE-E³ engine blade and a pressure ratio of 1.2 in a five-blade cascade. They measured heat transfer coefficients using the transient liquid crystal technique. The results of this experiment showed that a larger gap causes higher heat transfer coefficient on the tip. A second study by Azad et al. (2000) investigated the effects of a recessed tip ($D/H=3.77\%$)

on the heat transfer coefficient. It was determined that the squealer tip produced a lower overall heat transfer coefficient compared to the plain tip. The squealer redirected the airflow over the tip forcing the flow to move from the leading edge pressure side to the trailing edge suction side.

Bunker and Bailey (2000a) investigated the effectiveness of chordwise sealing strips to reduce leakage flow and heat transfer. Sealing strips increased resistance to leakage flow. Sealing strips also reduced flow when the gap between the strip and shroud was the same as that between the plain tip and shroud. The strip location affected the tip heat load distribution. The present study is based on this study by Bunker and Bailey (2000a). Bunker and Bailey (2000b) continued the study with more complicated strip geometries such as the circumferential rub strips and 45° angled rub strips. Their experiments showed that circumferential and angled strips increase heat loads by 20 – 25% and 10 – 15% respectively. Bunker and Bailey (2001) and Azad et al. (2001) examined the different squealer geometries for reducing tip leakage flow and associated heat transfer, including single and double squealers. They found that several squealer geometries reduce the overall heat transfer to the tip compared to the plain tip. The midchord squealer produced the best leakage reduction.

There have been several studies that have focused on the effect of periodic unsteady wakes on blade heat transfer in linear cascades. Wittig et al. (1988) and Han et al. (1993) focused on the blade surface heat transfer (not on the blade tip) under the effect of periodic unsteady wakes. Teng et al. (2001) presented detailed heat transfer coefficient distributions on a large-scale blade tip with different tip gaps. The effect of unsteady wake on tip heat transfer was investigated. They concluded that a reduced tip clearance

gap produces lesser effect of the upstream unsteady wake thereby producing lower heat transfer coefficients. However, they did not investigate the effects of various tip geometries under unsteady wake effects. Also, they used the mid-span section of the blade to simulate the leakage flow and not the tip section. This can produce non-typical leakage flow over the tip compared to the tip section.

1.3 Objective of the Present Study

The objectives of the present study are:

1. To study the effect of upstream freestream turbulence and the periodic unsteady wake on the blade tip heat transfer.
2. To study the effect of different tip geometries to reduce the leakage flow and associated tip heat transfer.

The experiments were performed in a low speed wind tunnel facility with a four-blade linear cascade. The steady state liquid crystal technique is used to obtain the blade tip heat transfer measurements. The present study focuses on using trip strips in different orientations, different types of squealers and cylindrical pin fins to reduce leakage flow and heat transfer.

Chapter 2

Experimental Set-Up

Figure 2.1 shows the overall layout of the facility and cascade test section. The test apparatus consists of a low-speed wind tunnel with an inlet nozzle, a turbulence grid, a spoked wheel type wake generator, linear turbine blade cascade and a suction blower. The rig is made of aluminum walls, except for the blades and the shroud window cover plate, which are made from acrylic material. The cover plate is 5.04 cm thick. The schematic layout of the experimental setup is shown in Figure 2.2.



Figure 2.1. The overall layout of the facility and cascade test section.

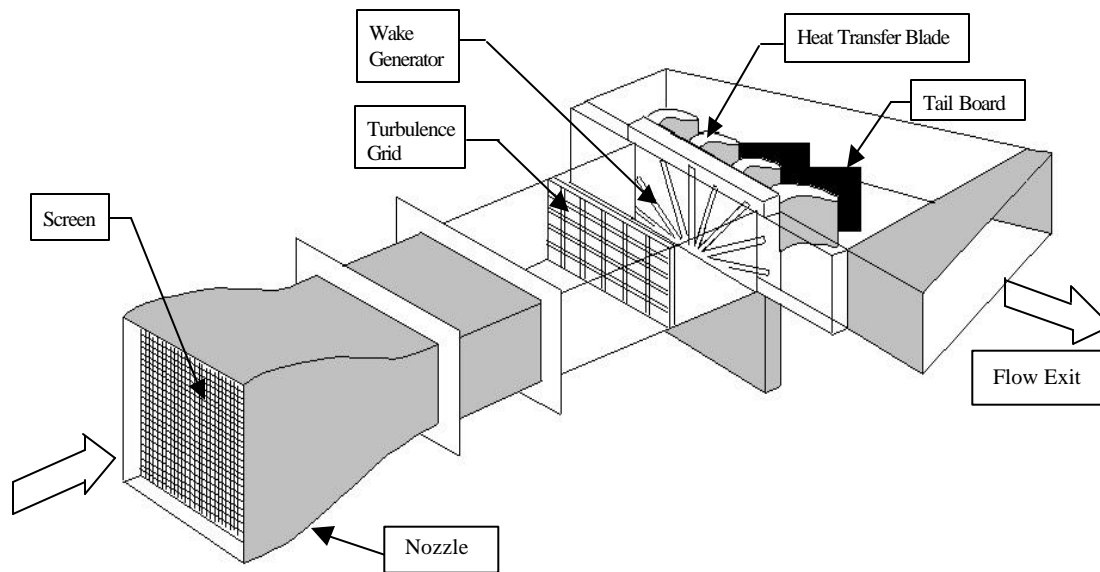


Figure 2.2. The schematic layout of the experimental setup.

The detailed description of all the different components of the set-up is explained in the following paragraphs.

2.1 Inlet Nozzle

The inlet nozzle to the facility has a top and bottom surface that is a 4th order polynomial curve. The nozzle has 3 inlet screens to assist in breaking up turbulent eddies of inlet airflow. The inlet dimensions 56 cm by 61 cm of converging inlet nozzle followed by a rectangular channel of dimension 56 cm by 20.32 cm.

2.2 Turbulence Grid

A turbulence-generating grid is placed in this channel 44.67 cm upstream of cascade leading edge as shown in Figure 2.3. This grid is composed of 6.35 cm diameter wooden bars arranged in a cross-bar fashion with spacing of 2.54 cm between the rods in

both directions. The width and height of the grid is the same as that of the rectangular channel. The open area ratio of the grid is 66.8 percent. The grid was designed to produce isotropic turbulence intensity of about 5% near the blade leading edge.



Figure 2.3. Turbulence Grid and Wake Generator as assembled in test cabinet.

2.3 Wake Generator

In order to simulate the effect of the stators on the airflow that passes over the turbine blades, the wake generator is installed upstream of the blades. In a real turbine engine, there is a gap in the airflow after it passes over the trailing edge of a stator. This is because the air has to pass on either side of the stator, and since the stator's trailing edge is not sharp, the airflow cannot rejoin smoothly. Due to the fact that the disruption in airflow is caused by the trailing edge, using rods with the similar diameter as a stator's trailing edge thickness simulates these stators. The rods pass through the test section cross-sectional area to properly mimic the stators' effect. The wake generator rotates

clockwise, as seen from the inlet, in order to properly recreate the flow conditions in the actual turbine stage. The wake generator spins in the direction opposite to the spin direction of the rotor of the real turbine and the blades are held stationary.

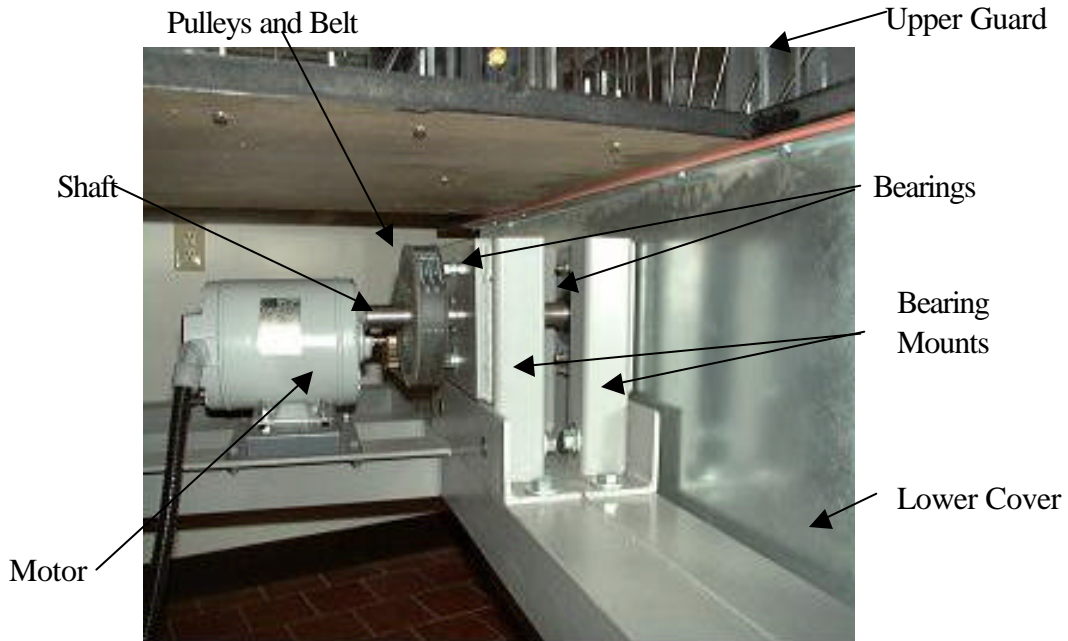


Figure 2.4. Wake generator drive components.

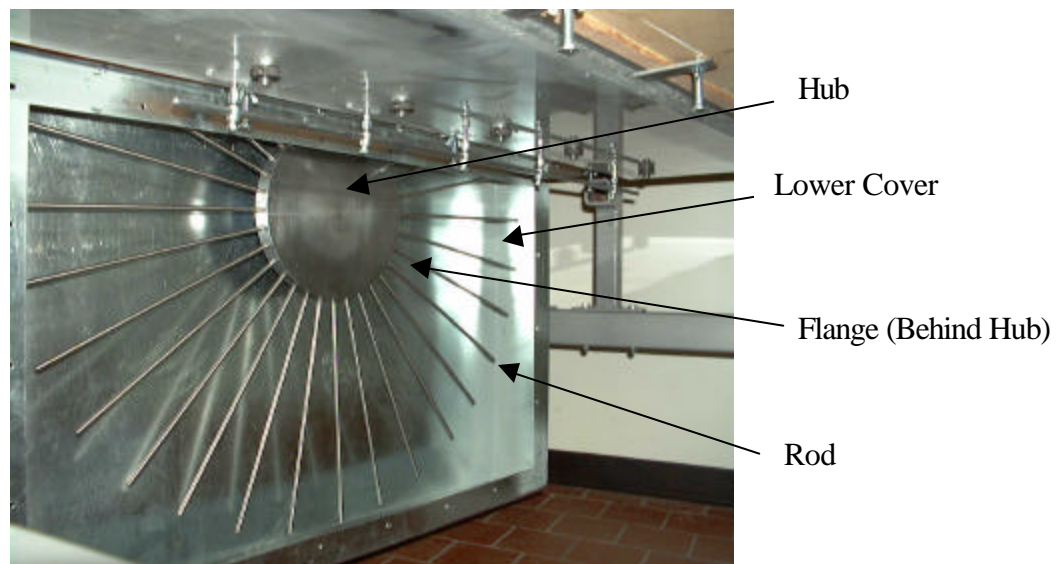


Figure 2.5. Wake generator hub and rod assembly.

As shown in the Figures 2.4 and 2.5, the rods are threaded into the hub that is bolted to a flange. The flange is threaded to accept a shaft, which is driven by a motor via a belt and pulley system. There are 32 hollow rods in it, with each rod having an outside diameter of ¼ inch and inside diameter of 1/8 inch. The wake generator is driven by 4 hp motor. The wake Strouhal number is adjusted by using frequency controller for controlling the motor speed. A DT-36M digital photo tachometer in the frequency controller is used to measure rotation speed.

The Strouhal number is a dimensionless parameter that represents the wake shedding frequency. It is the ratio of rotational speed and axial flow velocity. This wake shedding frequency was used to model the effect the stators would have on the airflow. The following equation was used to calculate the Strouhal number:

$$S = \frac{2\pi N(d/12)n}{60V}$$

where S = Strouhal Number (dimensionless)

N = Required Rotation Speed of Wake Generator (rpm)

d = Diameter of the Rods (inch)

n = Number of Rods

V = Velocity of the Cross-Flow Air (ft/s)

2.4 Test Section

The cascade as shown in Figure 2.6(a,b) has four blades. Each blade has an axial chord length of 12 cm and span of 20.32 cm. The blade spacing (S) at the cascade inlet is 19.06 cm. The relative flow angles at the blade inlet and exit and the throat aspect ratio (the span divided by the throat width) are not disclosed due to proprietary requirements. The two end blades form the outer edge of the cascade guiding the flow through the middle three passages. One of the middle blades serves as the test blade location. The

blade can be interchanged to obtain pressure measurements. All the blades are machined out of plexiglass. The blade shapes were cut out of 5.04-cm thick plexiglass sheet and four cuts were stacked up and glued together to obtain one blade for the cascade.

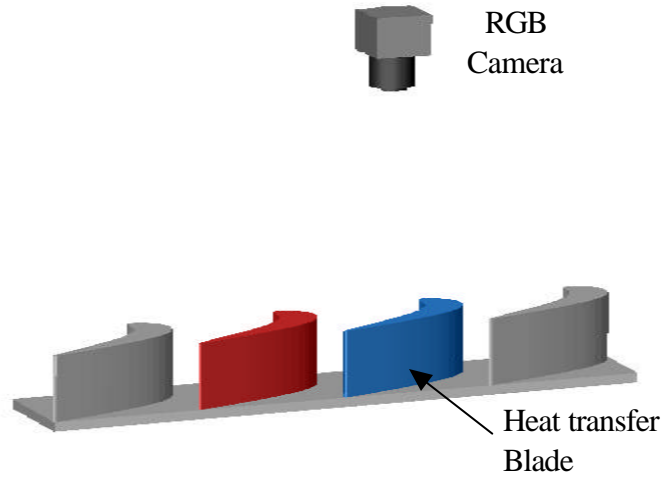


Figure 2.6(a). Schematic layout of the back view of test section.

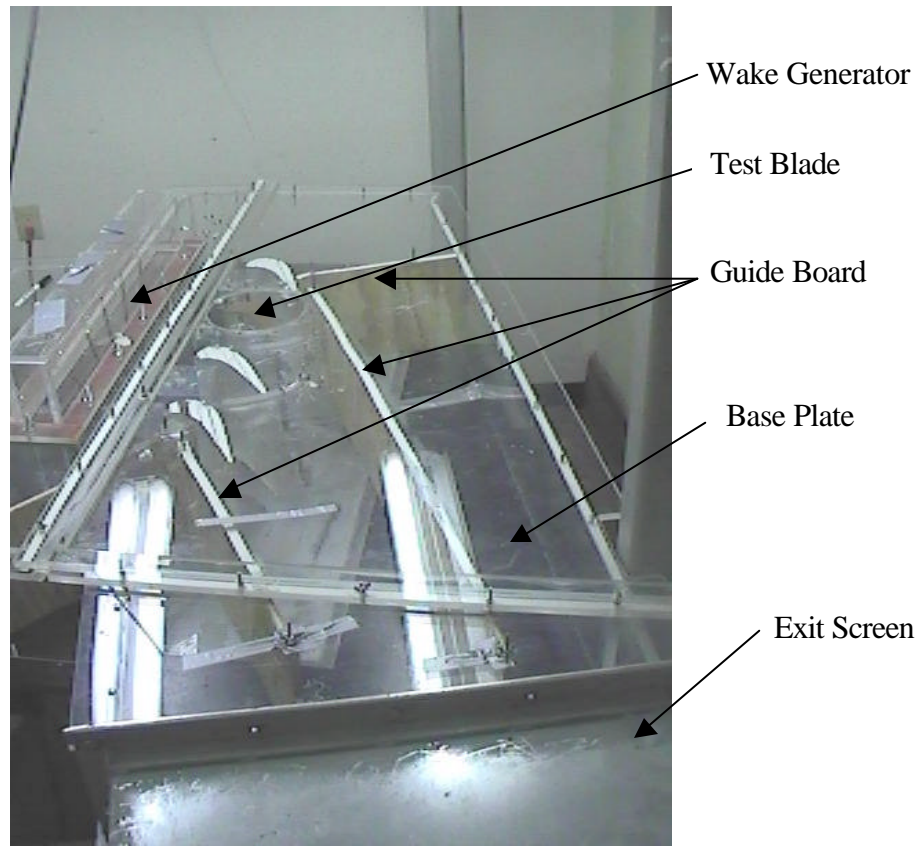


Figure 2.6(b). Overhead view of test section.

2.4.1 Test Blade

The heat transfer blade that serves as the test blade is shown in Figure 2.7. The test blade has a tip gap clearance of 1.5625% of the blade height, while remaining three blades do not have a tip gap clearance. The top surface of the plexiglass blade is covered with kapton. A kapton sheet is used between the plexiglass blade and heating wire to provide electrical insulation and heat transfer between them. A thin copper-plate heater of thickness 0.79 cm is placed over the plexiglas blade, which is heated underneath by a heating wire distributed uniformly. In the trailing edge the heating wire is not dense because blade is relatively thin in this region. This may ensure the uniform heating of the blade. A kapton sheet is placed between the copper plate and heating wire to provide electrical insulation and increase the heat conduction from the wire to the copper plate. The 2-D regions along the blade edges may produce some non-uniformity because most of the disturbances. A liquid crystal sheet of known color range (R30C5W) with red beginning at 30°C and a bandwidth of 5°C was then glued to the top of the copper plate.

Figure 2.8 shows the test blade with surface pressure taps. Pressure taps were placed on the blade surface at 60% span and 90% span to measure the static pressure distributions on the blade surface at different span locations. There were 154 static pressure taps placed on the shroud of the blade with a tip clearance as shown in the Figure 2.9. Some of the pressure taps are placed outside the edge of the blade tip to see how the flow behaves while approaching the blade tip. The shroud pressure distributions were obtained to characterize the leakage flows with different tip sealing geometries. Each static pressure tap was connected to a 32-channel NetScanner Pressure Systems.

Kapton sheet

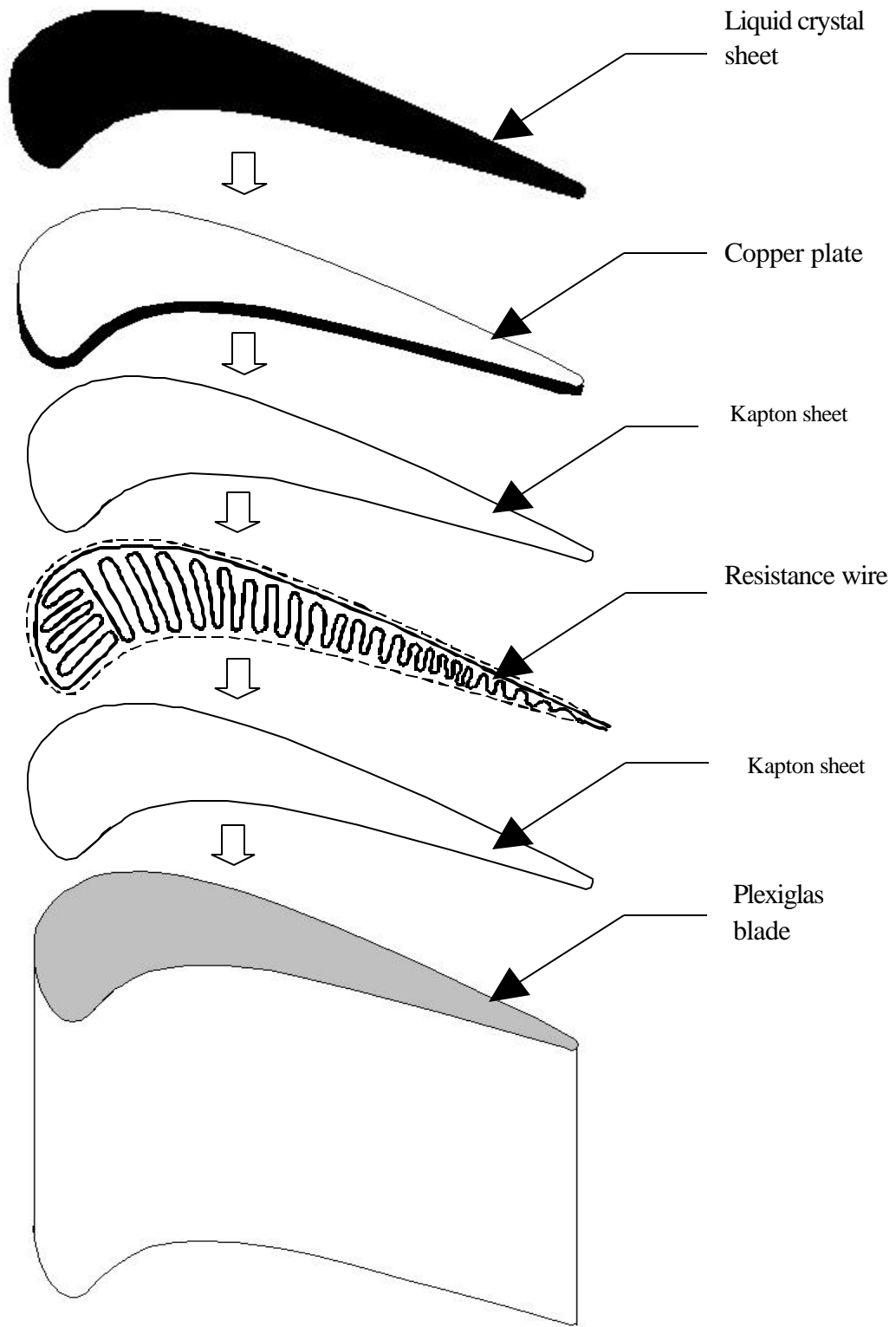


Figure 2.7 The complete description of the Heat Transfer Test Blade.

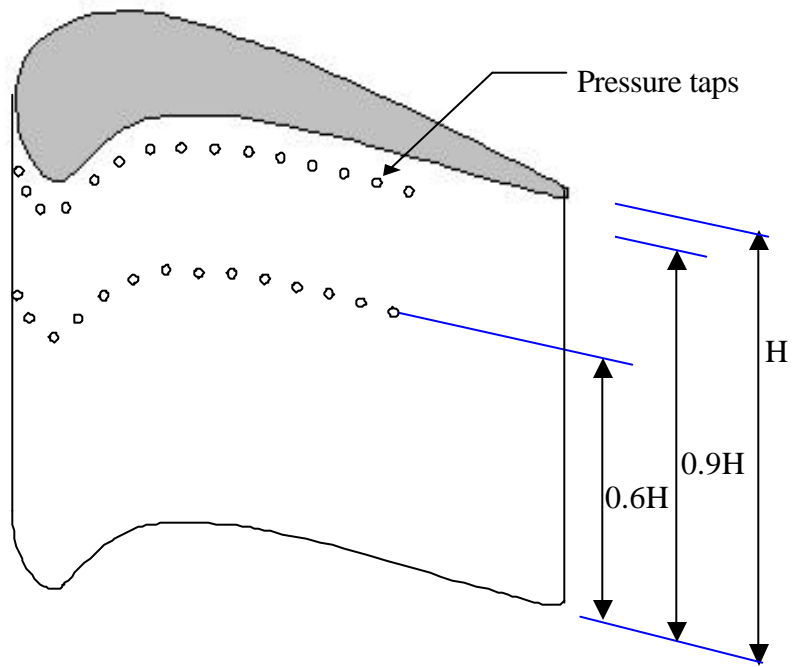


Figure 2.8. The location of the pressure taps on the blade surface at different span locations.

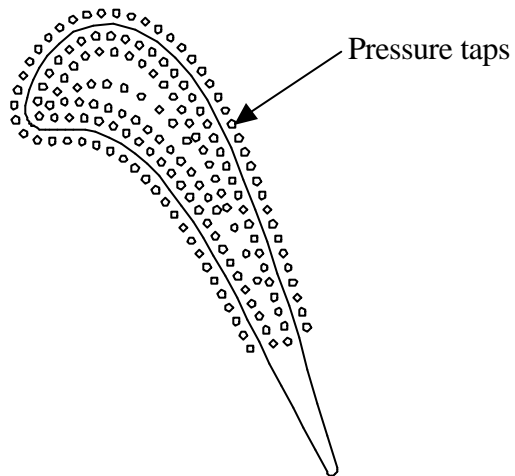


Figure 2.9. The location of the pressure taps on the shroud surface above the blade

2.4.2 Guide Board

In order to equally distribute the flow in all the three blade passages, guide boards are placed behind the plates in the test section. These guide boards are made up of wood and have thickness 1.27 cm and height 20.32 cm and are adjustable.

2.5 Description of Different Proposed Tip Geometries

For the tip sealing geometries, the ribs or trip strips at different orientations, squealers and cylindrical pin fins are used to reduce the leakage flow over the tip. The detailed description of all the ten tip geometry cases is explained in the following sections.

2.5.1 Plain Tip

Case 1 is the plain tip case with the tip clearance at 1.5625% of the blade height. The leakage flow direction was determined from the pressure distributions from the plain tip case.

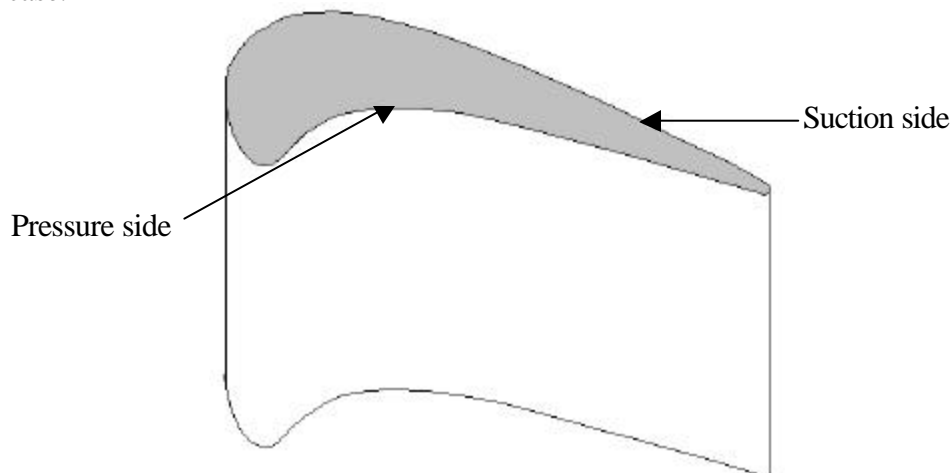


Figure 2.10. Plain Blade tip configuration.

2.5.2 Ribs

All the trip strips are 3.17-mm square in cross-section. Case 2 is for trip strips placed 25.4-mm apart with the trip strips orthogonal to the leakage flow direction. Case 3 is for the trip strips at 102° angle to the mainstream flow and slightly turned away from

the leakage flow with a reduced spacing of 18.7-mm. Case 4 is for the trip strips placed at $+9^\circ$ to the mainstream flow such that the strips are organized 25.4-cm apart to be along the leakage flow direction. Case 5 is for the trip strips placed at -9° to the mainstream flow such that the trip strips are tilted against the flow slightly with a spacing of 25.4-cm.

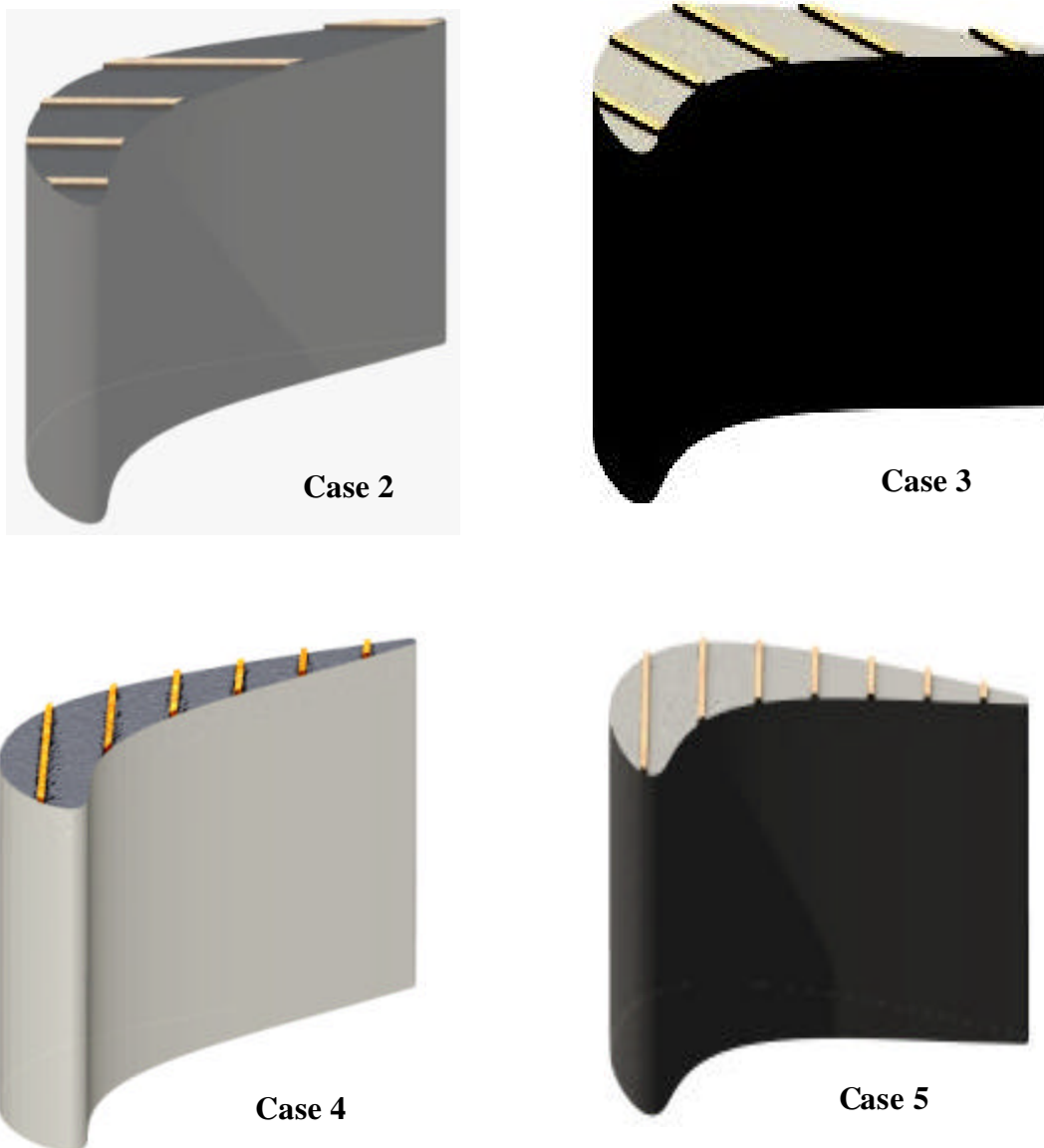


Figure 2.11. Blade tip with ribs in different orientations.

2.5.3 Cylindrical Pin Fins

Case 6 is for the tip with cylindrical pin fins attached to the tip surface only. The pin fins are 6.35-mm in diameter and 3.68-mm tall with a spacing of 25.4-mm. The pins are arranged in a staggered configuration on the tip. The first pin is placed at the leading edge of blade tip.



Figure 2.12. Blade tip with cylindrical pin fins.

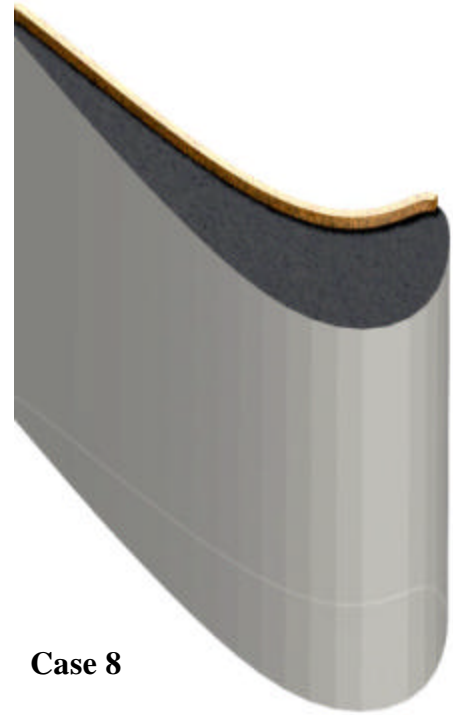
2.5.4 Squealers

All the squealers are with the width and depth of 3.17 mm. Case 7 is for the tip with partial squealer on the suction side of the blade tip. Case 7 is for the tip with partial squealer on the suction side of the blade tip. Case 8 is for the tip with partial squealer on the pressure side of the blade tip. Case 9 is for the tip with partial squealer on the edge of the blade tip. Case 10 is for the tip with full squealer on the suction side of the blade tip. The tip gap above the trip strips, pin fins and squealers is maintained at 1.5625% of the blade span.

The Figure 2.14 shows the top view of all the tip sealing geometries studied. All the angles are given with respect to the mainstream flow direction.



Case 7



Case 8



Case 9



Case 10

Figure 2.13. Blade tip with different kinds of squealers.

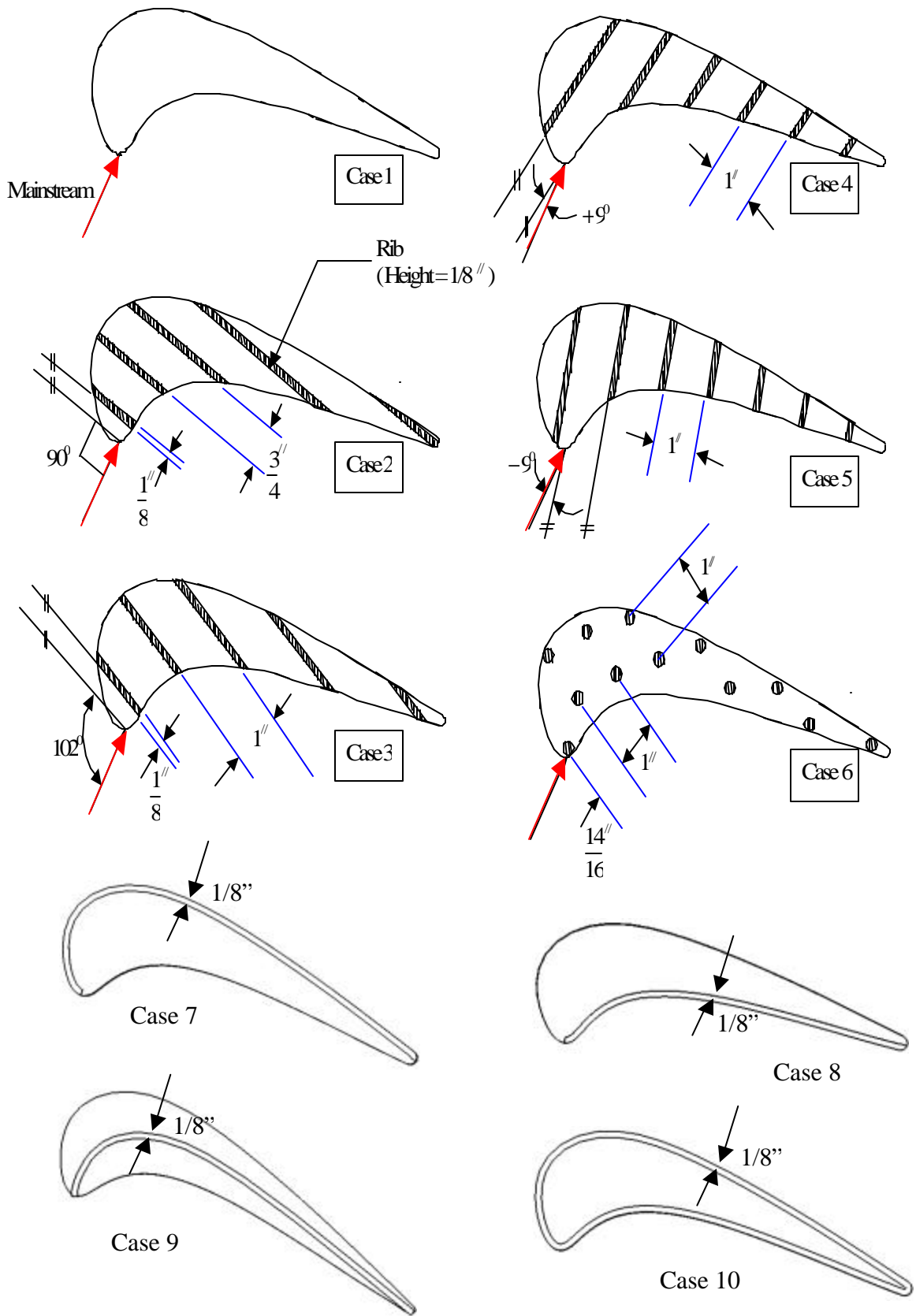


Figure 2.14. Top view of the Blade tip for all the different configurations tested.

The experiments were run for the five flow conditions for all the above ten-blade tip geometries.

1. No wake and no grid (NW-NG).
2. No wake and with grid (NW-WG).
3. With wake (Strouhal Number 0.2) and no grid (S02-NG).
4. With wake (Strouhal Number 0.4) and no grid (S04-NG).
5. With wake (Strouhal Number 0.4) and with grid (S04-WG).

Chapter 3

Data Acquisition Systems

3.1 Visual Image Processing System

A schematic layout of the image processing system used for this test facility is shown in the Figure 3.1. A Plunix RGB camera is placed right above the tip surface of the heat transfer blade location as shown in Figure 3.2. Lights are mounted on the frame that holds the camera in position. This camera connects to a CFG 24-bit frame grabber board in a PC. Image processing software (Optimas v6.5) communicates with the frame grabber board. The camera records the local RGB value on the heat transfer blade surface. A macro in Optimas was developed to convert RGB values to the hue value at that instant of time when the blade surface achieves steady state.

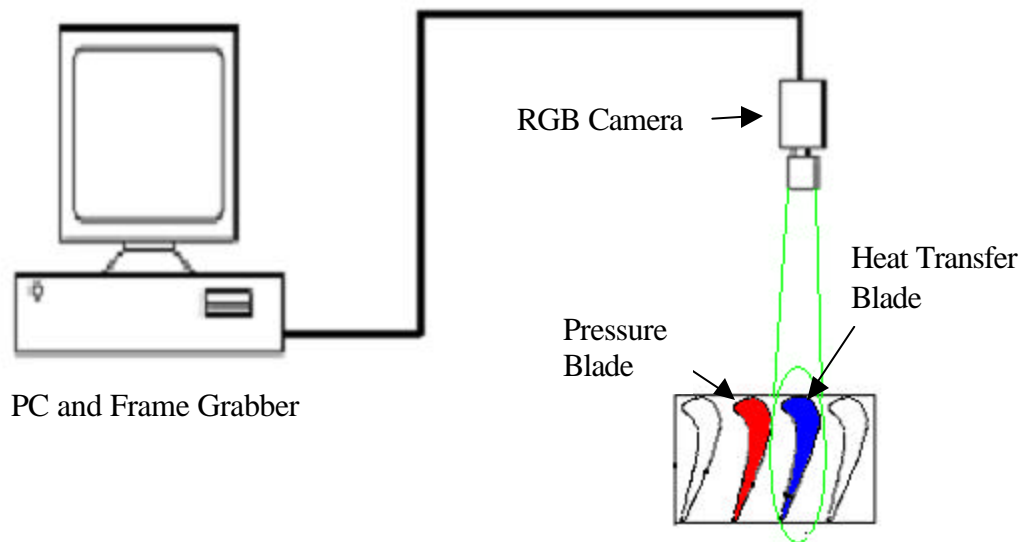


Figure 3.1 A schematic layout of the image processing system.



Figure 3.2 A Plunix RGB camera

3.2 Pressure Data Processing System

A schematic layout of the pressure measurement system used for this test facility is shown in the Figure 3.3. The pressure system, NetScanner, Model 98RK is used for all pressure measurements. Each pressure tap is connected to the 1/8-inch nylon tube that is connected to 1/16-inch nylon tube through the reducing connector. The latter tube is connected to each channel in the two 16-channel ports on the pressure system. There are 32 channels in the pressure system, so in order to take the reading of 154 pressure taps the experiments are repeated five times to obtain at the each tip location. Before obtaining the reading, the pressure system is calibrated with respect to the atmospheric pressure.

3.3 Hot Wire System

A single calibrated hot wire shown in Figure 3.4(a) is used to measure the instantaneous velocity from which the time mean turbulence intensity and ensemble-averaged mean velocity can be calculated. The hot wire sensor is vertically oriented at the

inlet of the pressure side passage of the test blade 15.24 cm downstream of the wake generator. It is connected to a three-channel TSI IFA 300 Constant Temperature Anemometer (CTA) shown in Figure 3.4(b). A 250 kHz Data Translation DT2831G A/D board installed in the PC to convert the analog signal from the anemometer.

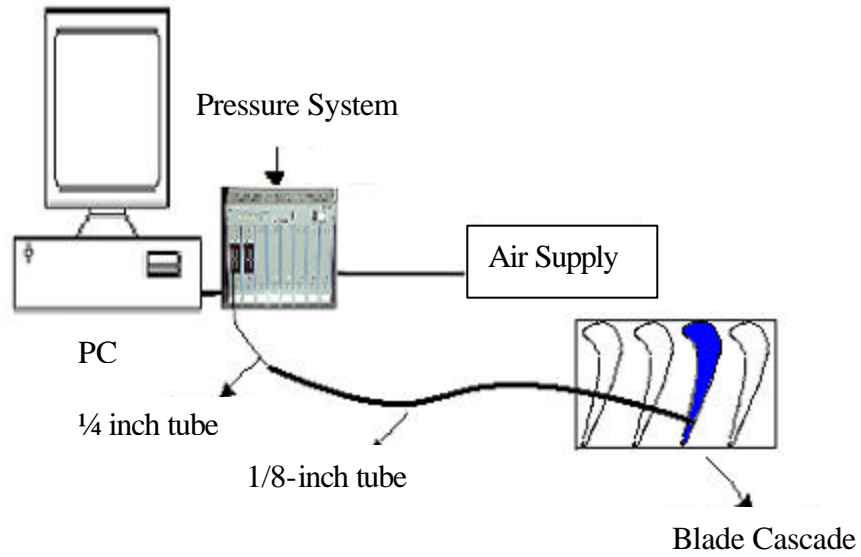


Figure 3.3 A schematic layout of the pressure measurement system.



Figure 3.4(a) A single calibrated hot wire probe.



Figure 3.4(b) Hot Wire system.

Chapter 4

Procedure and Data Reduction

4.1 Heat Transfer Experiments

The first step in the experimental procedure is to calibrate the liquid crystal color to temperatures. The calibration was done in-situ with a thermocouple placed on the liquid crystal sheet. The camera was focused on the region around the thermocouple. The image-processing system records the Hue of the color and the temperature was measured using a temperature recorder. The image-processing system using a simple macro in OPTIMAS software converts local red green blue (RGB) value to Hue Saturation Index (HSI) value.

Hue can be obtained as follows.

$$H_1 = \frac{p}{2} - A \sin \left[\frac{(0.5 * ((R - G) + (R - B)))}{\sqrt{((R - G)^2 + (R - G) * (G - B))}} \right]$$

$$H_2 = H_1 * \frac{180}{p}$$

if $H_2 > 180$

$$H_2 = 360 - H_2$$

$$\text{Hue}(H) = \frac{H_2}{360} * 255$$

The Hue values vary from 0 to 255 (8-bit scale). The macro is written in Optimas V 8.0 to convert RGB values to HSI values at each pixel location.

The liquid crystal sheet was heated by applying known current and voltage to the heater underneath the sheet. The voltage of heater is varied slowly increase the heater temperature by about 0.1°C and allowed to come to steady state. This change in the local temperature and the liquid crystal color change around the thermocouple are recorded simultaneously. Using the macro, the RGB values (color change) are converted to Hue of the color. The Hue value was plotted against the temperature to obtain the calibration curve. Camci et al. (1991) provide a detailed description of Hue-based liquid crystal measurement technique. A Hue-Temperature relationship is obtained from the curve as shown in the Figure 4.1.

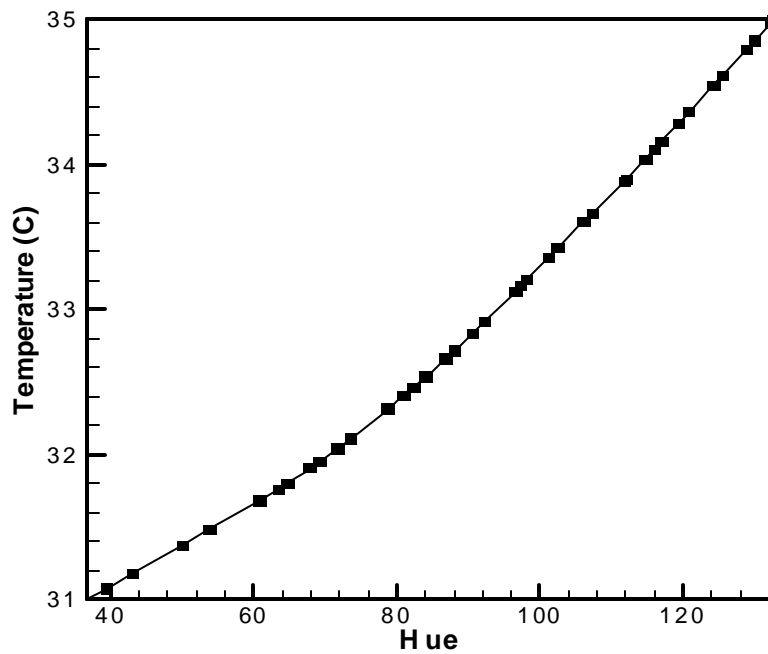


Figure 4.1 Hue- Temperature calibration curve.

The linear polynomial relation below is obtained from the plot.

$$Temperature = 0.047 * Hue + 28.619 \dots\dots\dots(4.1)$$

The temperature at every location on the entire blade tip surface is obtained using this relation for the same illuminating conditions. If the illuminating conditions are changed a new calibration curve is required as the calibration curve could be affected by the change in the illumination.

The suction blower is turned on to start the mainstream flow through the cascade. Once the flow is steady, the heater is turned on using the electrical supply and a variac. The variac is used to control the current and voltage into the heating wire. The heating wire heats up the copper plate and the copper plate heats up the liquid crystal layer. The heat flux is increased till most of the blade is either green or red. The Hue calibration is not very reliable in the blue color range, as the curve tends to plateau with increasing temperature. To avoid this, color changes are limited to red and green. Once the surface is mostly green, the heat flux is maintained constant until the test surface achieves steady state. This typically takes about 30-45 minutes. The image is then captured and the local Hue values are obtained at every pixel on the blade tip surface. The wall surface heat flux is calculated from the known voltage and current and the blade tip surface area. The local heat transfer coefficient is calculated from the relation:

$$h = \frac{q''_{elec} - q''_{loss}}{(T_w - T_\infty)} \dots\dots\dots(4.2)$$

where q''_{elec} is the applied electrical power per unit area, and q''_{loss} is the losses due conduction, natural convection, and radiation. This was estimated to be about 6% of the applied heat flux. The local wall temperature T_w is calculated from the local hue measurement and T_m is the oncoming free-stream temperature measured upstream of the cascade. A computer code is written in C-language, which converts the Hue to the local

surface temperature using the equation 4.1, and then calculates the local heat transfer coefficient using the equation 4.2.

4.2 Hot Wire Measurements

A TSI hot wire system was used with a probe model 1260A-T15 for the velocity and turbulence measurements. The hot wire sensor (probe) is first calibrated using a calibrator, according to the velocity range in which the probe is to be used. In these experiments, it is calibrated for velocity range of 1-50 m/sec. A calibration curve is obtained. The calibration is repeated until a smooth curve is obtained. After obtaining a smooth calibration curve, the probe is removed from the calibrator. The probe is vertically oriented at the inlet of the pressure side passage of the test blade 15.24 cm downstream of the wake generator to record the flow measurements.

In order to capture the smallest variation in the velocity it is important to increase the sample rate. But increasing the sample rate increases number of sample points resulting in a lot of memory allocation on the computer hardware. Hence, the data was obtained using different sample rates to determine optimum sample rate. The flow measurements were obtained for all the different flow conditions for the plain blade tip at a sample rate of 200,000 samples per sec. Then finally using the Microsoft Excel the variation of velocity was plotted against the time.

4.3 Pressure Measurements

Each pressure tap on the blade/shroud is connected to a one channel on the 32-channel Pressure System. The system is calibrated with respect to atmospheric pressure before obtaining measurements. After the suction blower is turned on to start the mainstream flow through the cascade and the flow is steady, the pressure at each tap

location is measured. Twenty-five readings of each pressure tap are obtained with one sec intervals. The average of these values is determined and using the Tecplot software the pressure value of each tap are plotted against the x and y- coordinate of that pressure tap with respect to the blade leading edge location. The turbulence intensity is calculated from the instantaneous velocity data obtained. The grid produces the isotropic turbulence. So, the turbulence intensity is given by

$$Tu = \frac{\overline{u'}}{u_{\infty}} \quad (4.3)$$

4.4 Experimental Uncertainty

The experimental uncertainties in the local heat transfer coefficient measurement are calculated based on Kline and McClintock (1953) with 95% confidence. The uncertainty in Hue measurement, the Hue-temperature relation, free-stream temperature measurement, and heat flux input, and loss estimation affect the heat transfer coefficient measurement. The individual uncertainties are listed below:

Voltage measurements (V):	2.5%
Current measurements (I):	2%
Mainstream Temperature (T_{∞}):	1%
Hue measurements (Hue):	5%
Area measurements (A):	1%

The procedure to calculate the experimental uncertainty is given below:

$$Q'' = \frac{V * I}{A} \dots\dots\dots(4.4)$$

The combined uncertainty in the calculating the Q'' is

$$u_{Q''} = \pm \left\{ \left(\frac{I}{Q''} \frac{\partial Q''}{\partial I} \frac{dI}{I} \right)^2 + \left(\frac{V}{Q''} \frac{\partial Q''}{\partial V} \frac{dV}{V} \right)^2 + \left(\frac{A}{Q''} \frac{\partial Q''}{\partial A} \frac{dA}{A} \right)^2 \right\}^{1/2}$$

$$u_{Q''} = \pm \left\{ \left(\frac{I}{Q''} \frac{V}{A} \frac{dI}{I} \right)^2 + \left(\frac{V}{Q''} \frac{I}{A} \frac{dV}{V} \right)^2 + \left(\frac{A}{Q''} \left(\frac{-VI}{A^2} \right) \frac{dA}{A} \right)^2 \right\}^{1/2}$$

$$u_{Q''} = \pm \left\{ \left(\frac{dI}{I} \right)^2 + \left(\frac{dV}{V} \right)^2 + \left(-\frac{dA}{A} \right)^2 \right\}^{1/2}$$

As we know,

$$\frac{dI}{I} = 0.02, \quad \frac{dV}{V} = 0.025 \quad \text{and} \quad \frac{dA}{A} = 0.01, \quad \text{so we get}$$

$$u_{Q''} = \pm 0.0335$$

$$T = 0.047 * Hue + 28.619 \dots\dots\dots(4.5)$$

The uncertainty in the calculating the T is

$$u_T = \pm \left\{ \left(\frac{Hue}{T} \frac{\partial T}{\partial Hue} \frac{dHue}{Hue} \right)^2 \right\}^{1/2}$$

$$u_T = \pm \left(\frac{1}{1 + \frac{28.619}{0.047 * Hue}} \frac{dHue}{Hue} \right)$$

As we know $\frac{dHue}{Hue} = 0.05$, we get

$$u_T = \pm 0.0087$$

$$h = \frac{Q''}{(T - T_\infty)} \dots\dots\dots(4.5)$$

The combined uncertainty in the calculating the heat transfer coefficient h is

$$u_h = \pm \left\{ \left(\frac{T}{h} \frac{\partial h}{\partial T} \frac{dT}{T} \right)^2 + \left(\frac{T_\infty}{h} \frac{\partial h}{\partial T_\infty} \frac{dT_\infty}{T_\infty} \right)^2 + \left(\frac{Q''}{h} \frac{\partial h}{\partial Q''} \frac{dQ''}{Q''} \right)^2 \right\}^{1/2}$$

$$u_h = \pm \left\{ \left(\frac{-T}{(T-T_\infty)} \frac{dT}{T} \right)^2 + \left(\frac{T_\infty}{(T-T_\infty)} \frac{dT_\infty}{T_\infty} \right)^2 + \left(\frac{dQ''}{Q''} \right)^2 \right\}^{1/2}$$

$$\frac{dT}{T} = 0.0087, \quad \frac{dT_\infty}{T_\infty} = 0.01, \quad \frac{dQ''}{Q''} = 0.0335 \text{ and with average } T \text{ and } T_\infty, \text{ we get}$$

$$u_h = \pm 0.0478$$

Therefore, the experimental uncertainties in the measurement of local heat transfer coefficient calculated based on Kline and McClintock (1953) is 4.78%. Similarly the experimental uncertainty in pressure measurement is 0.2% and in the velocity measurements is 5%.

Chapter 5

Results: Flow and Pressure Measurements

5.1 Flow Measurements

The free-stream velocity at cascade inlet is 23 m/s and 58 m/s at the cascade exit. The cascade exit Reynolds number based on axial chord length is 4.83×10^5 . Five different flow conditions were studied for each tip geometry. The no grid and no wake case has a baseline turbulence intensity of around 1.4% and the upstream grid produces a turbulence intensity of 4.9% upstream of the cascade. Two different wake generator rotational speeds produce wake Strouhal numbers of 0.2 and 0.4. Figure 5.1 shows the velocity signature from four flow conditions. The baseline case with no wake no grid (NW-NG) produced a average turbulence intensity of 1.4%. The turbulence intensity with the turbulence grid (NW-WG) was 4.8%. With the unsteady wake superimposed on the grid, the periodicity of the wake passing is clearly evident. For the case with Strouhal number of 0.2, the wake passing period is 0.007-seconds. The case for the Strouhal number of 0.4 produces half the wake passing period of $S=0.2$ as expected. The periodicity for the passing wake is clearly evident from the velocity signatures. Table 5.1 summarizes the flow conditions and the associated turbulence intensity for each case.

Table 5.1 List of Flow conditions

Flow condition	Rods	Grid	Turbulence Intensity	Wake Strouhal No. (S)
NW-NG	No	No	1.4%	0
NW-WG	No	Yes	4.8%	0
S02-NG	Yes	No	1.4%	0.2
S04-NG	Yes	No	1.4%	0.4
S04-WG	Yes	Yes	4.8%	0.4

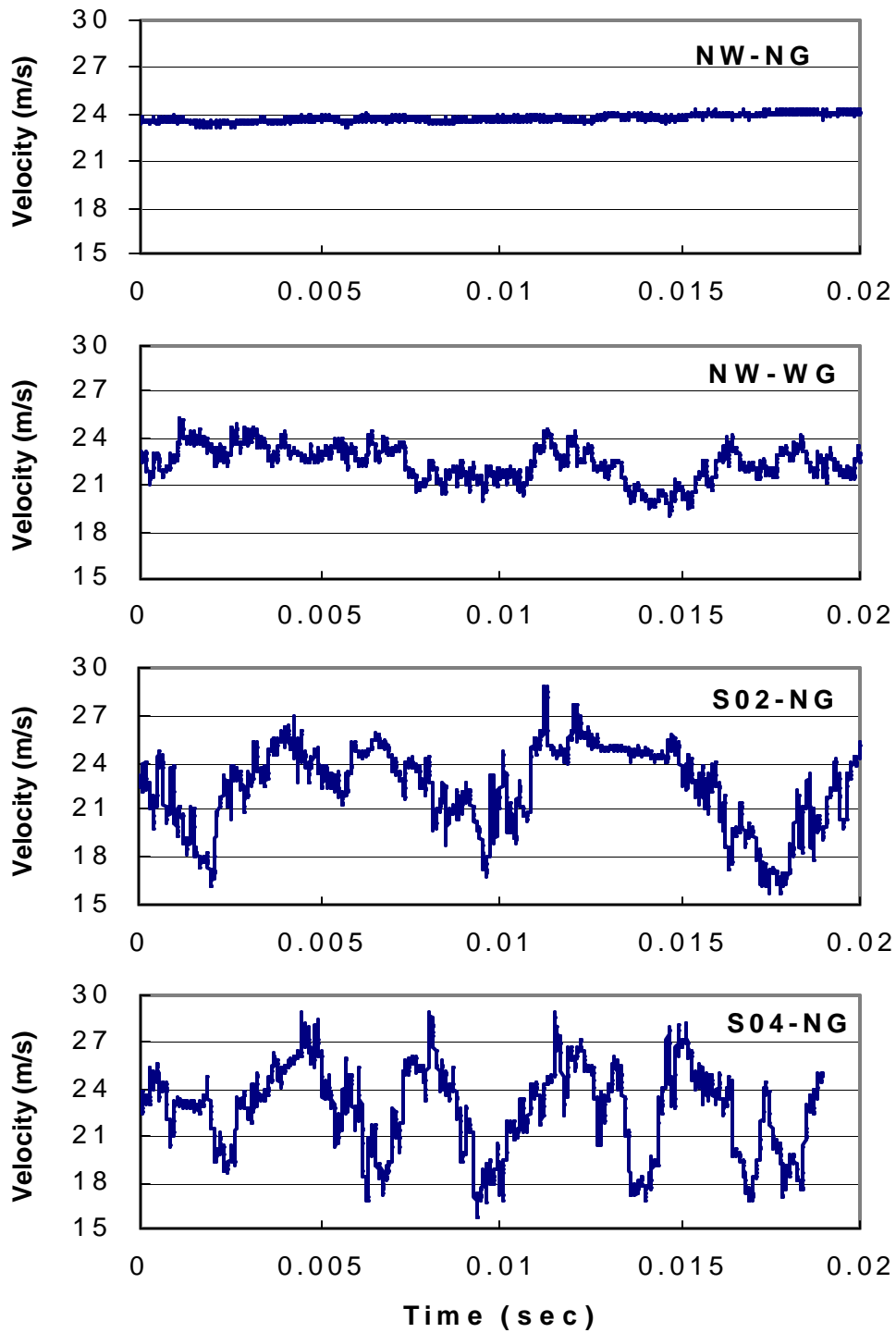


Figure 5.1. Velocity signature for the four flow conditions

5.2 Pressure Measurements

The flow in all three blade passages was equalized by moving the guide boards behind the cascade. The tailboards were adjusted till the leading edge velocities were uniform for all the three passages. Figure 5.2 presents the surface pressure distributions $\{(P_t - P_s)/P_t\}$ for the test blade at 60% and 90% span locations. The static pressure measurements were obtained for four different flow conditions. Results show that the upstream flow condition, whether wake or grid, does not affect the static pressure distributions on the blade surface significantly. This is true at both span locations. The pressure side shows almost uniform pressure over the entire surface. The lowest pressure occurs around 0.45C on the suction surface. The flow accelerates from the leading edge to 0.45C on the suction surface and then decelerates towards the trailing edge, as shown by the arrows.

Figure 5.3 shows the comparison of the pressure distributions at the two different span locations. The pressure side pressures are identical but at a span of 90%, the acceleration on the suction surface is slower than for 60% span location. This may be due to the tendency of the flow to migrate towards the tip at larger span location.

Figure 5.4 presents the static pressure distributions $\{(P_t - P_s)/P_t\}$ on the shroud for the plain tip with four different flow conditions. The effect of unsteady wake appears to show little effect on the shroud pressure distributions comparing case 1 and case 3. However, the presence of grid-generated turbulence appears to reduce the low pressure region in the middle of the blade and spreading the leakage flow.

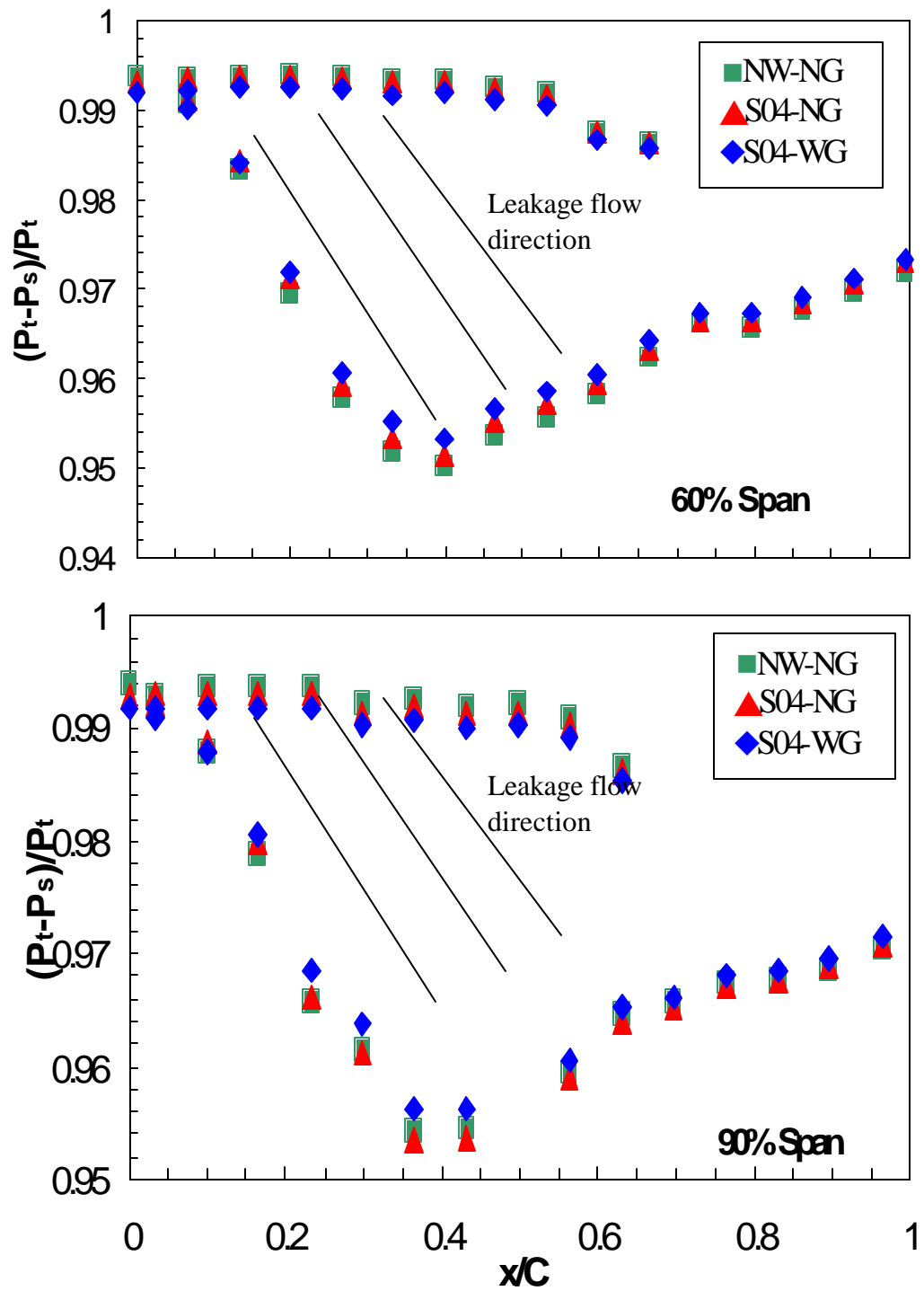


Figure 5.2 Surface pressure distributions on the test blade at different span locations.

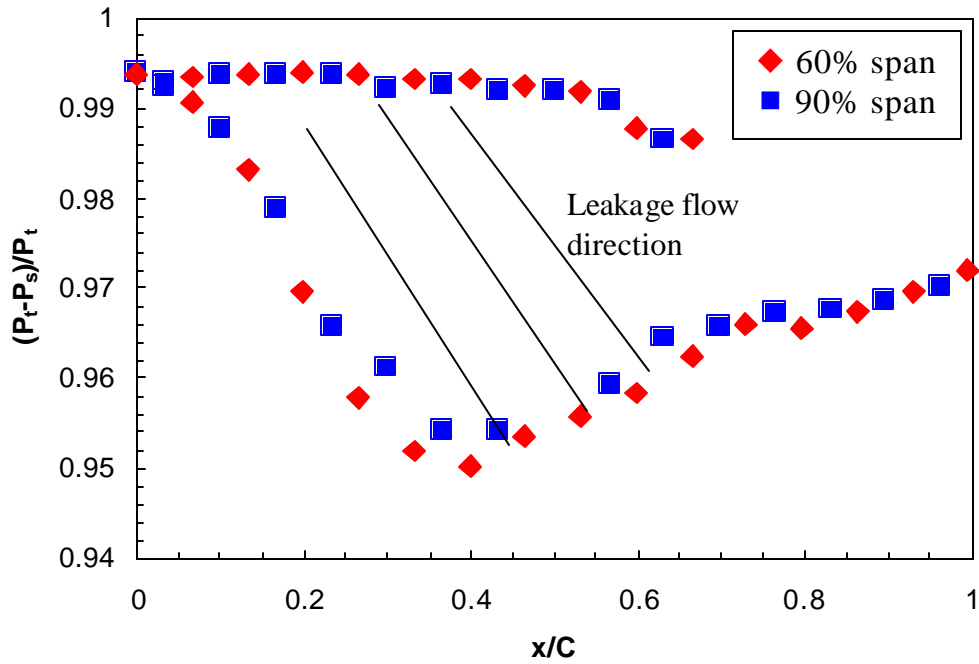


Figure 5.3 Comparison of surface pressure distributions for two different span locations.

Figure 5.5 presents the shroud pressure distributions for various tip geometries. The pressure distributions clearly show that the lowest velocities are obtained for Case 7, which is the suction side squealer. Case 10, full squealer, is also comparable. This shows that the squealers appear to be effective leakage flow sealing mechanisms. The ribs and pins do appear to reduce leakage flow over the tip compared to the plain tip but do not appear to be effective as the squealer geometries. As indicated by the squealers squeal the flow and reduce the overall leakage.

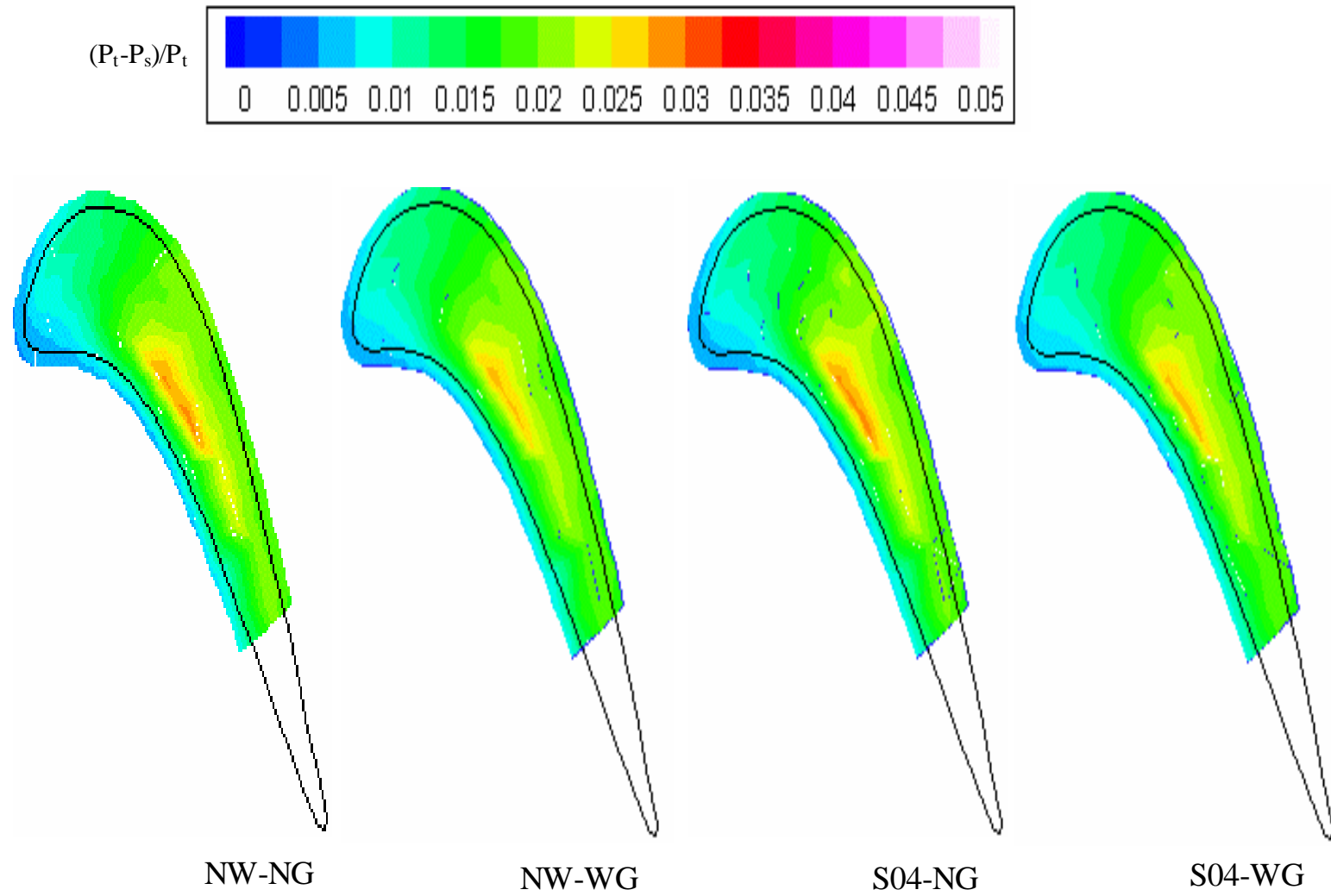


Figure 5.4 Static pressure distributions $\{(P_t - P_s)/P_t\}$ on the shroud for the plain tip under different flow conditions.

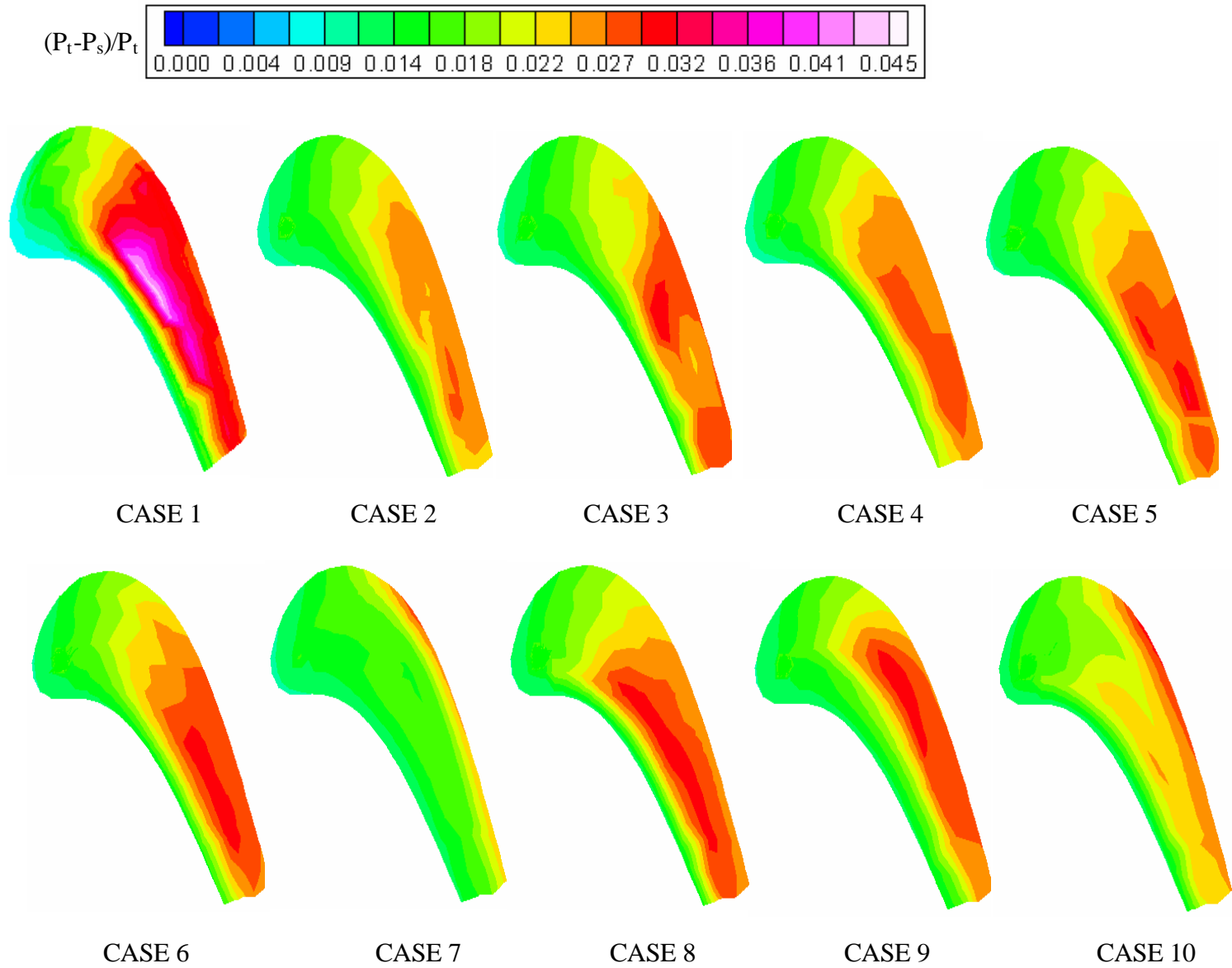


Figure 5.5 Static pressure distributions $\{(P_t - P_s)/P_t\}$ on the shroud for all the ten different tip configurations.

Chapter 6

Results: Heat Transfer Measurements

6.1 Effects of Flow Condition on the Tip Surface

Comparison of flow condition for Plain Tip (i.e. Baseline) Case

The Figure 6.1 presents heat transfer distributions under baseline conditions for the plain tip under different flow conditions.

- Flow with no wake and no upstream turbulence (NW-NG): The baseline case is the no wake and no grid with a low turbulence intensity of 1.4%. For this condition, heat transfer coefficient is highest along the blade tip trailing edge region. The lowest heat transfer coefficients are obtained in the middle of the leading edge region. Bunker and Bailey (2000) referred this region of low heat transfer as the “sweet spot”. From the pressure distributions on the shroud, it is clear that bulk of the leakage flow will follow the line along the strongest pressure gradient across the tip which is downstream of the leading edge region around $X/C=0.4-0.5$. Further downstream, the heat transfer coefficient is higher due to highly accelerated flow over the tip. The heat transfer coefficient is higher along the pressure side as compared to the suction side because of entrance flow effect. As the incoming flow separates from the inner edge of the pressure side a separation vortex is generated. Ameri et al (1997) and Sjolander and Cao (1995) observed the separation vortex phenomenon. The lower heat transfer coefficient on the suction side of the gap is because of the boundary layer develops at the pressure side and grows towards the suction side.

- Effect of Free Stream Turbulence (NW-WG): In the combustion chamber the turbulence is created during the mixing of fuel and air, which is simulated by the introduction of turbulence grid upstream of the blade cascade, which increases the turbulence intensity to 4.8%. As the mainstream turbulence increases, it disturbs the boundary layer and causes increase in the heat transfer coefficients. This is evident in both the Figure 6.1(a) and Figure 6.1(b), the heat transfer coefficients increases as compared to baseline case. The sweet spot region sees higher heat transfer coefficients. It can be summarized that the increase in free-stream turbulence enhances heat transfer closer to the leading edge of the tip gap.

- Effect of Unsteady Wake (S02-NG and S04-NG): The wakes induced by the spoked rotor also enhances the heat transfer. The explanation for this phenomenon is that due to the movement of the blades (hereby simulated by the rotating rods and keeping the blade fixed) flow gets turned which lead to non-zero incident angle of the inlet flow. This results in the shift of the actual stagnation line from the geometrical one. There is one more reason that the rotating rod cut the flow creating a velocity deficit on the blade tip. This periodic flow deficit causes the unsteadiness in the flow. This unsteadiness causes an increase in the overall tip heat transfer coefficient. When the wake speed is increased (i.e. Strouhal Number changed from 0.2 to 0.4), the periodicity increases as seen from Figure 5.1. This also increases the unsteadiness of the flow leading to higher heat transfer at the trailing edge as compared to $St = 0.2$ case as seen in Figure 6.1(a) and the Figure 6.1(b).

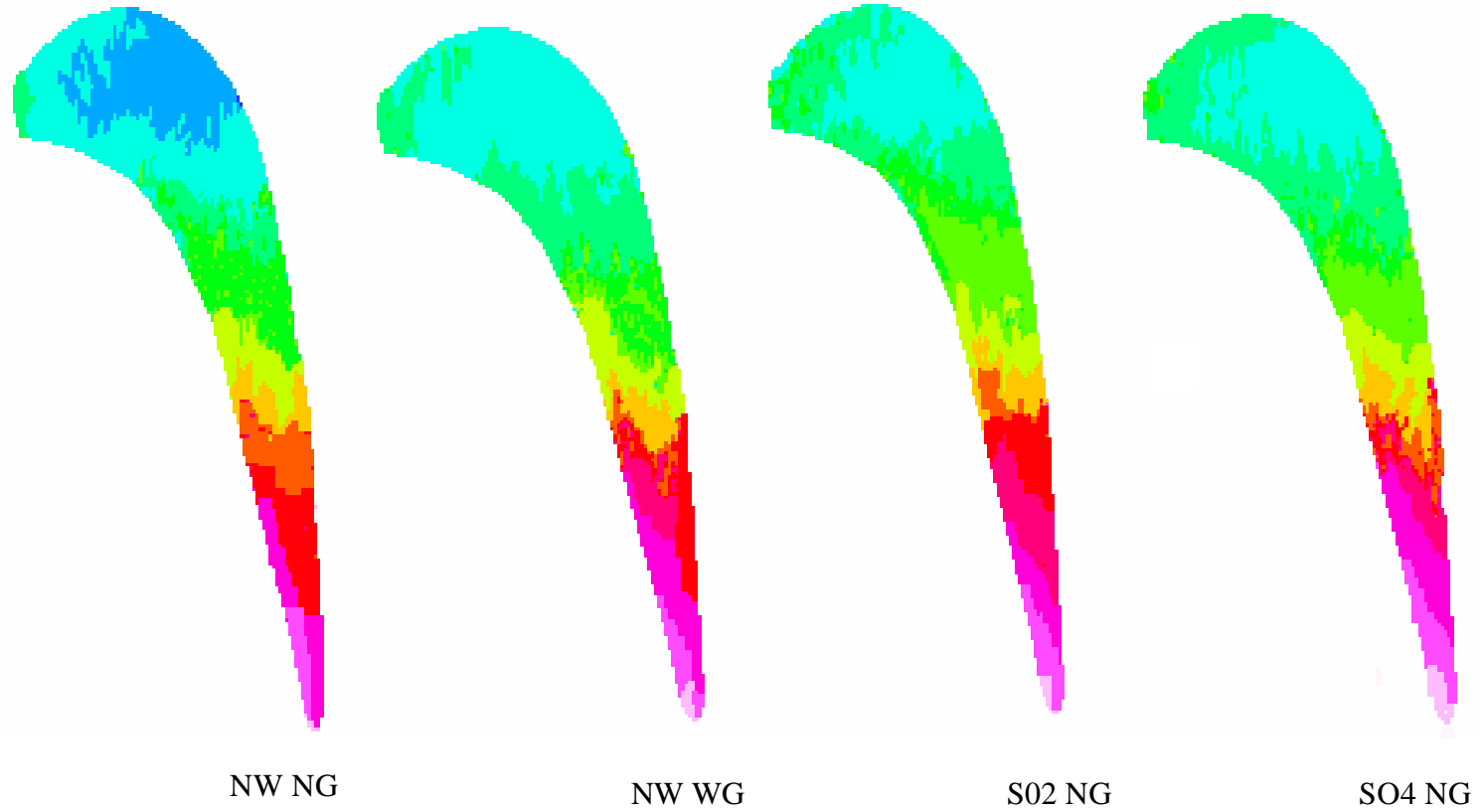
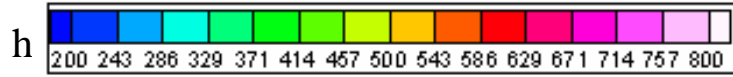


Figure 6.1(a) Detailed heat transfer coefficient distributions on plain tips (Case 1).

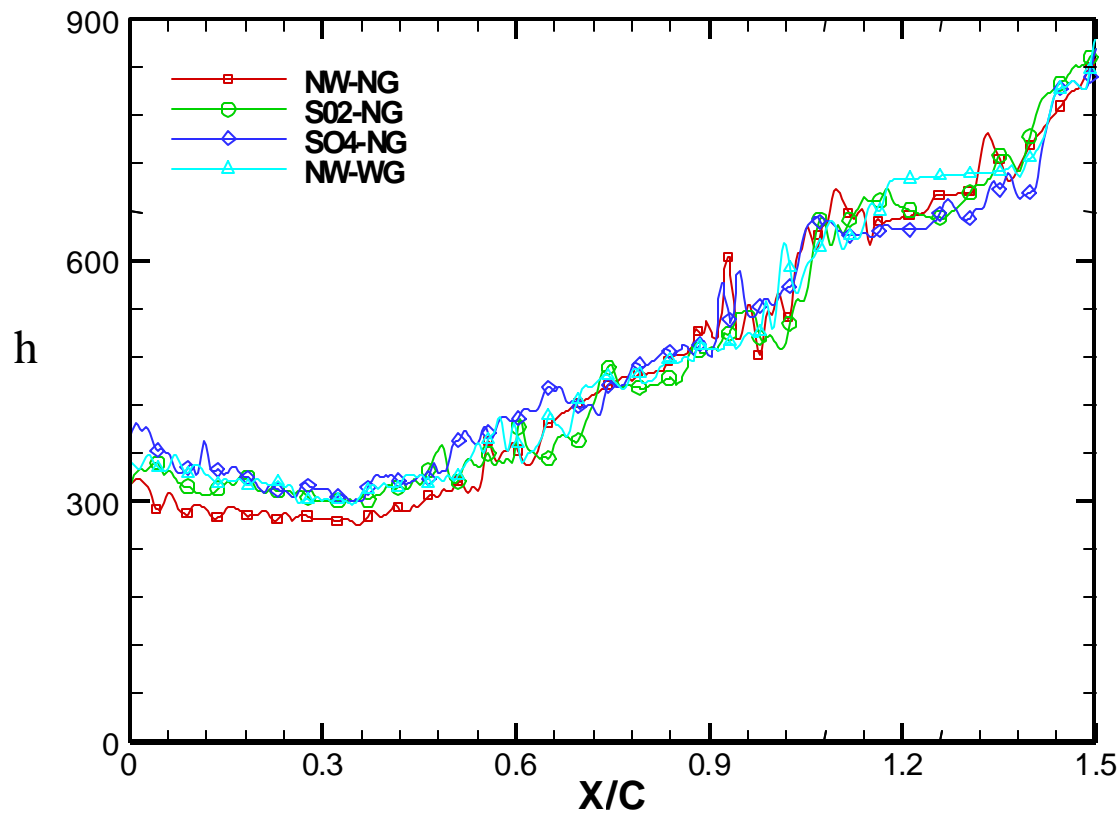


Figure 6.1(b) Effect of upstream flow condition on tip camberline heat transfer coefficient for baseline case.

Comparison of flow condition for Case 2

Figure 6.2 presents the effect of flow condition on tip heat transfer for the tip geometry, Case 2. For the no wake and no grid (NW-NG) case, the tip heat transfer coefficients obtained are lower than plain tip. With the introduction of the grid (i.e. WG-NW) the heat transfer increases because of the increase in turbulence. Expect for the trailing edge, this increase in the tip heat transfer coefficient is less as compared to the increase that takes place in plain tip case. Similarly, with the introduction of the wake (i.e. S02-NG) the increase in the tip heat transfer coefficient is small compared to the increase seen for plain tip case.

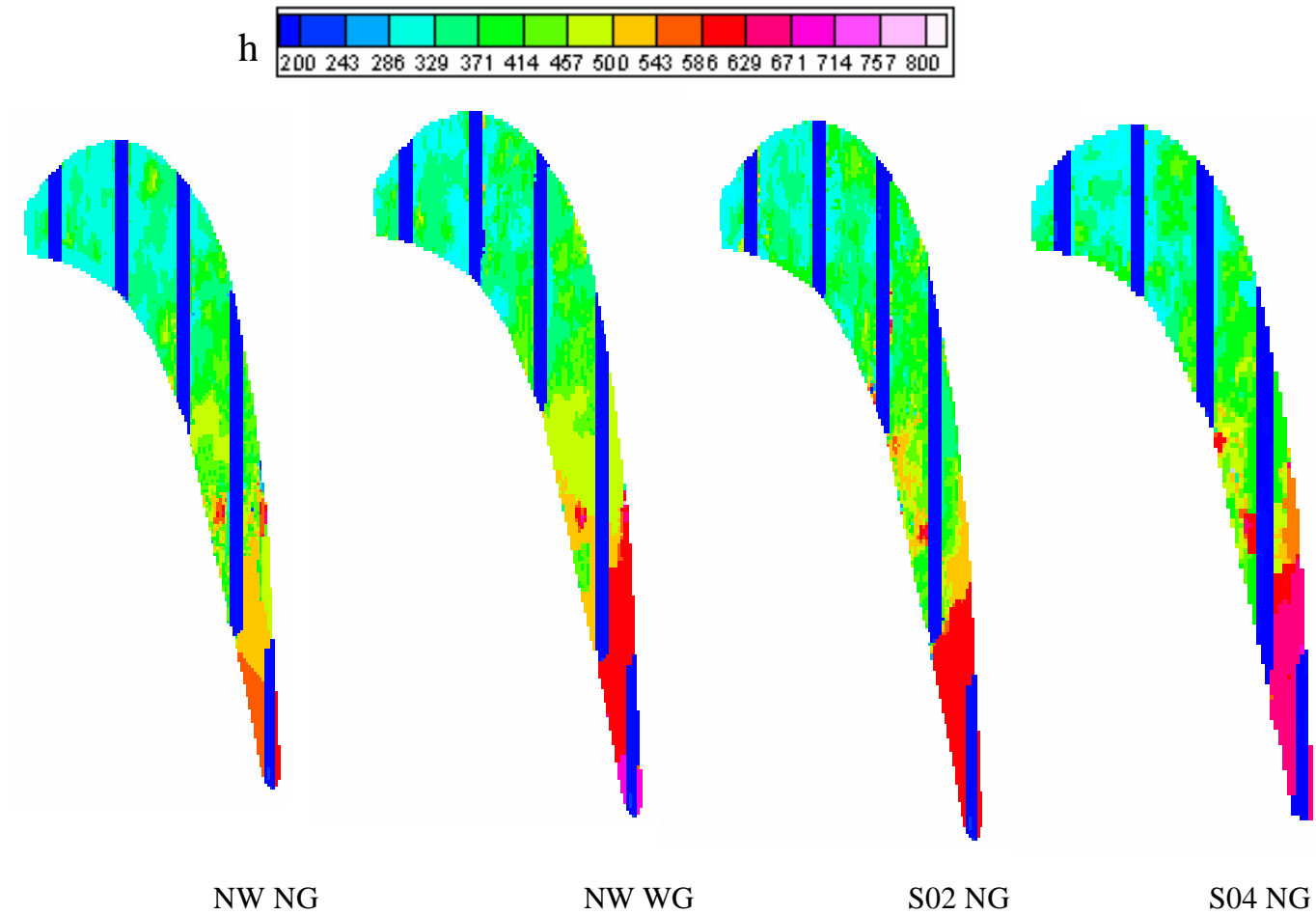


Figure 6.2(a) Detailed heat transfer coefficient distributions on tip with ribs against the flow 3-quarters inch away (Case 2).

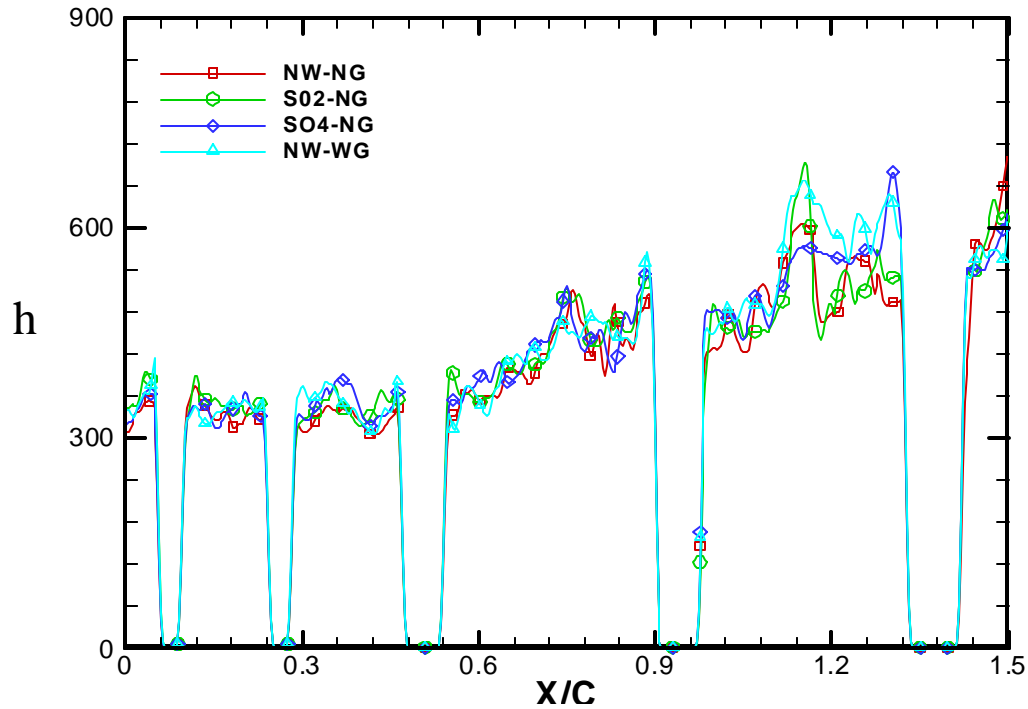


Figure 6.2(b) Effect of upstream flow condition on tip camberline heat transfer coefficient for Case 2.

Comparison of flow condition for Case 3

Figure 6.3 presents the effect of flow condition on tip heat transfer for tip geometry, Case 3. For the no wake and no grid (NW-NG) case, the tip heat transfer coefficients obtained are lower than plain tip. With the introduction of the grid (i.e. WG-NW), the heat transfer increases because of the increase in turbulence. Except for the trailing edge, this increase is less as compared to the increase in plain tip case. Similarly, with the introduction of the wake (i.e. S02-NG) the increase in the tip heat transfer coefficient is small compared to the increase in plain tip case. But for $X/C = 1.3-1.5$, there is large increase in the heat transfer coefficient with the introduction of grid and wake as seen in the Figure 6.3(b). Thus in this case, the unsteady effects dominate in the trailing edge region where most of the leakage flow occurs.

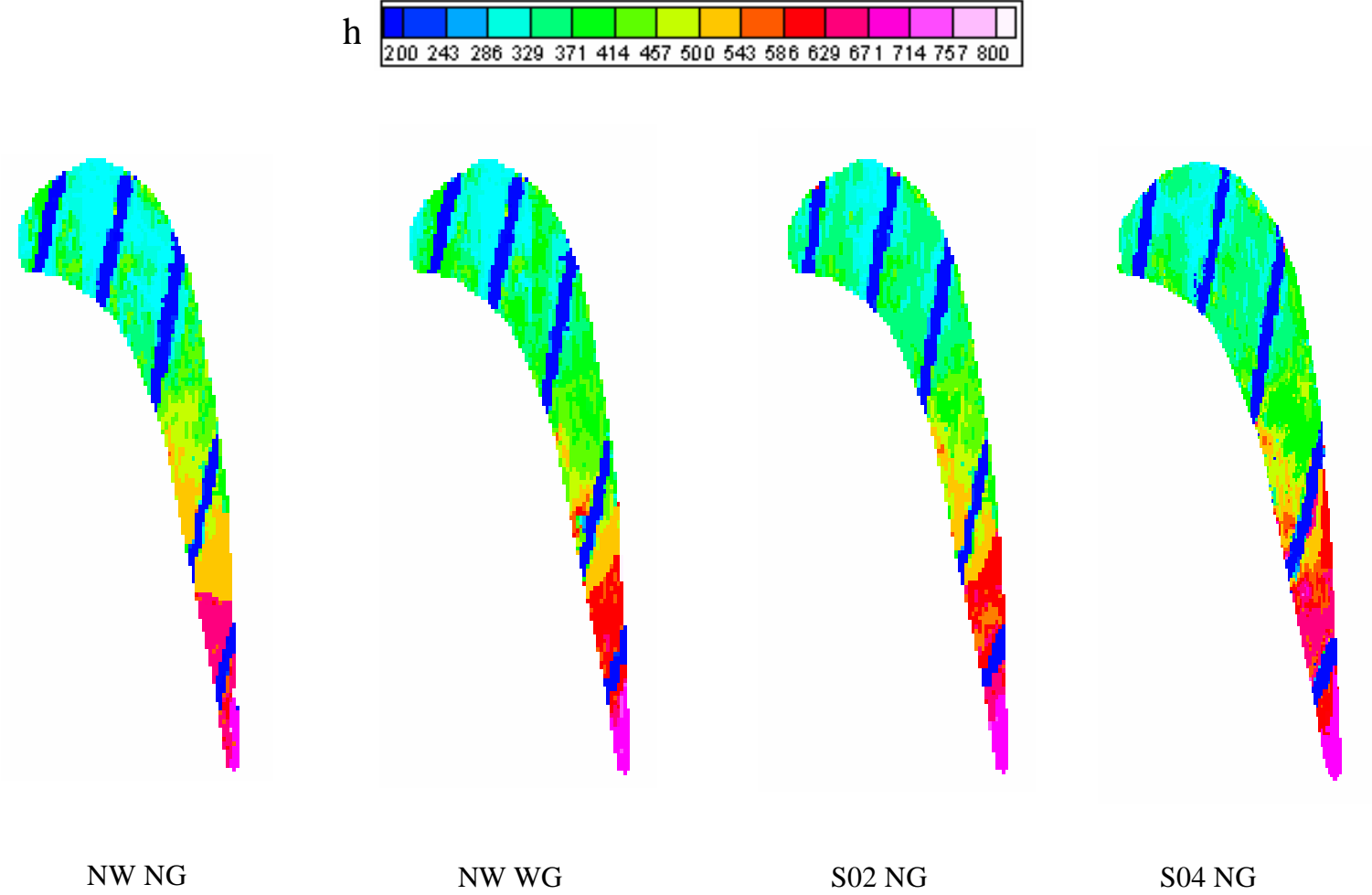


Figure 6.3(a) Detailed heat transfer coefficient distributions on tip with ribs against the flow one inch away (Case 3).

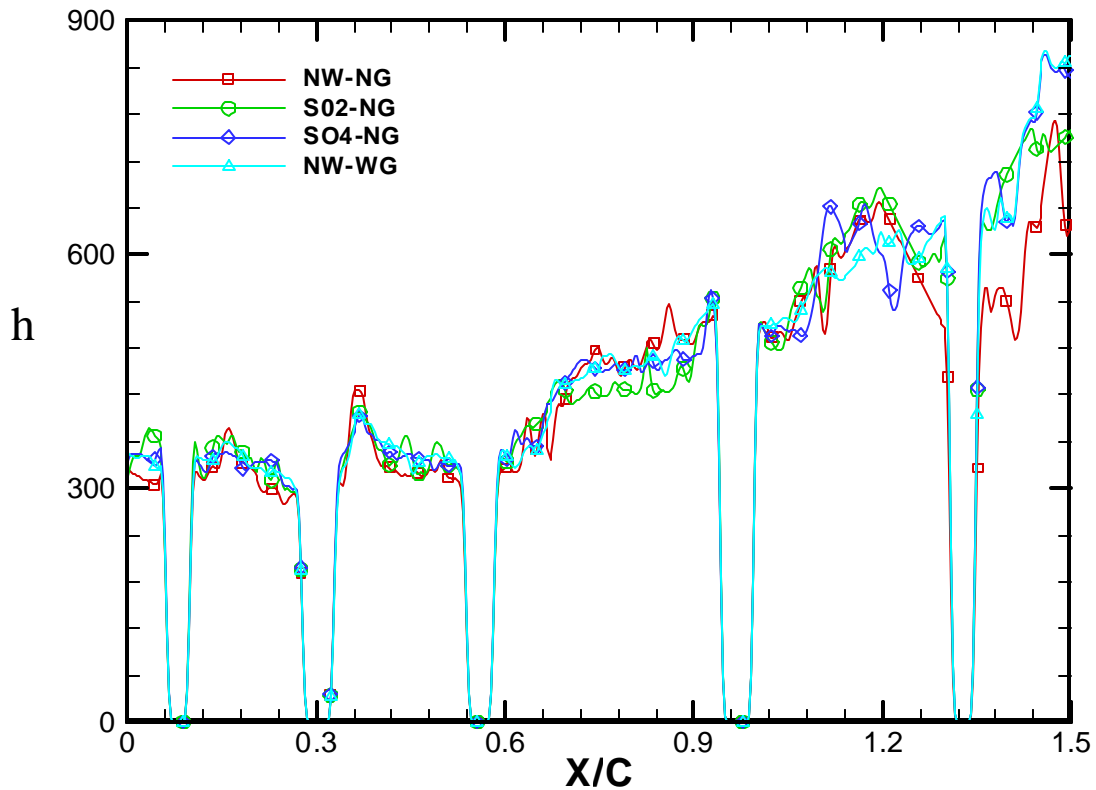


Figure 6.3(b) Effect of upstream flow condition on tip camberline heat transfer coefficient for Case 3.

Comparison of flow condition for Case 4

Figure 6.4 presents the effect of flow condition on tip heat transfer for tip geometry, Case 4. For case 4 in the middle of the leading edge region, the heat transfer coefficient in no wake and no grid (i.e. NW-NG) is almost similar with the introduction of grid (i.e. NW-WG) as seen in the Figure 6.4(a, b). With the introduction of wake, the heat transfer coefficient increases in this region. But for $X/C = 1.35-1.5$, there is large increase in the heat transfer coefficient with the introduction of grid and wake as compared to no wake and no grid. Thus in this case, the unsteady effects dominate in the trailing edge region where most of the leakage flow occurs.

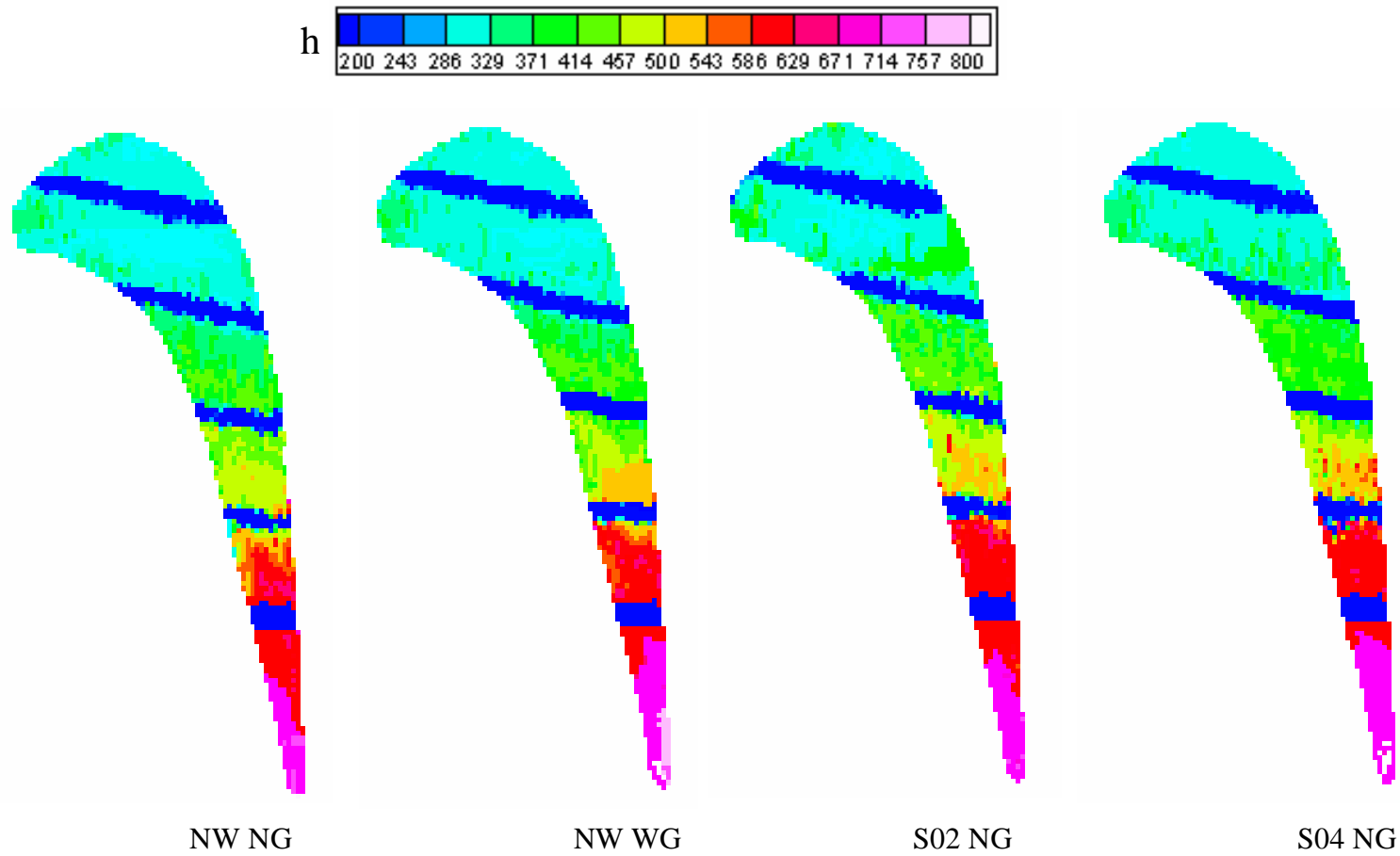


Figure 6.4(a) Detailed heat transfer coefficient distributions on tip with ribs along the flow one inch away (Case 4).

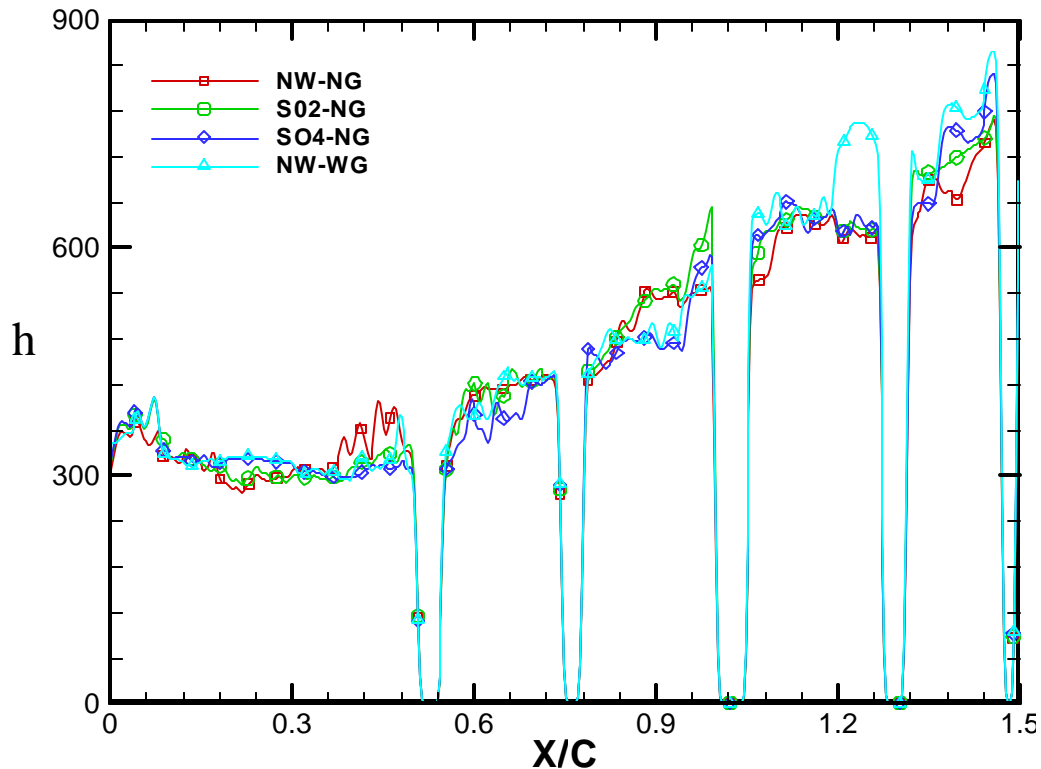


Figure 6.4(b) Effect of upstream flow condition on tip camberline heat transfer coefficient for Case 4.

Comparison of flow condition for Case 5

Figure 6.5 presents the effect of flow condition on tip heat transfer for tip geometry, Case 5. For case 5 for all the flow conditions the heat transfer coefficient is almost similar in the leading edge region as seen in the Figure 6.5(a). But for $X/C = 1.0-1.5$, there is large increase in the heat transfer coefficient with the introduction of grid and wake as seen from Figure 6.5(b). As the ribs are parallel to the leakage flow, the flow gets accelerated within the ribs. The turbulence produced due to the grid along with the accelerated flow causes higher heat transfer coefficients in the trailing edge region.

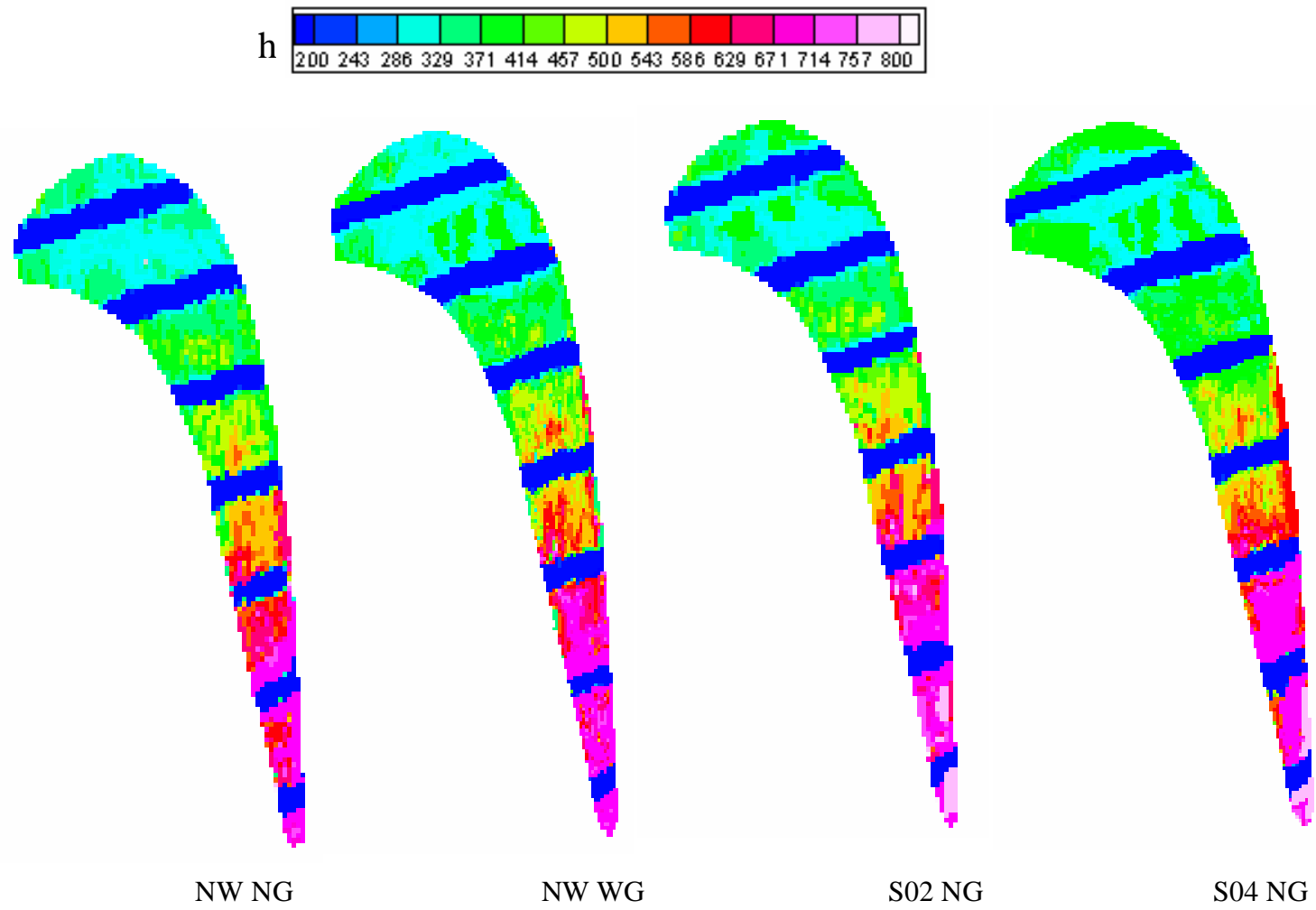


Figure 6.5(a) Detailed heat transfer coefficient distributions on tip with parallel ribs one inch away (Case 5).

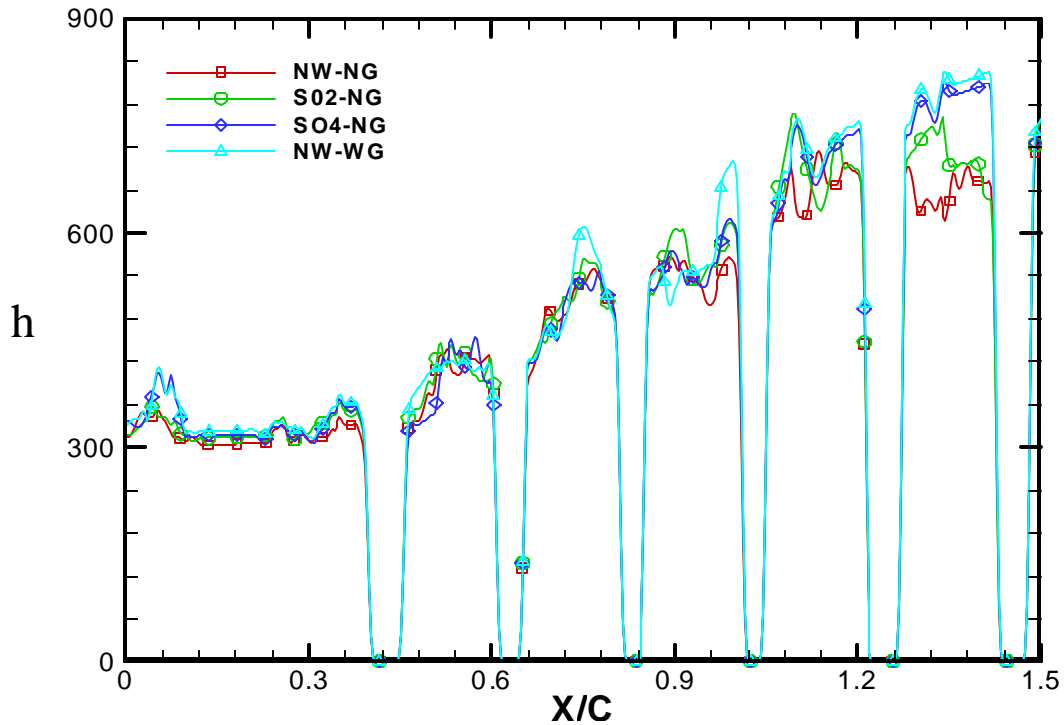


Figure 6.5(b) Effect of upstream flow condition on tip camberline heat transfer coefficient for Case 5.

Comparison of flow condition for Case 6

Figure 6.6 presents the effect of flow condition on tip heat transfer for tip geometry, Case 6. In Case 6, the cylindrical pin fins are used. For Case 6 for all the flow conditions the heat transfer coefficient is almost similar in $X/C = 0.1-1.0$ region as seen in the Figure 6.6(b). But for $X/C = 1.3-1.5$, there is large increase in the heat transfer coefficient with the introduction of grid and wake. The turbulence increase created by the grid enhances the heat transfer in the trailing edge region where most of the leakage flow occurs. There is a slight increase in the tip heat transfer when the wake is increased (i.e. Strouhal Number is changed from 0.2 to 0.4). This increase is mostly in the trailing edge region of the tip.

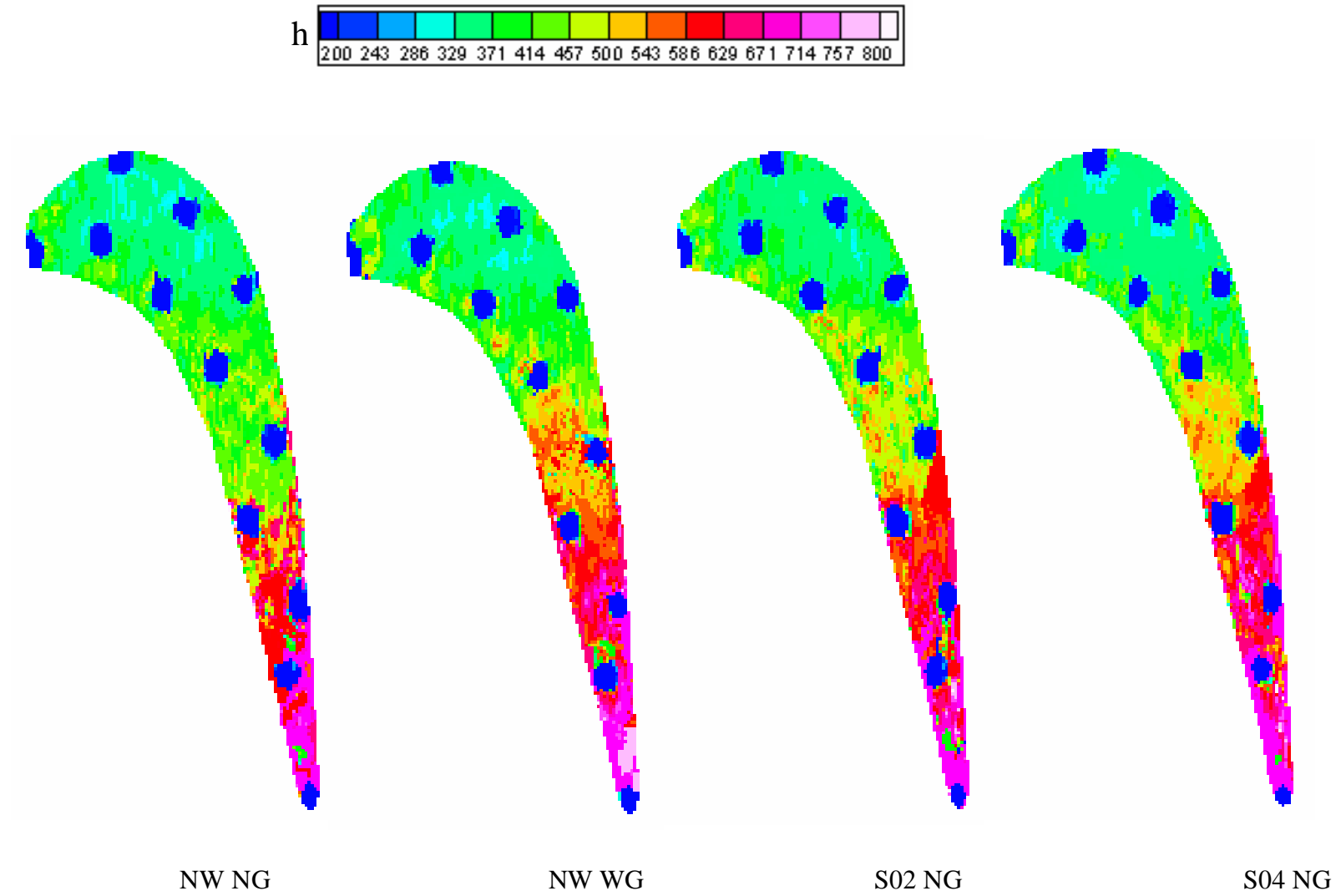


Figure 6.6(a) Detailed heat transfer coefficient distributions on tip with pins one inch away (Case 6).

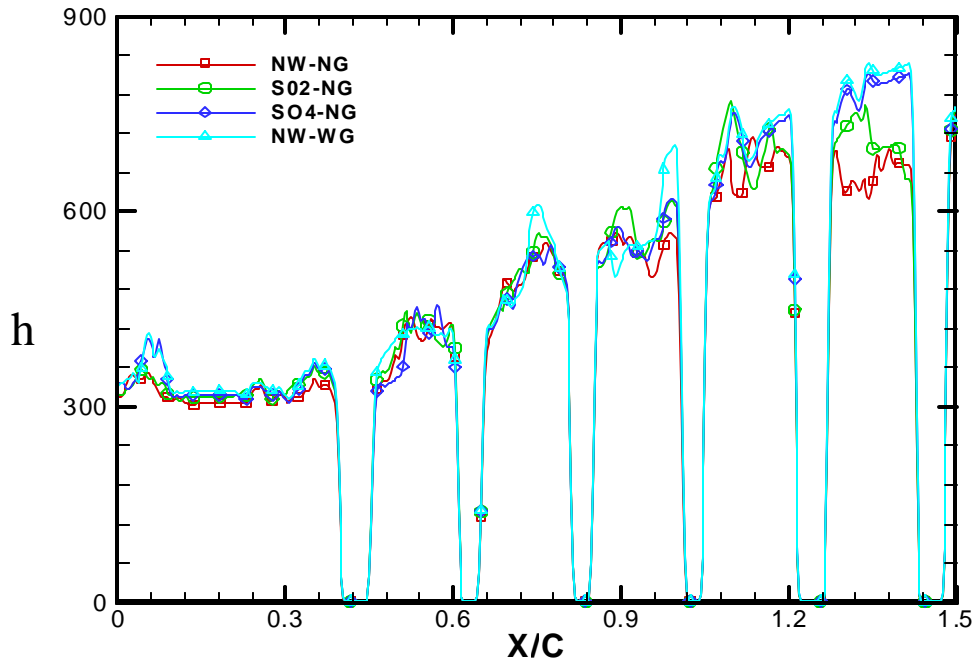


Figure 6.6(b) Effect of upstream flow condition on tip camberline heat transfer coefficient for Case 6.

Comparison of flow condition for Case 7

Figure 6.7 presents the effect of flow condition on tip heat transfer for tip geometry, Case 7. For case 7 for all the flow conditions the heat transfer coefficient is almost similar in $X/C = 0.05-0.7$ region as seen in Figure 6.7(b). But for $X/C = 0.75-1.1$, there is large increase in the heat transfer coefficient with the introduction of grid and wake. In Figure 6.7(c), we see that there is an increase in the tip heat transfer coefficient over the entire tip with the introduction of grid and wake. Thus in this case, with the introduction of unsteady effects, there is an increase in the heat transfer coefficient along the trailing edge region towards the pressure side but on the entire tip towards the suction side. With the squealer, the flow acceleration above the squealer rim reducing the effect of the upstream flow condition. This is seen clearly in Figure 6.7(b,c).

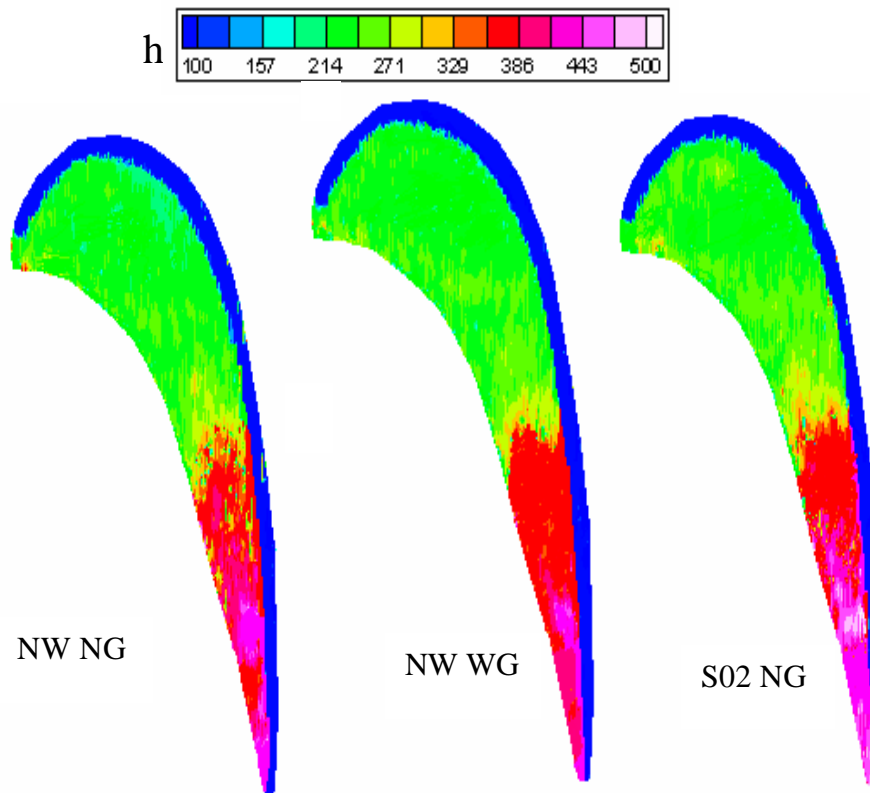


Figure 6.7(a) Detailed heat transfer coefficient distributions on tip with Suction Side Squealer (Case 7).

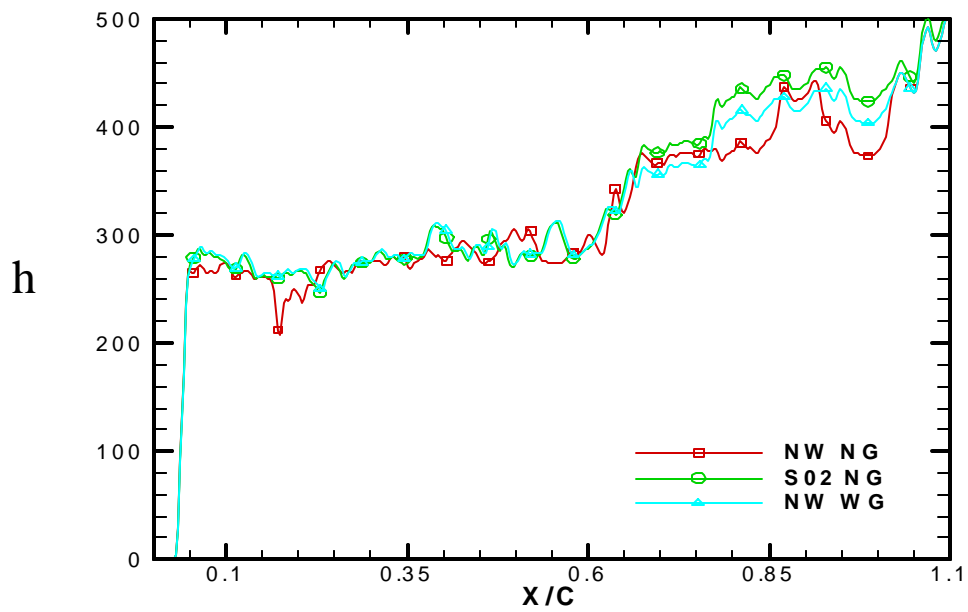


Figure 6.7(b) Effect of upstream flow condition on tip heat transfer coefficient towards pressure side for Case 7.

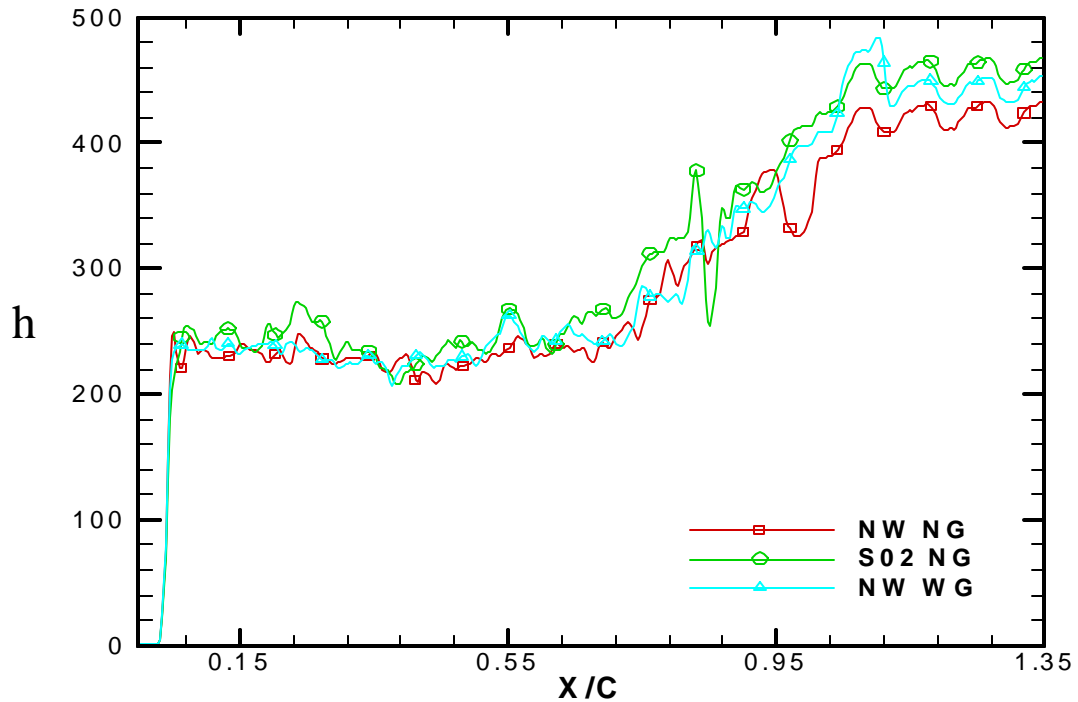


Figure 6.7(c) Effect of upstream flow condition on tip heat transfer coefficient towards suction side for case 7.

Comparison of flow condition for Case 8

Figure 6.8 presents the effect of flow condition on tip heat transfer for tip geometry, Case 8. For case 8 for all the flow conditions the heat transfer coefficient is almost similar in $X/C = 0.05-0.6$ region as seen in Figure 6.8(a, b, c). But for $X/C = 0.62-1.1$, there is large increase in the heat transfer coefficient with the introduction of grid and wake. Thus in this case, with the introduction of unsteady effects there is increase in the heat transfer coefficient along the trailing edge region. Due the presence of the squealer on the suction side, there is resistance to the flow. So, the flow tries to move towards the path of low resistance. As a result, the flow tends to move from the leading edge on suction side towards the trailing edge. This leads to the slight increase in the heat transfer along the trailing edge region.

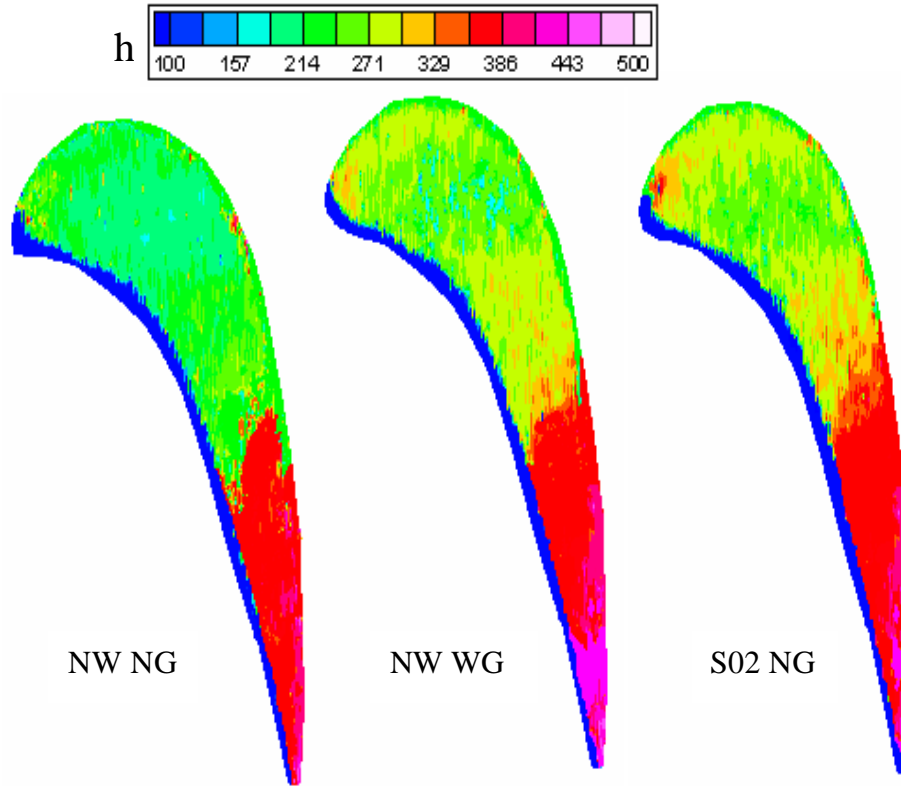


Figure 6.8(a) Detailed heat transfer coefficient distributions on tip with Pressure side Squealer (Case 8).

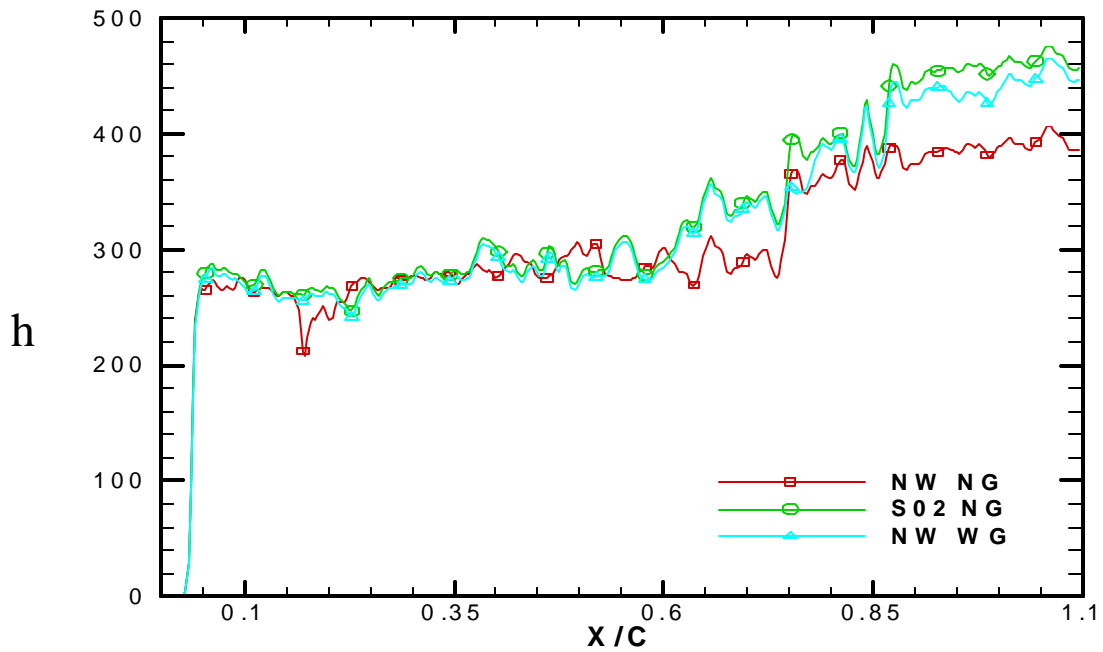


Figure 6.8(b) Effect of upstream flow condition on tip heat transfer coefficient towards pressure side for Case 8.

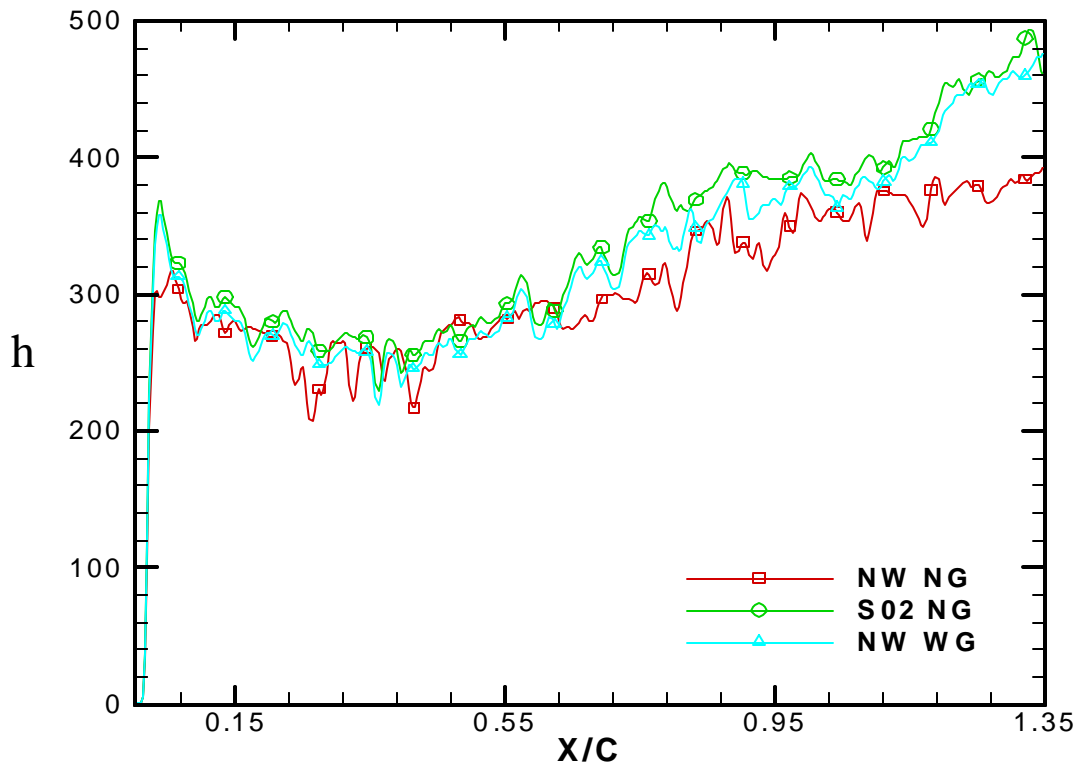


Figure 6.8(c) Effect of upstream flow condition on tip heat transfer coefficient towards suction side for Case 8.

Comparison of flow condition for Case 9

Figure 6.9 presents the effect of flow condition on tip heat transfer for tip geometry, Case 9. For case 9 with the introduction of grid and wake, there is large increase in the overall tip heat transfer coefficient over the entire tip region as seen in Figure 6.9(a, b, c). Thus in this case, the unsteady effects are dominant over the entire tip region. Because the squealer is placed on the midchord, the leakage flow entering the clearance gap through the leading edge is bifurcated along the pressure side rim and suction side rims resulting in the even heat transfer from leading edge to trailing edge on both sides of the squealer. This can be seen in the color plots in Figure 6.9(a).

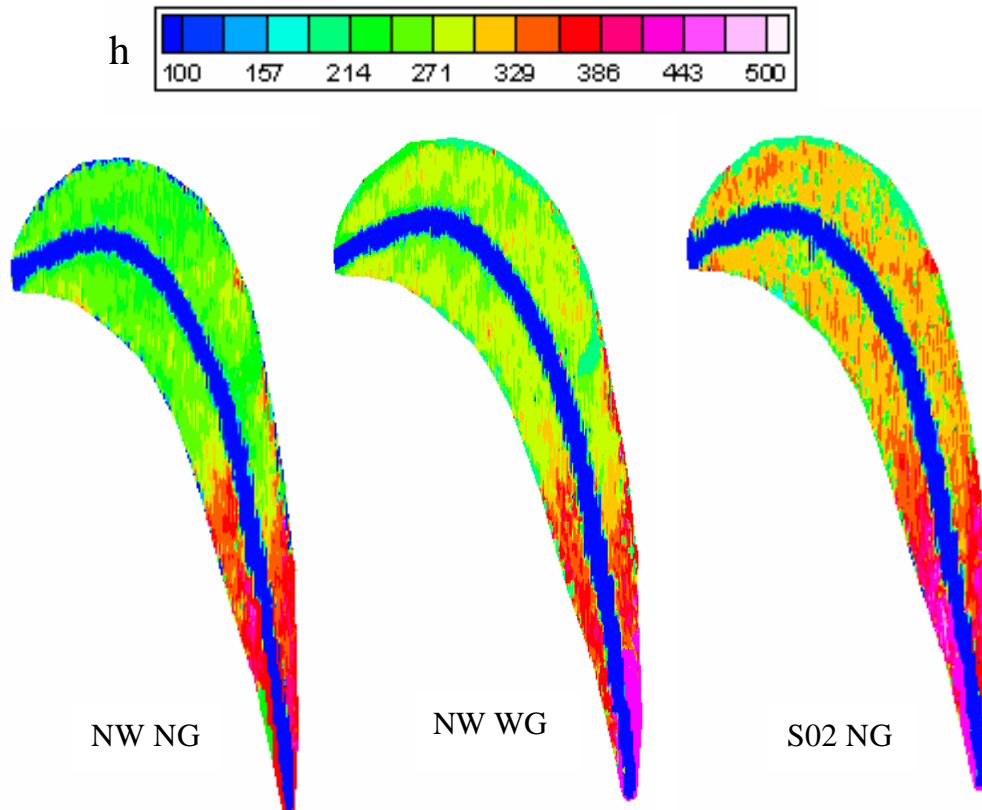


Figure 6.9(a) Detailed heat transfer coefficient distributions on tip with camberline Squealer (Case 9).

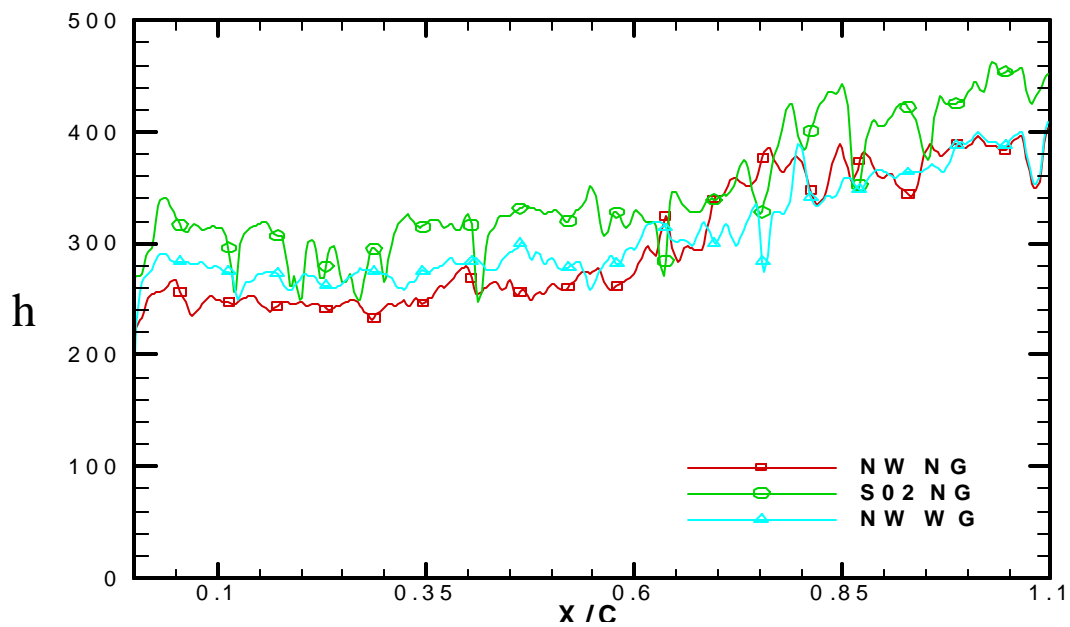


Figure 6.9(b) Effect of upstream flow condition on tip heat transfer coefficient towards pressure side for Case 9.

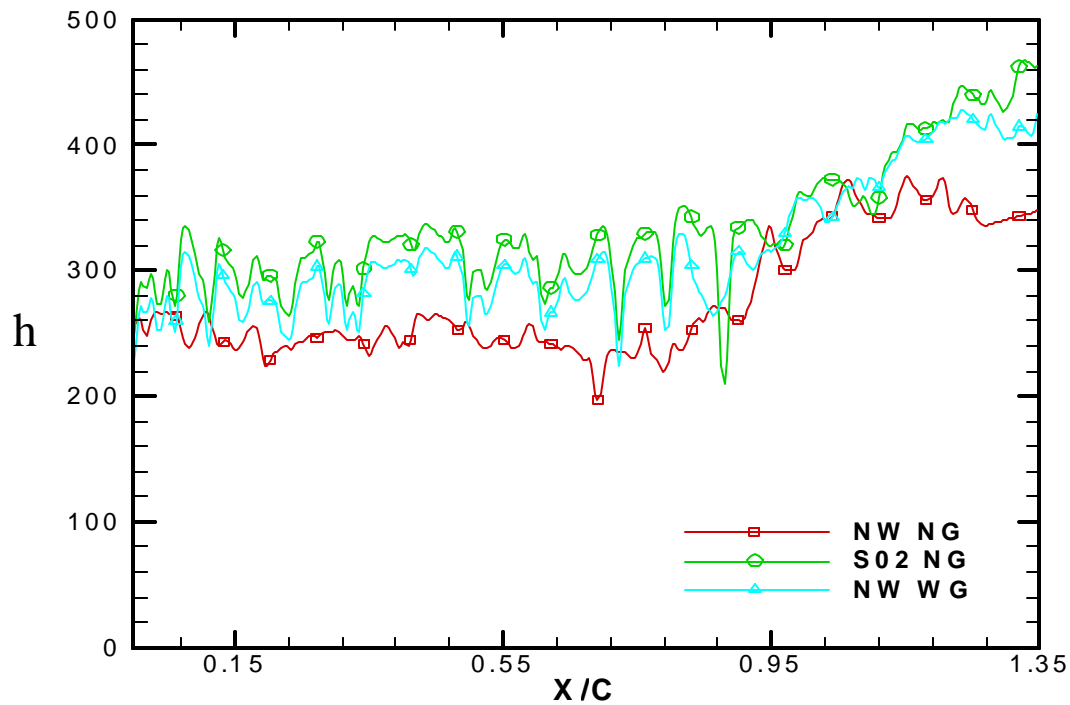


Figure 6.9(c) Effect of upstream flow condition on tip heat transfer coefficient towards suction side for Case 9.

Comparison of flow condition for Case 10

Figure 6.10 presents the effect of flow condition on tip heat transfer for tip geometry, Case 10. For case 10 with the introduction of grid and wake, there is small increase in the heat transfer coefficient over the entire tip region the Figure 6.10(a, b, c). Thus in this case, the unsteady effects are minimized and there is uniform heat transfer coefficient over the entire tip. The full squealer causes significant acceleration across the tip for the reduced leakage flow resulting in lesser effect of upstream flow conditions. With the introduction of the grid, the turbulence in the flow increases which leads to slight increase in the tip heat transfer. Also with the increase of wake (i.e. Strouhal Number changed from 0.2 to 0.4) there is slight increase in the tip heat transfer. But due to the cavity formed, all the unsteady effects are minimized.

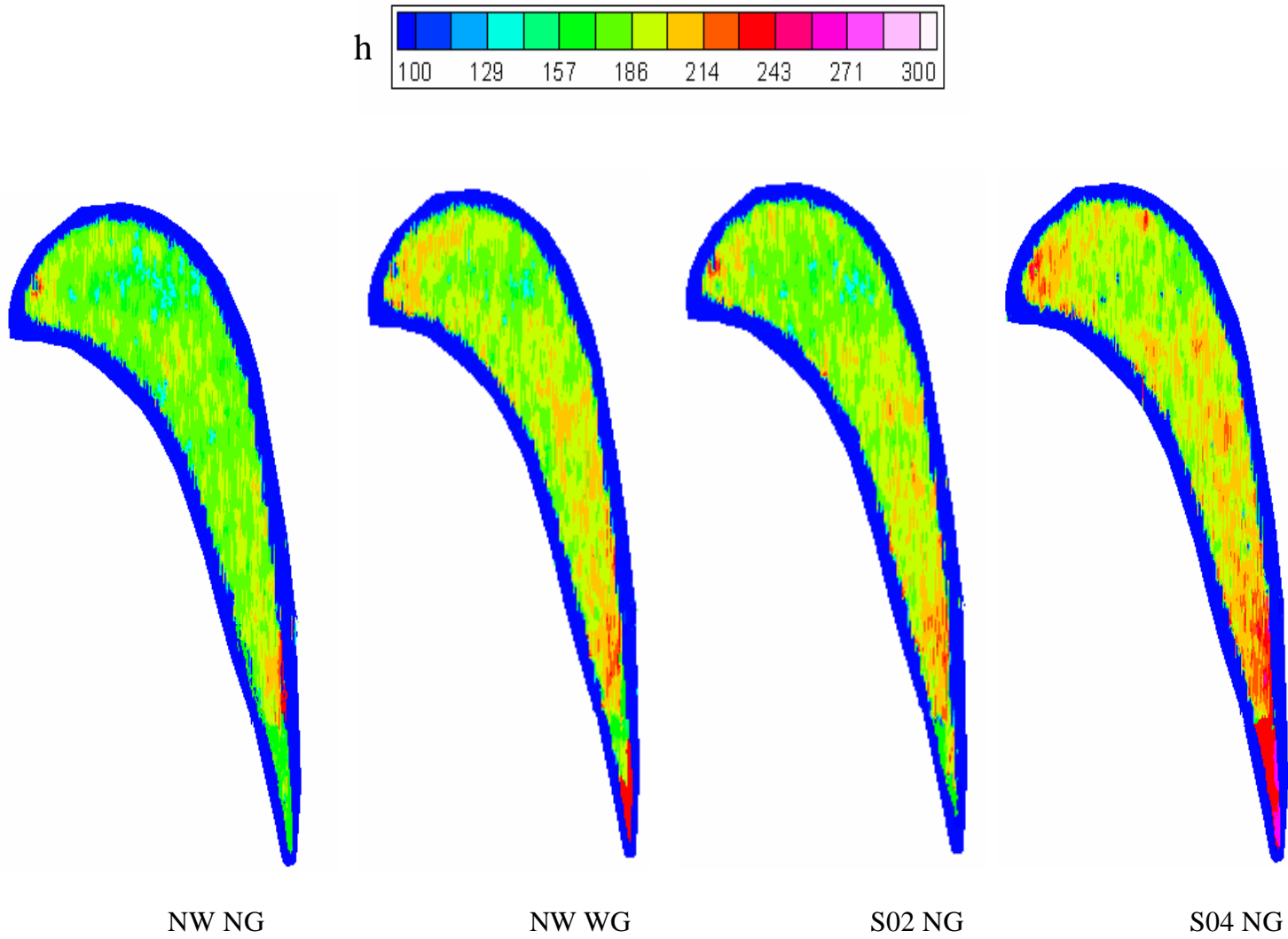


Figure 6.10(a) Detailed heat transfer coefficient distributions on tip with Full Squealer (Case 7).

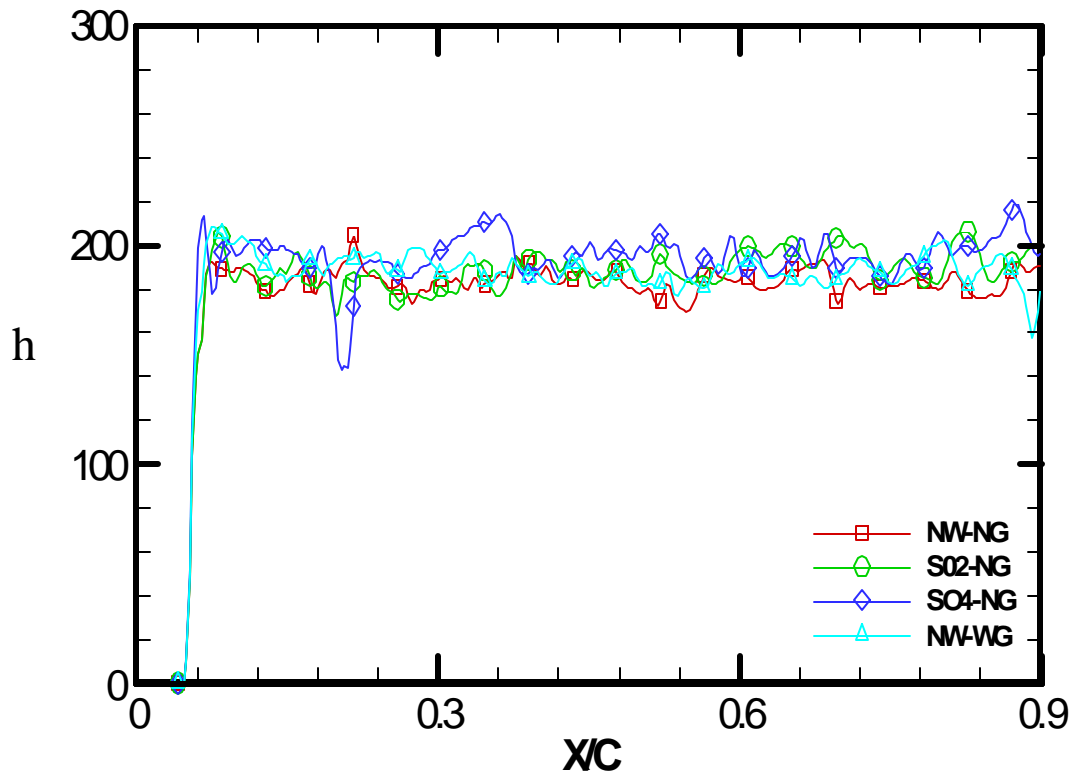


Figure 6.10(b) Effect of upstream flow condition on tip heat transfer coefficient towards pressure side for case 10.

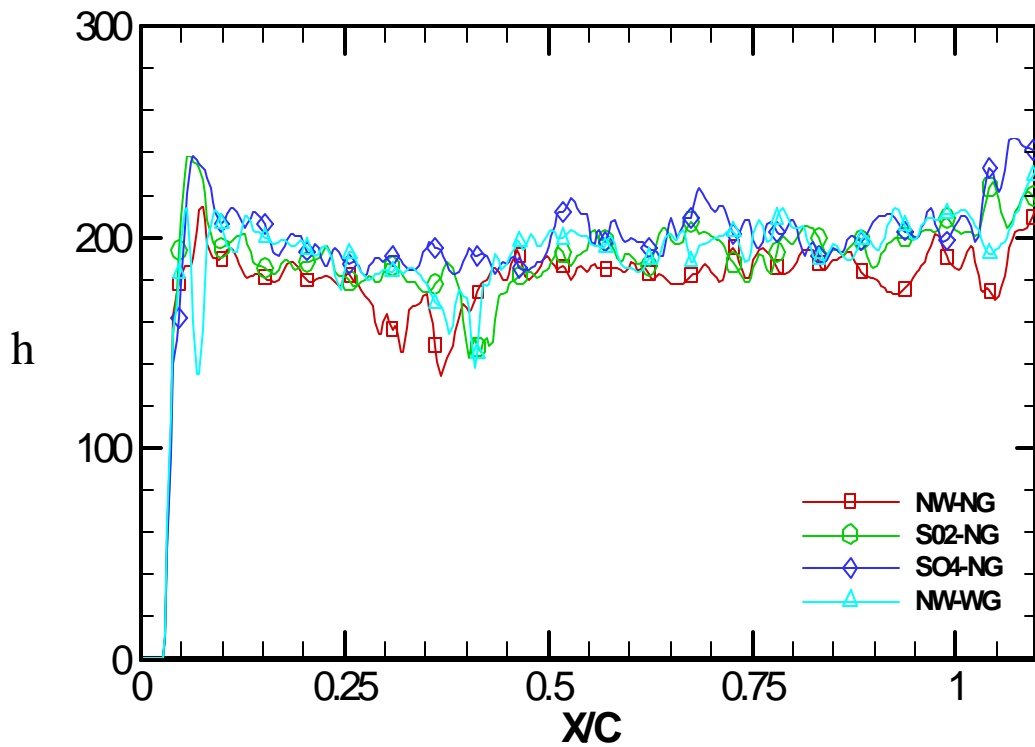


Figure 6.10(c) Effect of upstream flow condition on tip heat transfer coefficient towards suction side for case 10.

6.2 Effects of Tip Geometry on Heat Transfer

Figure 6.11 compares the heat transfer coefficient distributions on the tip for all the ten tip geometry configurations for the baseline flow condition (i.e. no wake and no grid). Comparing Case 2 with the baseline plain tip case, the trip strips placed against the flow with a spacing of 18-mm appear to reduce the trailing edge heat transfer coefficients significantly. The trip strips appear to provide some blockage to the leakage flow resulting in lower heat transfer coefficients over most of the tip surface. In the leading edge regions, the heat transfer coefficients are similar if not slightly higher than the plain tip. For Case 3, the leading edge region heat transfer coefficient appears to be reduced but the trailing edge region appears to produce similar levels as the plain tip. The leakage flow direction may be moving from the mid-chord towards the trailing edge for this case resulting in more flow in the rear end of the tip. Case 4 produces slightly higher heat transfer coefficients in the leading edge region and slightly lower values near the trailing edge. The trip strips are aligned along the mainstream flow direction. The leakage flow appears to accelerate between the regions between the trip strips enhancing heat transfer coefficients. The trailing edge region has lower values due to the reason that bulk of the leakage flow moves over the blade tip before it reaches the trailing edge. For Case 5, the heat transfer values are similar to that of Case 4. In this case, the trip strips are aligned parallel to the leakage flow. In this case also, the leakage flow accelerates between the trip strips and there appears to be no blockage effect by the trip strips to reduce the leakage flow. Case 6 produces higher levels of heat transfer coefficients over the entire tip surface as the plain tip. The pin fins do not appear to be increasing blockage or reducing leakage flow. This case increased acceleration of the leakage flow between the

pin fins and thus producing similar levels of heat transfer coefficient as the plain tip. The vortex shedding behind the pins further enhance the heat transfer. The case 7 produces lower heat transfer coefficients over the entire tip surface. For the suction side squealer, the blockage is not affecting the leakage flow till the flow reaches the suction side rim. This causes the leakage flow to enter the tip gap and move along the tip towards the trailing edge causing higher h values at the trailing edge. The case 8 produces slightly similar heat transfer coefficients on the leading edge as compared to baseline case. Because of the squealer on the pressure side, the leakage flow finds an obstruction at starting which causes detachment of this flow over the blade tip. This in turn reduces the heat transfer coefficient over the tip along the leading edge. In case 9, due to the presence of the squealer at the mean camberline the leakage flow finds an obstruction that causes bifurcation of leakage flow. This causes even levels of heat transfer coefficients on both sides of the squealer. Case 10 produces lowest heat transfer coefficients over the entire tip surface as compared to all the tip geometries proposed. This is because the groove or cavity acts as a labyrinth seal to increase the resistance to the flow and thus reduces the leakage flow and the associated heat transfer. There is some flow attachment near the leading edge but the weaker leakage flow reduces overall heat transfer.

Overall, it appears that Case 10 produce the largest reduction in heat transfer coefficients over the tip surface compared to the plain tip.

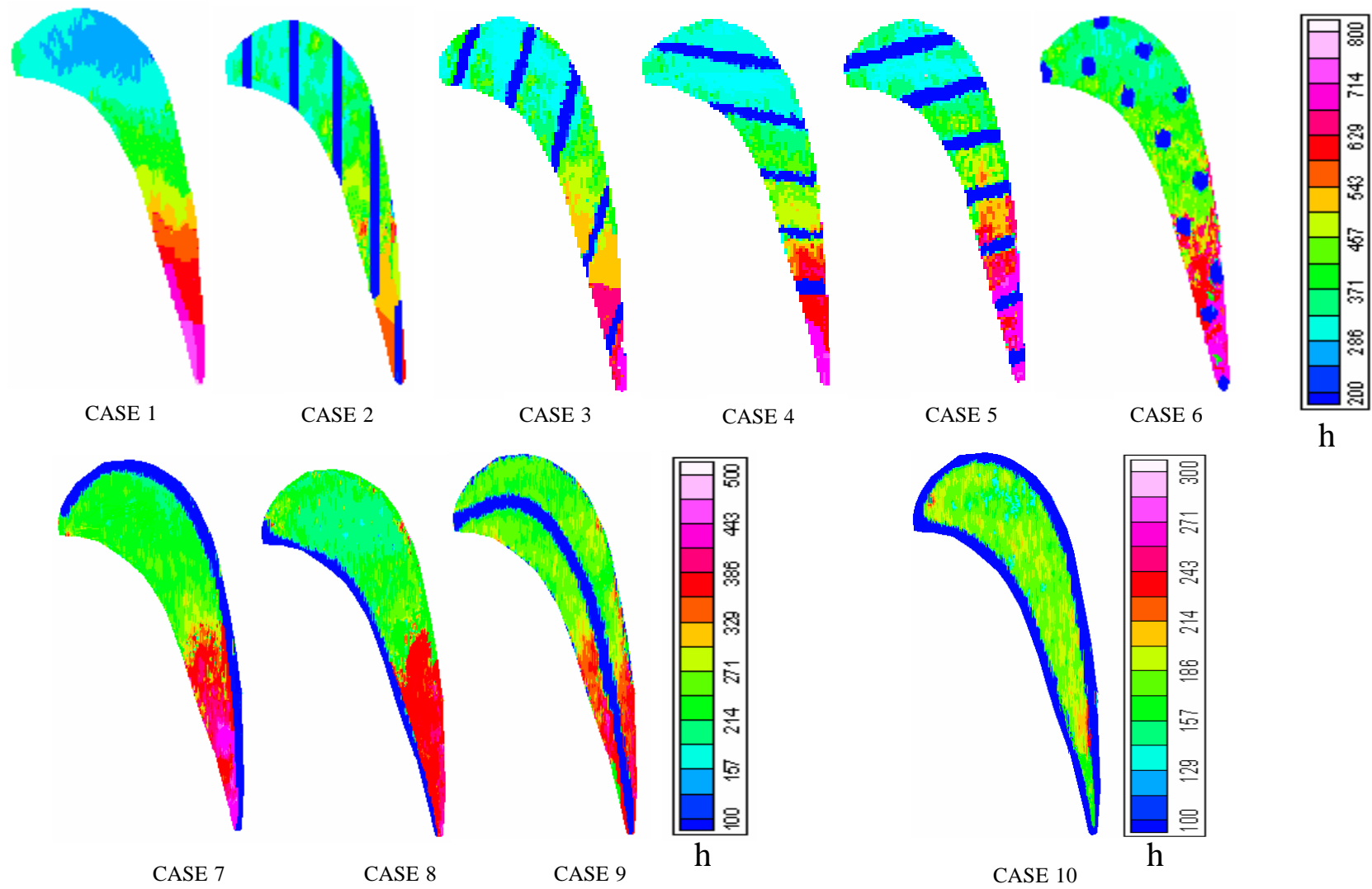


Figure 6.11. Detailed heat transfer coefficient distributions on tip for all the different tip geometries

6.3 Effects of Tip Geometry on Heat Transfer Compared to Baseline (i.e. Case 1)

Comparison of Case 2 with Baseline Case

The trip strips placed against the flow with a spacing of 18-mm appear to reduce the trailing edge heat transfer coefficients significantly as seen in Figure 6.12. As can be seen from the Figure 5.5, this configuration produces very low pressure differential across the tip gap as compared to Case 1. The trip strips appear to provide some form of blockage or detachment to the leakage flow resulting in lower heat transfer coefficients over most of the tip surface. In the leading edge regions, the heat transfer coefficients are similar if not slightly higher than the plain tip. This region is not much of concern as compared to trailing edge heat transfer where most of the leakage flow occurs. It can be noticed here that the heat transfer coefficients in Case 2 reduces around 30% towards the trailing edge region as compared to Case 1.

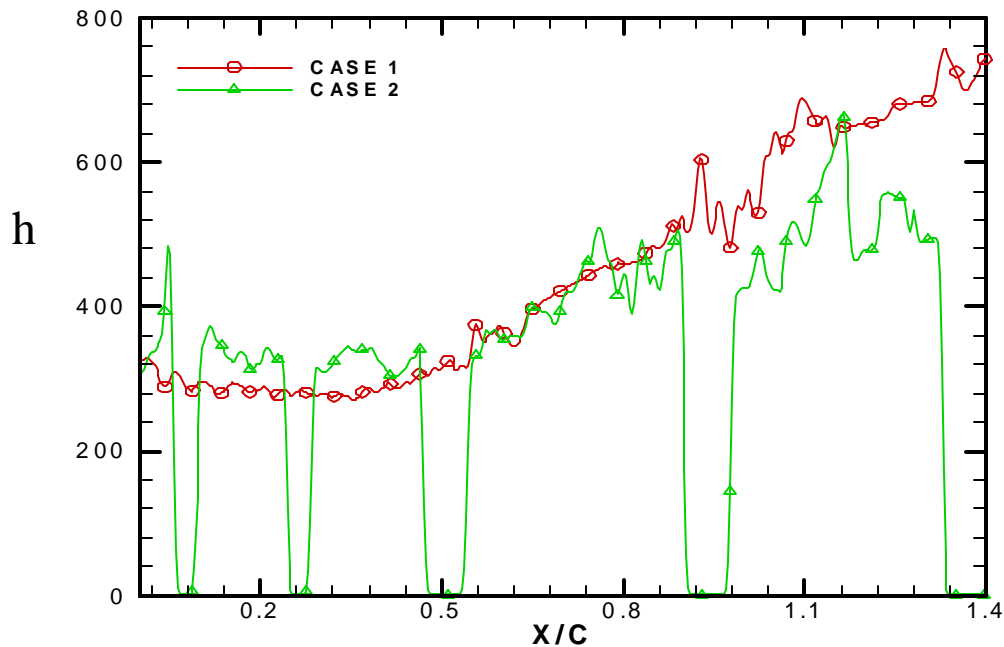


Figure 6.12. Comparison of camberline heat transfer coefficient distributions of Case 1 and Case 2.

Comparison of Case 3 with Baseline Case

The leading edge region heat transfer coefficient appears to be reduced more as compared to Case 2 as seen in the Figure 6.13. As shown in the Figure 5.5, this configuration produces slightly lower pressure differential across the tip gap as compared to Case 1. This leads to slightly lower leakage flow across the tip in this case as compared to the baseline case. The leakage flow direction may be moving from the mid-chord towards the trailing edge for this case resulting in more flow in the rear end of the tip as compared to Case 2. The heat transfer coefficient is lower in the trailing edge region for this case as compared to Case 1 but not as low as in Case 2.

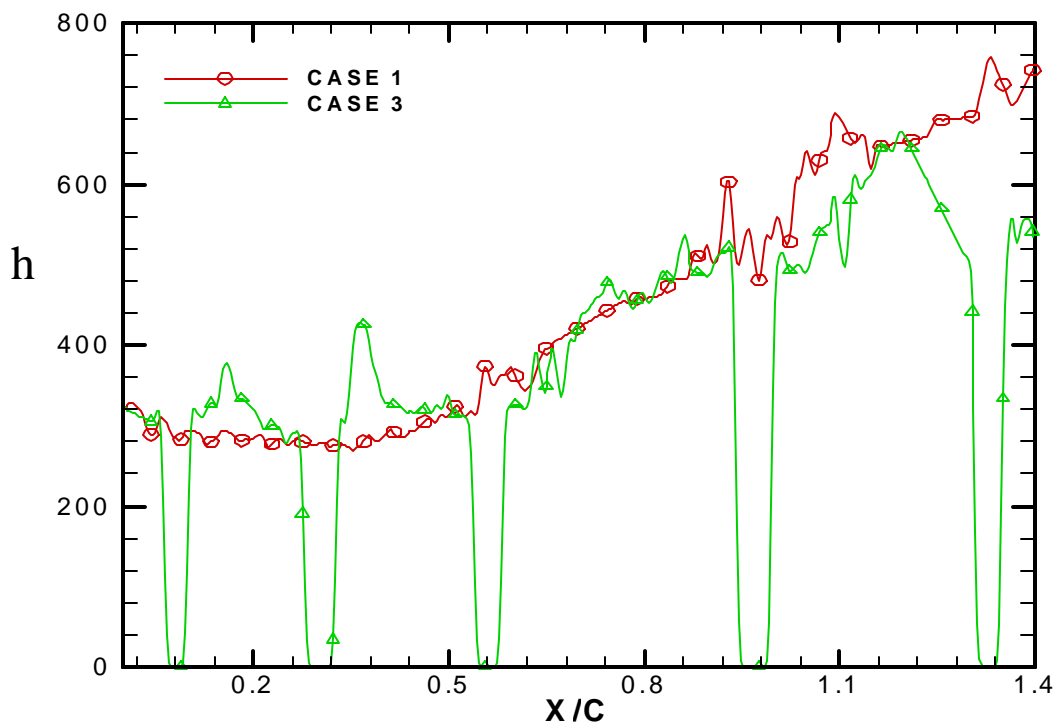


Figure 6.13 Comparison of camberline heat transfer coefficient distributions of Case 1 and Case 3.

Comparison of Case 4 with Baseline Case

The case 4 produces slightly higher heat transfer coefficients in the leading edge region and nearly similar values near the trailing edge to the Case 1 as seen in Figure 6.14. The trip strips are aligned along the flow direction. As can be seen from the Figure 5.5, in this configuration pressure difference between pressure side and suction side is higher so the leakage flow appears to accelerate between the regions between the trip strips enhancing heat transfer coefficients. There is no re-circulation or no detachment of the flow and thus the heat transfer is not reduced.

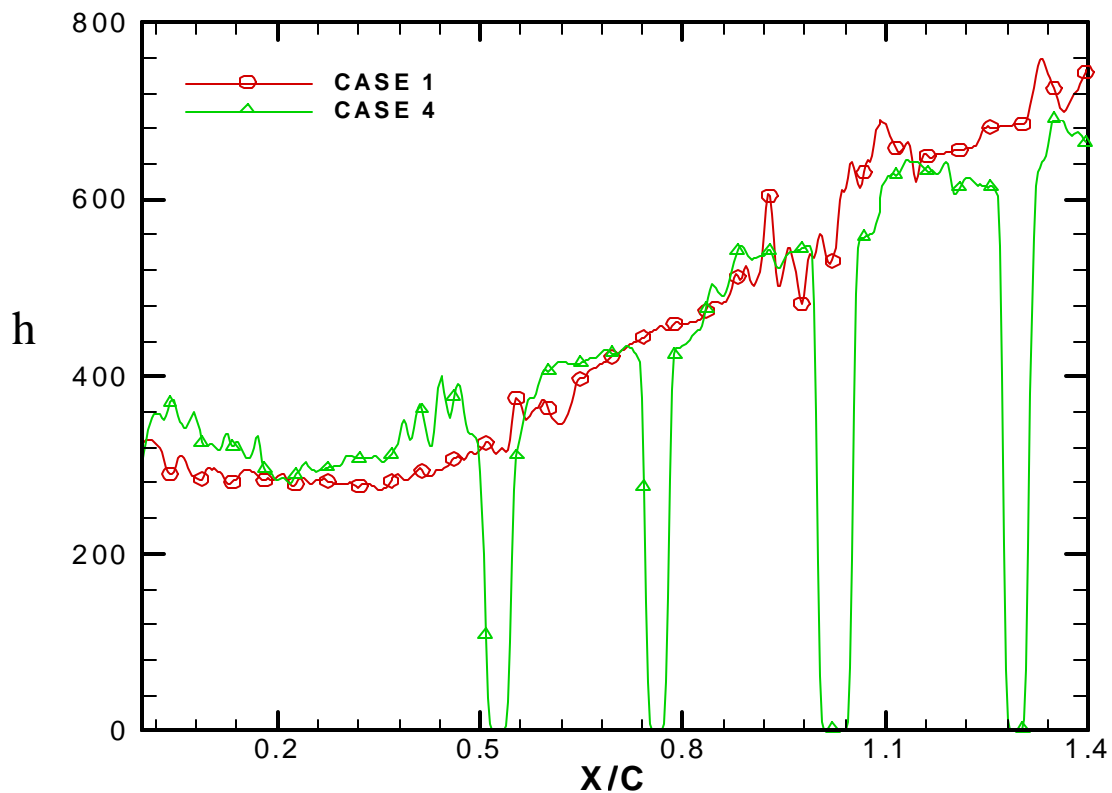


Figure 6.14 Comparison of camberline heat transfer coefficient distributions of Case 1 and Case 4.

Comparison of Case 5 with Baseline Case

In this case, the trip strips are aligned parallel to the leakage flow. This causes the leakage flow to accelerate between the trip strips and there appears to be no blockage effect by the trip strips to reduce the leakage flow. This leads to increased heat transfer on the blade tip. From Figure 6.15, it is seen that this case produces slightly higher heat transfer coefficients in the leading edge region and nearly similar values near the trailing edge to Case 1.

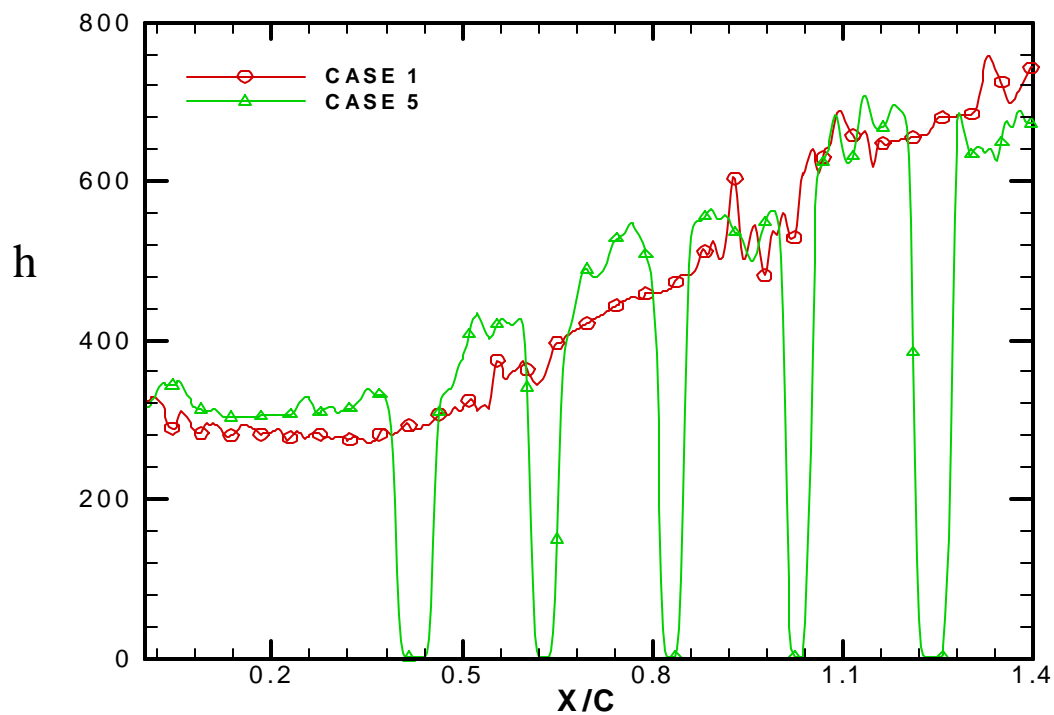


Figure 6.15 Comparison of camberline heat transfer coefficient distributions of Case 1 and Case 5.

Comparison of Case 6 with Baseline Case

Case 6 produces higher or similar levels of heat transfer coefficients over the entire tip surface as compared to the plain tip as seen in Figure 6.16. The pin fins do not appear to be increasing blockage or reducing leakage flow. The acceleration of the leakage flow increases between the pin fins and thus producing slightly higher levels of

heat transfer coefficient as compared to the plain tip. There also appears to be vortex shedding behind pins resulting in overall higher heat transfer.

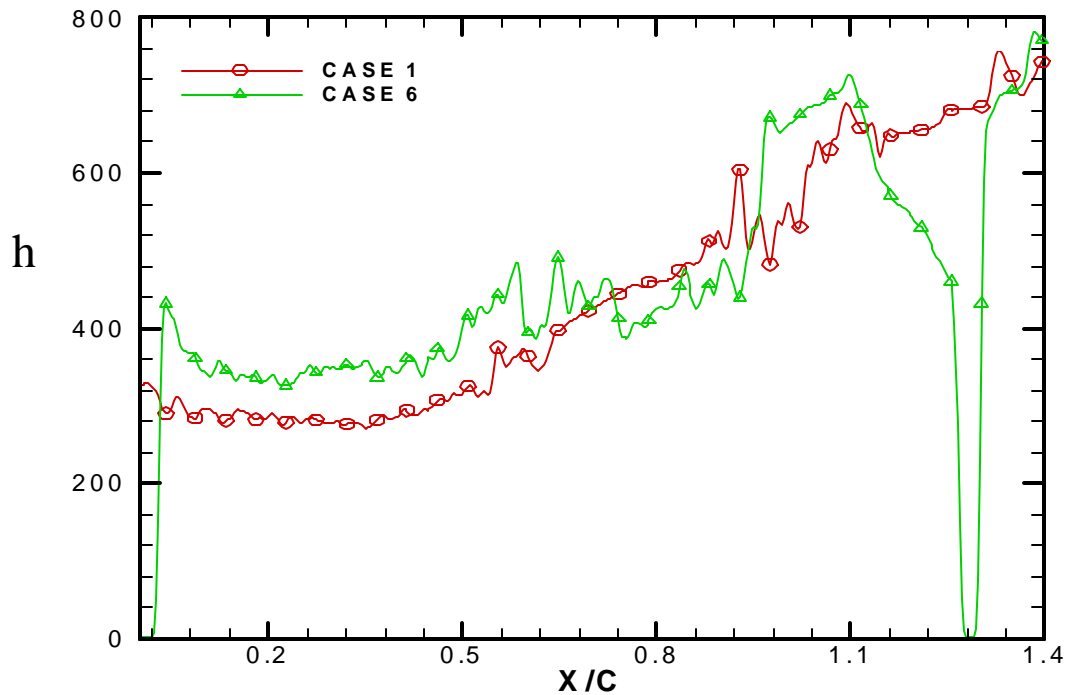


Figure 6.16 Comparison of camberline heat transfer coefficient distributions of Case 1 and Case 6.

Comparison of Case 7 with Baseline Case

Case 7 produces lower heat transfer coefficients over the entire tip surface as compared to baseline tip as seen in Figure 6.17. As shown in Figure 5.5, we see that pressure gradient across the tip is lowest, which indicates that leakage flow may be reduced. In this case, flow has similar condition to the plain tip with more clearance gap until it reaches suction side where it sees the suction side partial squealer. This squealer causes the detachment of the flow at the suction side of the tip. This reduces the tip heat transfer coefficient especially in the trailing edge region.

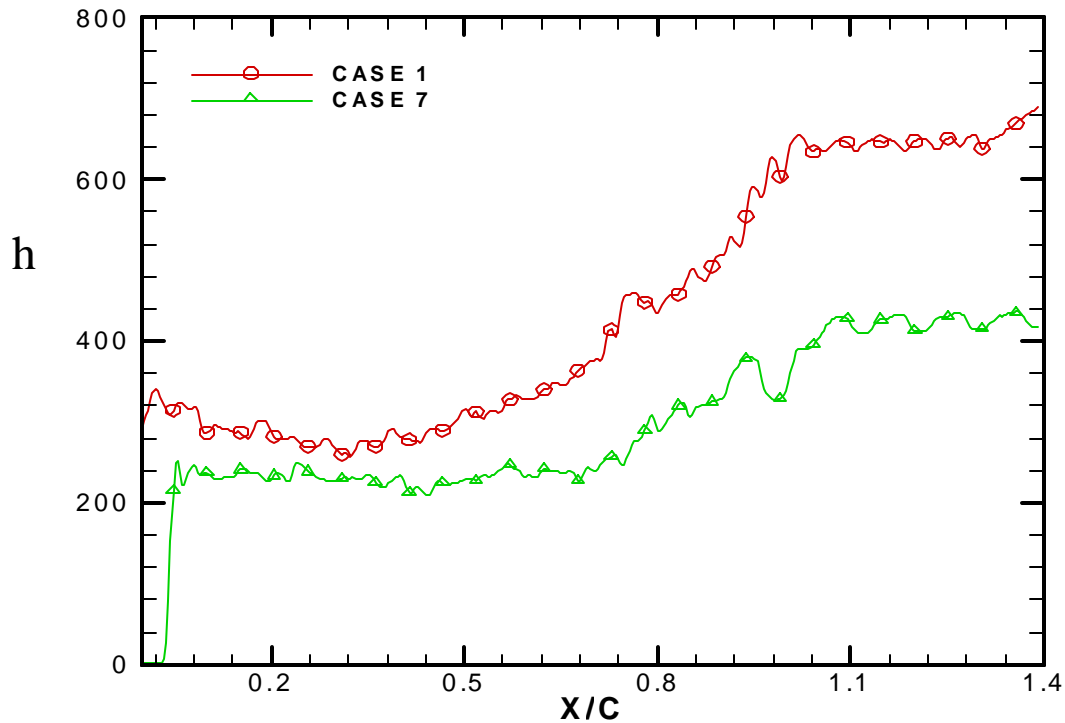


Figure 6.17 Comparison of camberline heat transfer coefficient distributions of Case 1 and Case 7.

Comparison of Case 8 with Baseline Case

Case 8 produces slightly similar heat transfer coefficients on the leading edge as compared to baseline case as seen in Figure 6.18. Because of the squealer on the pressure side, the leakage flow finds an obstruction on the pressure side rim, which causes detachment of this flow over the edge of the blade tip. But as the flow reattaches again on the tip, the flow gets accelerated. As seen from Figure 5.5, the pressure gradient increases after the pressure side squealer but this is lower compared to baseline case. Large reductions in the heat transfer coefficients on the trailing edge are seen as compared to the baseline case.

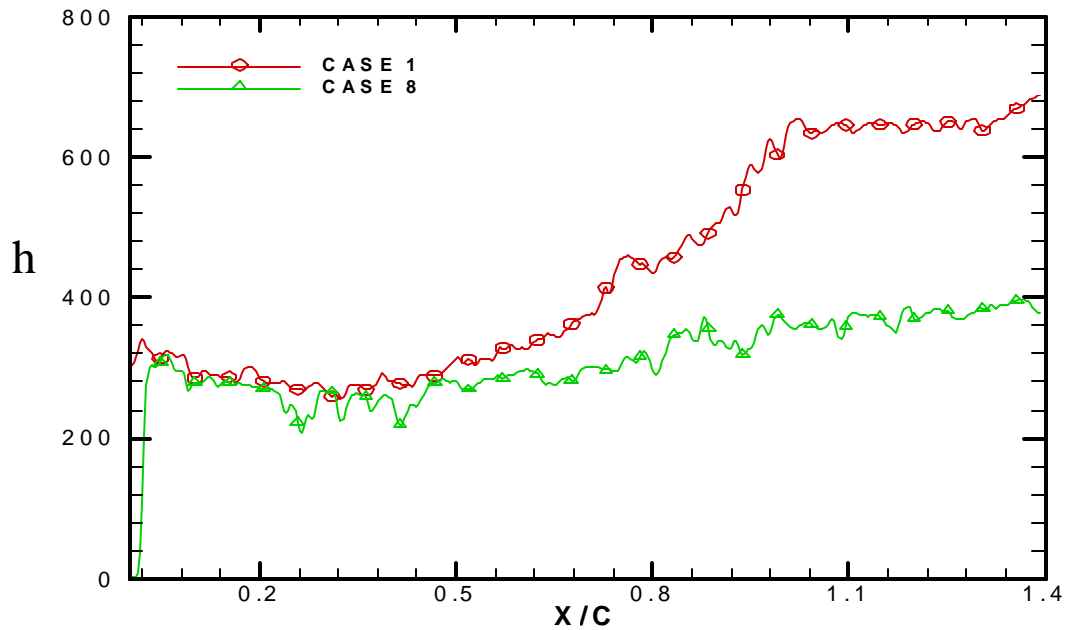


Figure 6.18 Comparison of camberline heat transfer coefficient distributions of Case 1 and Case 8.

Comparison of Case 9 with Baseline Case

Case 9 produces slightly lower heat transfer coefficients on the leading edge as compared to baseline case as seen in Figure 6.19. Due to the presence of the squealer at the mean camberline, the leakage flow finds an obstruction that causes detachment and bifurcation of this flow. But as the flow reattaches, the flow gets accelerated as seen in Figure 5.5, the pressure gradient increases after the mean camberline squealer but this is lower compared to baseline case. This causes the reduction in the heat transfer coefficients on the trailing edge as compared to the baseline case.

Comparison of Case 10 with Baseline Case

Case 10 produces lowest heat transfer coefficients over the entire tip surface as compared to all the tip geometries proposed. This is because the groove or cavity acts as a labyrinth seal to increase the resistance to the flow and thus reduces the leakage flow and the associated heat transfer. Because of the flow re-circulation in cavity, the heat

transfer coefficient reduces 30-40% as compared to the baseline case that can be seen in Figure 6.20. Overall, it appears that case 10 produces the largest reduction in heat transfer coefficients over the entire blade tip.

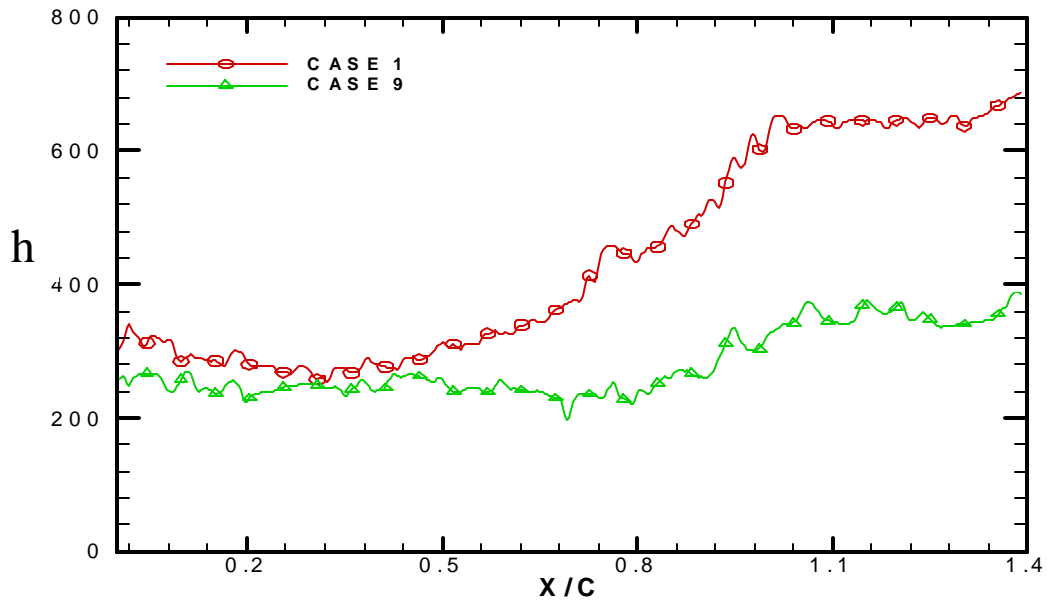


Figure 6.19 Comparison of camberline heat transfer coefficient distributions of Case 1 and Case 9.

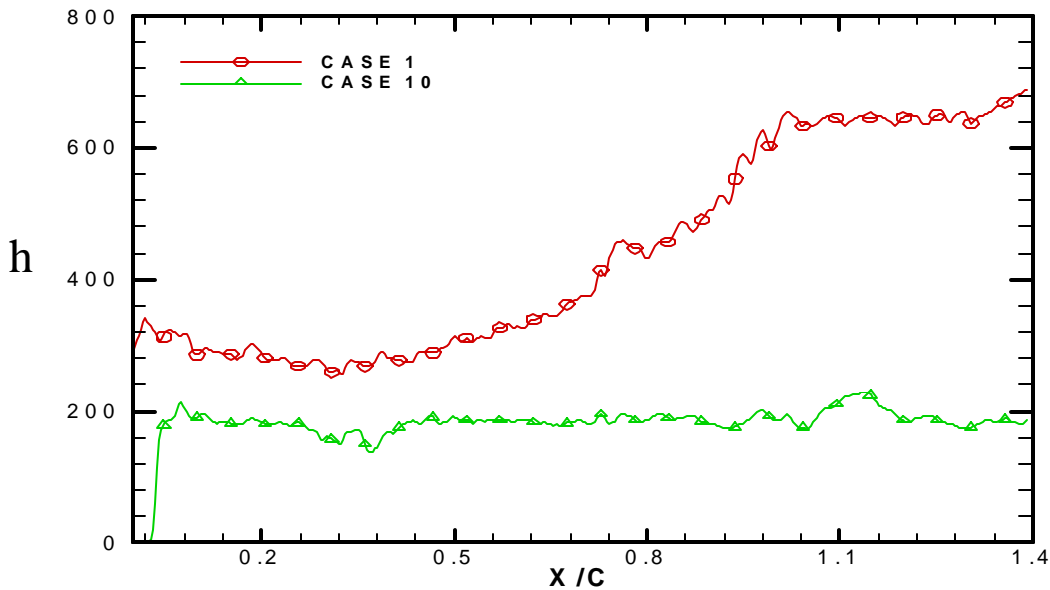


Figure 6.20 Comparison of camberline heat transfer coefficient distributions of Case 1 and Case 10.

Chapter 7

Conclusions

A systematic investigation of various tip leakage flow sealing methods on flow and heat transfer over a turbine blade tip in a low speed cascade was performed. Several configurations of trip strips, squealers and pin fins placed on the tip to reduce leakage flow and associated heat transfer were tested. Results show that the full squealer configuration produces reduced leakage flow and the lowest heat transfer coefficient over the entire tip. The other partial squealers also helped in reducing leakage flow and associated heat transfer. The trip strips placed in a direction orthogonal to the leakage flow direction produces the lowest leakage flow and heat transfer coefficient over the tip among all the trip strip configuration tested. The other configurations produce similar levels of heat transfer coefficient compared to the plain tip or are higher than the plain tip. The effect of upstream flow condition with the presence of a grid to generate free-stream turbulence of 4.8% and to simulate passing wake due to upstream NGV trailing edge were also investigated. The presence of the wake and free-stream turbulence produced higher heat transfer coefficients on the plain tip. However, the other tip geometries showed little effect of upstream flow condition. Overall, the squealer configurations offer reduction in leakage flow and associated heat transfer. However the usage of trip strips and pin fins as tip sealing mechanisms do not provide desirable results in significant reduction of tip surface heat transfer coefficients. The effect of trip strip alignment appears to have strong effect on leakage flow and associated heat transfer.

Recommendation for future work

There are several issues that remain to be investigated. Based on the results of the present study, I recommend

1. A detailed study of squealer depth effect on leakage flow and tip heat transfer.

2. A detailed study on the influence of film cooling in the tip gap and the pressure side on the leakage flow and heat transfer.
3. A detailed study on the near tip region of the blade surface that will be affected by the leakage flow cross-over over the tip.
4. The test tip can also be used to study hub surface heat transfer by using heater plates and liquid crystals with steady the steady state technique.

References

Ameri, A.A., and Bunker, R.S., 1999, "Heat Transfer and Flow on the First Stage Blade Tip of a Power Generation Gas Turbine: Part 2 - Simulation Results," ASME Journal of Turbomachinery, Vol. 122, pp. 272-277.

Azad, Gm. S., Han, J.C., and Teng, S., 2000, "Heat Transfer and Pressure Distributions on a Gas Turbine Blade Tip," Proceedings of: International Gas Turbine and Aeroengine Congress and Exposition, ASME paper 2000-GT-194.

Azad, G.S., Han, J.C., and Boyle, R.J., 2000, "Heat Transfer and Flow on the Squealer Tip of a Gas Turbine Blade," Proceedings of: International Gas Turbine and Aeroengine Congress and Exposition, Munich, Germany, 2000-GT-195.

Azad, G.S., Han, J.C., Bunker, R.S., and Lee, C.P., 2001, "Effect of Squealer Geometry Arrangement on Gas Turbine Blade Tip Heat Transfer," Proceeding of: International Mechanical Engineering Congress and Exposition, New York, New York, November 2001, IMECE2001/HTD-2431.

Bindon, J.P., 1989, "The Measurement and Formation of Tip Clearance Loss" ASME Journal of Turbomachinery, Vol. 111, pp. 257-263.

Bunker, R.S., and Bailey, J.C., 2000, "An Experimental Study of Heat Transfer and Flow on a Gas Turbine Blade Tip With Various Tip Leakage Sealing Methods," Proceedings of the 4th HMT/ASME Heat and Mass Transfer Conference, Paper No. HMT2000-055, pp. 411-416.

Bunker, R.S. and Bailey, J.C., 2000, "Blade Tip heat Transfer and Flow with Chordwise Sealing Strips," International Symposium on Transport Phenomena and Dynamics of Rotating Machinery (ISROMAC), Honolulu, Hawaii, pp.548-555.

Bunker, R.S., Bailey, J.C., and Ameri, A.A., 1999, "Heat Transfer and Flow on the First Stage Blade Tip of a Power Generation Gas Turbine: Part 1 -Experimental Results," ASME Journal of Turbomachinery, Vol. 122, pp. 263-271.

Bunker, R.S., and Bailey, J.C., 2001, "Effect of Squealer Cavity Depth and Oxidation on Turbine Blade Tip Heat Transfer," International Gas Turbine and Aeroengine Congress and Exposition, New Orleans, June 2001, ASME Paper GT-2001.

Camci, C., Kim, K., and Hippensteel, S. A., 1991, "A New Hue Capturing Technique for Quantitative Interpretation of Liquid Crystal Images Used in Convective Heat Transfer Studies," ASME Paper 91-GT-277.

Chyu, M. K., Moon, H. K., and Metzger, D. E., 1989, "Heat Transfer in the Tip region of Grooved Turbine Blades," ASME Journal of Turbomachinery, Vol. 111, pp. 131-138.

Doorly, D. J., Oldfield, M.L.G., and Scrinvenner, C.T.J., 1985, "Wake-Passing in a Turbine Rotor Cascade," AGARD CP-390 Paper No.7, Bergen, Norway.

Dring, R. P., Joslyn, H.D., Hardin, L.W., and Wagner, J.H., 1982, "Turbine Rotor-Stator Interaction," ASME Journal of Engineering for Power, Vol. 104, pp. 729-743.

Dunn, M.G., Haldeman, C.W., 2000, "Time-Averaged Heat Flux for a Recessed Tip, Lip and Platform of a Transonic Turbine Blade," ASME Paper 2000-GT-0197

Funazaki, K., 1994, "Studies on Wake-Affected Heat Transfer around the Circular Leading Edge of Blunt Body," Proceedings of the International Gas Turbine and Aeroengine Congress and Exposition.

Han, J. C., Zhang, L., and Ou, S., 1993, "Influence of Unsteady Wake on Heat Transfer Coefficient from a Gas Turbine Blade," ASME Journal of Heat Transfer, Vol. 115, pp. 904-911.

Hodson, H. P., 1984, "Boundary Layer and Loss Measurements on the Rotor of an Axial-Flow Turbine," ASME Journal of Engineering for Gas Turbines and Power, Vol. 106, pp. 391-400.

Kaiser, I., and Bindon, J. P., 1997, "The Effect of Tip Clearance on the Development of Loss Behind a Rotor and a Subsequent Nozzle," ASME Paper 97-GT-53.

Kline, S.J. and McClintock, F.A., 1953, "Describing Uncertainties in Single Sample Experiments," Mechanical Engineering, Vol. 75, pp. 3-8.

Urban, M.F., and Vortmeyer, N., 1995, "Experimental Investigation on the Thermal Load and Leakage Flow of a Turbine Blade Tip Section with Different Tip Section Geometries," Proceedings of: ASME TURBO EXPO Land, Sea and Air, Munich, Germany, May 2000, 2000-GT-0196.

Mayle, R.E., Metzger, D.E., 1982, "Heat Transfer at the Tip of an Unshrouded Turbine Blade" Proceedings of the 7th International Heat Transfer Conference, Vol. 3, pp. 87-92.

Metzger, D.E., Bunker, R.S., Chyu, M.K., 1989, "Cavity Heat Transfer on a Transverse Grooved Wall in a Narrow Flow Channel," ASME Journal of Heat Transfer, Vol. 111, pp. 73-79.

Metzger, D.E., Dunn, M.G., Hah, C., 1990, "Turbine Tip and Shroud Heat Transfer," Proceeding of: International Gas Turbine and Aeroengine Congress and Exposition, Brussels, Belgium, September 1990, 90-GT-333.

Morphis, G., and Bindon, J. P., 1988, "The Effect of Relative Motion, Blade Edge Radius and Gap Size on the Blade Tip pressure Distribution in an Annular Turbine Cascade with Clearance," AMSE Paper 88-GT-256.

Teng, S., Han, J. C., and Azad, Gm. S., 2001, "Detailed Heat Transfer Coefficient Distributions on a Large Scale Gas Turbine Blade Tip," ASME Journal of Heat Transfer, Vol. 123, pp.

Yang, T.T., and Diller, T.E., 1995, "Heat Transfer and Flow for a Grooved Turbine Blade Tip in a Transonic Cascade," Proceedings of: International Mechanical Engineering Congress and Exposition, San Francisco, ASME No. 95-WA/HT-29.

Yamamoto, A., 1989, "Endwall Flow/Loss Mechanisms in a Linear Turbine Cascade With Blade Tip Clearance," ASME Journal of Turbomachinery, Vol. 111, pp. 264-275.

Yaras, M., Yingkang, Z., Sjolander, S.A., 1989, "Flow Field in the Tip Gap of a Planar Cascade of Turbine Blades," ASME Journal of Turbomachinery, Vol. 111, pp. 276-283.

Wittig, S., Schulz, A., Dullenkopf, K., and Fairbank, J., 1988, "Effects of Free-Stream Turbulence and Wake Characteristics on the Heat Transfer Along a Cooled gas Turbine Blade," ASME Paper No. 88-GT-179.

Vita

Vikrant Saxena was born on June 30th, 1978, in Etawah, Uttar Pradesh, India. He received the degree of Bachelor of Technology in Mechanical Engineering from Indian Institute of Technology, India. He joined the Louisiana State University Mechanical Engineering graduate program in Fall 2001. He is a candidate for the degree of Master of Science in Mechanical Engineering in Spring 2003. He is joining Doctoral program in Mechanical Engineering at Pennsylvania State University beginning Spring 2003.